Eötvös Loránd University
Doctoral School of Environmental Sciences
Environmental Physics Program

Large-scale atmospheric circulation driven changes in the Arctic cryosphere and Central-European hydroclimate – with insights from paleoclimate

Dániel Topál

Dissertation submitted in partial fulfilment of the degree of Doctor of Philosophy.

Advisors: Dr. István Gábor Hatvani & Dr. Zoltán Kern (ELKH CSFK FGI)

External consultant: Prof. Qinghua Ding (UC Santa Barbara)

ELTE
EÖTVÖS LORÁND
TUDOMÁNYEGYETEM

DOI: 10.15476/ELTE.2022.275

2022

PREFACE

The motivation behind this work roots back to my high school years, when my parents and high-school geography teacher, *Attila Kiss*, planted the idea in my mind to pursue a research scientist career; indirectly, by their way of thinking about nature, which I am sincerely grateful for. The first research article I read was about how changes in the Arctic were happening at a pace exceeding the global average; termed Arctic amplification (AA). At that time, I did not understand much of the atmosphere, however it was enough to gravitate my attention towards climate dynamics. I later on learnt that tropical dynamics is the key to drive global atmospheric circulation. Therefore, always pursuing the global picture became an essential viewpoint of mine in approaching scientific problems.

I was lucky to be the member of the Hungarian student research association since high school, which provided a community that motivated me to try to be a member or the Arctic climate research community. Since from Hungary only few people worked on studies related to the Arctic, it appeared to me as a great challenge to meet professors that actually work in the frontline of Arctic climate science. That have led me first to Alaska, USA where I participated at a summer school on Arctic sea-ice changes at the International Arctic Research Center. I am grateful to Prof. *Vladimir Alexeev* who – despite I was a BSc student in the summer school for PhD students – was opened to my restless yet immature questions on the Arctic. In short, that is when I decided to focus my attention on the Arctic for good, before even starting my MSc studies. At half time of my MSc studies, I spent a summer at UC Santa Barbara in California, USA where I started working with Prof. *Qinghua Ding* who has ever since guided my path in becoming a scientist and to whom I owe the dynamical perspective on the climate system, which I developed over the past years. On top of these international connections, I had also been working closely with members of a HAS Momentum Research group at the Institute for Geological and

Geochemical Research in Hungary ever since 2015 (1st BSc) under the supervision of *Istvan Gabor Hatvani* and *Zoltan Kern*. To them I owe my first research paper (Topál et al. 2016), the learning of important presentation skills and the never-ending personal support – including being my PhD advisors. If they – and of course the director of the Institution, *Attila Demény* – had not believed in me that it would be possible to bring Arctic climate science to Hungary, I would not have been able to start my PhD. I must also express gratitude to *Timea Haszpra* and *Matyas Herein*, who co-advised on my master's thesis and from whom I learnt and with whom explored new perspectives how anthropogenic external forcing causes changes in internal modes of atmospheric circulation.

Over the past three-to-four years I received support from the National Research Development and Innovation Fund, including four New National Excellence Program grants (UNKP-19-3-II; UNKP-20-3-I; UNKP-21-3-II; UNKP-22-4-I), the Co-operative Research Program (KDP-5-3/PALY-2021) and a bilateral research grant (2019-2.1.11-TÉT-2020-00114), which projects drove further my scientific interests and career.

Overall, in my PhD thesis work I focus on understanding atmospheric drivers of Arctic climate changes on interannual, decadal and multidecadal-to-centennial time scales by combining paleoclimatic proxy data, observational and modelling analyses. This dissertation is a summary of 4 lead-author papers which I wrote between 2019-2022. The four individual papers cover four main topics ((i) atmospheric drivers of Arctic sea-ice and (ii) the Greenland ice sheet melt, (iii) Arctic climate sensitivity and (iv) Central European hydroclimate projections. *To distinguish my own work from the one we did with my co-authors, I will use "I" when referring to what I personally did and "we", for those instances that are results of a team-effort.*

LIST OF ABBREVIATIONS

AA – Arctic amplification
acab – accumulation and ablation rate
AMO – Atlantic Multidecadal Oscillation
ASI – Arctic streamfunction index
CanESM-LE – Canadian Earth System Model Large Ensemble
CERES - Clouds and the Earth's Radiant Energy System
CESM – Community Earth System Model
CISM – Community Ice Sheet Model
CMIP – Coupled Model Intercomparison Phase
CSIRO-LE – Commonwealth Scientific and Industrial Research Organization Large Ensemble
EBAF – Energy Balance and Filled
ECMWF – European Centre for Medium range Weather Forecast
EKF400 – Ensemble Kalman Fitting paleo-reanalysis 400
EOF – empirical orthogonal function
ERA-I - ECMWF Interim atmospheric reanalysis
ERA20C - ECMWF 20th century atmospheric reanalysis
ERA5 - ECMWF atmospheric reanalysis version 5
ERSST – Extended Reconstructed Sea Surface Temperatures
GBI – Greenland blocking index
GCM – global climate model
GFDL-LE – Geophysical Fluid Dynamics Laboratory Large Ensemble
GrIS – Greenland ice sheet
GSI – Greenland streamfunction index
IMBIE – Ice sheet Mass Balance Intercomparison Exercise
IPCC – Intergovernmental Panel on Climate Change
IPO – Interdecadal Pacific Oscillation
JJA – June-July-August
LMR – Last Millennium Reanalysis
LW – longwave radiation
MAR – Modele Atmospheriqe Regional
MCA – maximum covariance analysis
MPI-GE – Max Planck Institute Grand Ensemble
NASA – National Aeronautics and Space Administration SIA
NOAA20C – National Oceanic and Atmospheric Administration 20th century reanalysis
NSIDC – National Snow and Ice Data Center
ORAS5 – Ocean Reanalysis System 5
PAGES2k – Past Global Changes 2k
PDD – positive degree day
PDO – Pacific Decadal Oscillation
PI – pre-industrial
PR - precipitation
RCM – regional climate model
RCP – representative concentration pathway
SAT – surface air temperature
SIA – sea-ice area
SIC – sea-ice concentration
SIE – sea-ice extent
SMB – surface mass balance
SMILE – single model initial-condition large ensemble
SSP – shared socioeconomic pathway
SST – sea surface temperature
SW – shortwave radiation
T - temperature
U – zonal wind component
V – meridional wind component
Z – geopotential height

1 INTRODUCTION

Anthropogenic activities advance the level of CO_2 concentrations in the atmosphere at a rate of approximately 1% per year. This constitutes a time-dependent external radiative forcing on the climate system (Peters et al. 2020). Associated changes in the global mean surface temperature are likely to have emerged from unforced natural processes of the climate system i.e., from internal variability (Hawkins et al. 2020). The dramatic reduction in boreal summer (June-July-August, JJA) Arctic sea-ice cover and thickness as well as the melting of the Greenland Ice Sheet (GrIS) since the 1990s have become iconic symbols of on-going climate change (Vaughan et al, 2013). The emergence of regional forced changes from the underlying 'noise' in the Arctic is less certain (Ding et al. 2014;2017;2019; [1]; *Topál et al. 2022; Topál and Ding in prep*), nonetheless, a significant – yet uncertain – portion of the observed Arctic warming is undoubtedly attributable to anthropogenic forcing and its associated positive feedbacks, collectively known as Arctic amplification (Deser et al, 2010; Screen and Simmonds, 2010; Simmonds, 2015; Notz and Stroeve, 2016; Jahn, 2018; Screen et al, 2018).

Key goals of this dissertation are to gain better understanding of internal versus forced changes in the Arctic (**Sections 1.1 and 1.2**) and to point out existing model limitations that are of pivotal importance to better constrain future projections of Arctic sea-ice (**Section 1.3**), global sea-level rise (**Sections 1.2 and 1.3**) and Central European precipitation projections (**Section 1.4**) through the viewpoint of papers published by me and my colleagues.

[1] Research papers that I first- or co-authored are in italics.

1.1 Summer Arctic sea-ice changes

Drivers of sea-ice changes associated with natural variability have been suggested to originate from both oceanic (Zhang, 2007; Tokinaga et al, 2017) and atmospheric processes (Lee, 2012; Notz, 2014; Swart et al, 2015; Grunseich and Wang, 2016; Ding et al, 2017; Wernli and Papritz, 2018; Labe et al, 2019; Olonscheck et al, 2019). Existing linkages between observed Arctic JJA atmospheric circulation anomalies – featuring a low-frequency trend toward mid-to-upper-tropospheric anticyclonic wind anomalies above Greenland and the Arctic Ocean – and September sea-ice variability over the past four decades are apparent (Ding et al, 2017;2019). This circulation pattern resembles a barotropic anticyclone favouring a surface friction-driven top-down adiabatic warming and moistening process, which manifests as the primary physical mechanism behind the local atmosphere-sea-ice causal interactions (Ding et al, 2017;2019).

Previous studies attributed 40-50% of the observed summer sea ice melting since 1979 to this internal atmospheric process (Ding et al. 2019; Ding et al. 2022; Roach and Blanchard-Wrigglesworth, 2022). Not only local processes, but internal sea surface temperature (*SST*) variability residing in the tropical Pacific can also have substantial impact on Arctic climate (Ding et al, 2014; *Baxter et al. 2019*; Screen and Deser, 2019). Observational and modelling evidence suggest causal links between both tropical Pacific (*Baxter et al. 2019*) and Atlantic (Meehl et al. 2018; McCrystall et al. 2020) SST anomalies and Arctic sea-ice variability in a form of Rossby wave-trains emanating from the tropics and thus bridging the Arctic with the lower latitudes. *Baxter et al. (2019)* highlights that a recent cold SST anomaly in the east-central tropical Pacific (especially over 2007-2012) may act as a source for Rossby-wave trains to propagate into the Arctic and manifest as an anomalous high-pressure over the Arctic Ocean. This high-pressure plays a key role to

physically link September sea-ice variability with tropical *SST* changes (Ding et al, 2017;2019).

Remote drivers of Arctic sea-ice variability remain elusive for the summer IPO-Arctic linkage in climate models is different from that in observations. Two independent studies consistently imputed an important role for Pacific decadal variability in driving accelerated Arctic warming and proposed that the transitioning of the Interdecadal Pacific Oscillation (IPO) from cooling to a warming phase can exacerbate sea-ice loss (Svendsen et al. 2018; Screen and Deser 2019). While observations suggest an out-of-phase relationship between tropical and Arctic surface temperature trends (*negative* tropical *SST* changes are associated with *positive* Arctic *surface temperature* changes (*Baxter et al. 2019*; Ding et al. 2019)), Coupled Model Intercomparison Project phase 5 (CMIP5, Taylor et al. 2012) historical simulations feature an opposite pattern (*positive* tropical *SST* trends fall in line with *positive* Arctic *surface temperature* trends). In addition, Blanchard-Wrigglesworth and Ding (2019) recently realized that summertime tropical-Arctic linkages are quite weak in magnitude in one state-of-the-art model (Community Earth System Model v1, CESM1; see Figure 11 in Blanchard-Wrigglesworth and Ding (2019)). The complexity of tropical-Arctic linkages is further exemplified by atmosphere-only model relaxation experiments (Ye and Jung, 2019) and by Bonan and Blanchard-Wrigglesworth (2020) who recently proposed that the relatively short observational record may hinder us from fully understanding the stationarity of tropical-Arctic linkages. **These recent results highlight the complexity of driving factors leading to Arctic sea-ice melt and motivated my PhD to explore the driving mechanisms from new lens and, in particular, assess how previously identified atmospheric processes are represented across multiple large ensemble simulations[2].**

[2]*The aims that shape the main thread of this dissertation are indicated with* ***bold*** *letters.*

1.2 Summer GrIS changes

The GrIS is the single largest contributor to barystatic sea-level rise (Muntjewerf et al. 2020; Hofer et al. 2020). Similar to Arctic sea-ice, it exhibits symptoms of accelerated ice loss (Briner et al. 2020; Fettweis et al. 2020; Hanna et al. 2020; Hofer et al. 2020; IPCC 2021) with serious climatic and ecological consequences. The anthropogenically-forced response – multi-model means, or single-model large ensemble means – of GrIS surface conditions in CMIP5/6 climate models is mostly consistent with surface temperature and mass balance changes derived from satellite-based observations and reanalyses (Fettweis et al. 2020; The IMBIE Team 2020; Slater et al. 2020; Noël et al. 2021). Thus, the melting of the GrIS has become a key indicator of human influence on the climate system. Nevertheless, concerns have also been raised that the underlying physical mechanisms responsible for enhanced GrIS melting may differ in observations and models, hence models might produce a portion of GrIS warming for wrong reasons (Hanna et al. 2020; Delhasse et al. 2021; *Topál et al. 2022*). In particular, previous studies suggest that the observed increase in the frequency and persistence of anticyclonic circulation (blocking) anomalies since about 1990 – similar process to the one that drives sea-ice melting – has contributed to enhanced GrIS melt over the last three decades (Fettweis et al. 2013; Ballinger et al. 2018; Delhasse et al. 2018; Bevis et al. 2019; Hanna et al. 2021). However, climate models (both single-model ensembles (*Topál et al. 2020a*) and individual models (Hanna et al. 2018; Ballinger et al. 2018; Delhasse et al. 2021; Luo et al. 2021)) fail to depict changes in blocking conditions associated with surface temperature warming around the GrIS. This highlights existing discrepancies between the mechanisms causing GrIS melt in the observational and model worlds with ramifications for the reliability of estimates targeting the GrIS's sensitivity to anthropogenic forcing (Hofer et al. 2020; Slater et al. 2020). **Based on the above arguments, I plan to dive deeper and aim to provide**

a better understanding of the mechanisms responsible for accelerating GrIS melting in observations and multiple climate model simulations.

Anthropogenic emissions driven diabatic warming – i.e., radiative forcing, which is further amplified by the surface-albedo feedbacks in the ablation zone and widespread cloud radiative effects (Bennartz et al. 2013; Tedesco et al. 2016; Van Tricht et al. 2016; Zelinka et al. 2020) – and processes related to large-scale atmospheric and oceanic circulation variability together shape the recent changes of the GrIS (Fettweis et al. 2013; Hanna et al. 2013; Tedesco and Fettweis 2020; Ding et al. 2017; Hermann et al. 2020; Sherman et al. 2020). Regarding the physical mechanisms, circulation-driven surface friction is key to creating adiabatic warming around the core of the anticyclone, which together with advective effects cause enhancement of longwave radiation anomalies (in both components of the longwave radiation: clear-sky and cloud radiative) in the lower troposphere (Tedesco et al. 2016; Van Tricht et al. 2016; Hofer et al. 2017; Noël et al. 2017; Huang et al. 2021). Synchronously, beneath the centre of the high-pressure, clear skies favour incoming shortwave radiation anomalies that tend to amplify GrIS surface melt especially in coastal regions with their lower albedo (Bennartz et al. 2013; Bevis et al. 2019; Hofer et al. 2019). Current understanding thus suggests that GrIS surface conditions are determined by a quantitatively yet uncertain combination of (i) atmospheric circulation changes primarily via the aforementioned adiabatic warming process and (ii) anthropogenic diabatic warming, which may also induce circulation changes due to proportional relationships between air temperature and pressure. Nonetheless, previous analyses of state-of-the-art climate model simulations indicate weak Arctic wind changes in response to anthropogenic forcing and suggest forced temperature changes that are vertically rather uniform in the summer season (Ding et al. 2017; *Topál et al. 2020a*). Although one cannot rule out that model biases impact the forced temperature response in

the Arctic, the observed mid-to-upper-level wind-driven process, which causes vertically non-uniform temperature changes, is an acknowledged contributor in shaping GrIS surface conditions during recent decades (Fettweis et al. 2013; Ballinger et al. 2018; Delhasse et al. 2018; Bevis et al. 2019; Hanna et al. 2021).

I find the separation of the above two processes based on their corresponding vertical temperature response appealing, which I will use to showcase advantages of wind-nudging simulations described below (in Section 2.8).

1.3 Arctic climate sensitivity bias

Based on observed rapid changes in the Arctic cryosphere, it has been suggested that the Arctic is 'en route' to a new state (Landrum and Holland 2020) that may trigger a cascade of tipping points (Serreze 2011; Notz and Stroeve 2016; Boers and Rypdal 2021). Nevertheless, despite tremendous research efforts over past decades, mechanisms of Arctic amplification (Serreze et al. 2006; AA) and Arctic climate change are still difficult to pinpoint (Stroeve and Notz 2015; Goosse et al. 2018; Previdi et al. 2021; Moritz et al. 2022), especially in the melting season (Wernli and Papritz 2018; Huang et al. 2021) **(Sections 1.2 and 1.3)**. One key uncertainty is the lack of confidence in the modelled sensitivity of Arctic sea-ice and the GrIS to increasing atmospheric CO_2 concentrations (Stroeve et al. 2007; Winton 2011; Li et al. 2013; Notz and Stroeve 2016; Rosenblum and Eisenman 2017) (usually defined as a certain amount of ice melting corresponding to a unit of CO_2 emission; DeRepentigny et al. 2022). This partially results from our limited understanding of the importance of internal variability in contributing to observed Arctic warming over the past decades (Swart et al. 2015; Jahn et al. 2016; Delhasse et al. 2018; Ding et al. 2019; England et al. 2019; Boers and Rypdal 2021; Bonan et al. 2021).

If the observed Arctic warming is in part due to internal processes (Swart et al. 2015; Jahn et al. 2016; Ding et al. 2017; Meehl et al. 2018; *Topál et al. 2020a*; Chylek et

al. 2022;) – exemplified by the halt in the acceleration of sea-ice melting (*Baxter et al. 2019*; Francis and Wu 2020) and GrIS melting (Bevis et al. 2019) between 2013-2020 –, then the simulated forced response should not be expected to capture the total observed signal. Otherwise, a mismatch between Arctic warming in response to CO_2 forcing in models and observations may be suspected, which is likely attributable to not comprehensive-enough physics in models (Fyfe et al. 2013). Different views on the role of internal variability lead to diverse perspectives about models' sensitivity in the Arctic, which undoubtedly obstructs reliable projections of forthcoming pathways of the Arctic environment in response to climate change and hinder associated adaptation and mitigation planning. This year (2022) urgent concerns have been raised highlighting that one quarter of the models in CMIP6 have higher sensitivity to CO_2 forcing than any of those in CMIP5, even to an extent not supported by paleoclimatic evidence (Tokarska et al. 2020; Zhu et al. 2020; Hausfater et al. 2022). This tendency of CMIP6 models becoming 'hotter' in a global scale can be further amplified in the Arctic considering that AA processes are well simulated in most models (Hahn et al. 2021; Holland et al. 2021). It remains unclear whether these 'too hot' models are consequent of improvements in models' physics (Notz and SIMIP Community 2020; Zelinka et al. 2020), or it indicates that models are biased too warm when driven by high levels of atmospheric CO_2 (Zhu et al. 2020). However, it is important to note that regardless of changes in sensitivity to emissions, CMIP5 and CMIP6 models share limitations in representing the complex local Arctic processes and teleconnections at play, in particular for atmosphere-ocean-sea/land-ice interactions (Ding et al. 2017; Hanna et al. 2018; Ding et al. 2019; *Topál et al. 2020a*; Delhasse et al 2021) and their linkages with large-scale circulation changes driven remotely (Meehl et al. 2018; *Baxter et al. 2019*; *Topál et al. 2020a*).

Hofer et al. (2020) showed that improvements in CMIP6 models, partially related to better radiative (cloud) feedbacks (Zelinka et al. 2020), led to simulating unprecedented GrIS melting rates by 2100 even without substantial improvements in modelling connections of large-scale circulation with local warming processes in the Arctic and over Greenland (Hanna et al. 2018; Delhasse et al. 2021; Luo et al. 2021). Hence, identifying those CMIP5/6 models that have a better representation of Arctic atmospheric circulation – even if these models are currently regarded as 'low sensitivity models' (Zhu et al. 2020) – may help to provide alternative, dynamically-coherent future GrIS climate projections that can enable more effective adaptation and mitigation plans to sea-level rise.

I aim to further explore (in Section 3.3) consequences of a discrepancy between observations and models of upper-tropospheric circulation-driven Arctic sea- and land-ice changes. I focus particular attention to a possible *delay* in the timing of the first sea-ice free September and widespread GrIS melting across hundreds of available simulations as a consequence of a low sensitivity of the models to large-scale circulation driven Arctic warming.

1.4 Central European hydroclimate projection uncertainties

Model uncertainties affecting regional Central European hydroclimate projections are of similar importance to those of hindering forthcoming pathways of Arctic climate change. In particular, uncertain projections of future precipitation changes may put a break on effective regional policymaking especially agricultural adaptation plans. Despite regional climate models tend to project less summer precipitation in the coming decades, observationally constrained global climate models (GCM) in Central Europe agree less on future drying in our region (**Section 3.4**). This topic is of prime importance, since East-Central Europe is believed to become more susceptible to the incidence of climate extremities in response to increased radiative forcing (Seneviratne et al. 2006; Bartholy and

Pongrácz 2007; Beniston et al. 2007; Hirschi et al. 2010). GCMs are elaborate tools for simulating past, present and future climatic and environmental changes on various timescales, however, any projection is riddled with three commonly mentioned uncertainties: scenario uncertainty, model uncertainty and internal variability (Stainforth et al. 2007; Knutti 2008; Hawkins and Sutton 2009). One practice to acknowledge GCM limitations is to use a multi-model ensemble (Suh et al. 2012; L'Heureux et al. 2017) and consider each GCM with equal weight. However, to abandon 'model democracy' (Knutti 2010) and weight or give preference to certain models in a multi-model ensemble based on performance ranking was also proposed (Merrifield et al. 2019). The latter has proved effective in constraining model uncertainty (Knutti et al. 2017) and is of particular importance when studying climatic variables (e.g., precipitation) whose future projections show large spread between different models (Garfinkel et al. 2020).

Several studies indicate that structural differences, namely the land-atmosphere feedback strength, between models can indeed be a source of uncertainty in future precipitation projections (e.g., Schwingshackl et al. 2018). However, the exact physical mechanisms such as, how changes in soil moisture affect precipitation or temperature extremes remain uncertain (Boberg and Christensen 2012; Taylor et al. 2012a; Berg et al. 2016). Based on CMIP5 models with more realistic land-atmosphere couplings future *reduction* in summer drying and warm extremes in Central Europe were highlighted (Vogel et al. 2018; Selten et al. 2020).

How internal variability may influence the selection of best performing models and thus the uncertainty in future precipitation projections have remained unaddressed. Single model initial-condition large ensemble (SMILE; Deser et al. 2020) simulations offer new perspectives in this regard. Within the CMIP5 multi-model ensemble one cannot estimate the relative role for internal variability and model structural differences in influencing the

spread of future precipitation projections since, for example, land-atmosphere feedbacks appear with different precision in the 31 CMIP5 models (Cheruy et al. 2014). However, with the inclusion of SMILEs new opportunities open: **I aim to explore the range of future precipitation projections solely due to internal variability (per model) and thus place CMIP5 model structural differences in the context of internal variability when assessing future hydroclimate projection uncertainties.**

1.5 Aims

A_1: To explore driving mechanisms of sea-ice loss from new lens and, in particular, assess how previously identified atmospheric processes are represented across multiple large ensemble simulations.

A_2: To dive deeper and provide a better understanding of the mechanisms responsible for accelerating GrIS melting in observations and multiple climate model simulations.

A_3: To separate GrIS warming processes based on their corresponding vertical temperature change profiles and showcase advantages of wind-nudging simulations.

A_4: To explore consequences of a discrepancy between observations and models of large-scale circulation-driven Arctic sea- and land-ice changes, in particular, a possible *delay* in the timing of the first sea-ice free September and widespread GrIS melting.

A_5: To explore the range of future precipitation projections due to internal variability and place CMIP5 model structural differences in the context of internal variability when assessing future hydroclimate projection uncertainties.

2 MATERIALS AND METHODS

The data and methods corresponding to the four main topics outlined in the Introduction are presented below in one coherent section.

2.1 Reanalyses, surface energy balance, sea surface temperature and ocean temperature data

In an effort to address **A_1**, I use monthly geopotential height (*Z*) and temperature (*T*) data at 27 pressure levels and the surface air temperature (*SAT*) variable from the European Center for Medium Range Weather Forecasting (ECMWF) reanalysis ERA-Interim (ERA-I) (Dee et al, 2011) (in **Section 3.1**). Despite uncertainties between different reanalysis data sets, Ding et al. (2017) showed that ERA-I well reproduces the radiosonde measurements in and around the Arctic, therefore I compare the models to ERA-I. I also use global 300-hPa and 500-hPa horizontal winds (*U, V*) and *SAT* from the ERA5 reanalysis (Hersbach et al. 2020) (1979-2020), the ERA 20th century reanalysis (Poli et al. 2016; ERA20C) (for the period of 1900-2014) and the NOAA 20th century reanalysis version 3 (Compo et al. 2011; Slivinski et al. 2019; NOAA20C) (for the period of 1835-2010) when exploring **A_2**, **A_3** and **A_4**. While working towards the goals of **A_2** and **A_3,** I also use the Extended Reconstructed Sea Surface Temperature (ERSST) dataset version 5 (Huang et al. 2018; ERSSTv5) from 1979 to 2020 and the Clouds and the Earth's Radiant Energy System (CERES) Energy Balanced and Filled (EBAF; Kato et al. 2018) edition 4.1 monthly means of surface net long- and shortwave radiation (LW and SW, respectively) for a satellite-based, simplified estimate for Greenland surface energy balance (excluding latent and sensible heat fluxes, indicated by *SEB** in Eq. 1) for the period 2001-2020 (in **Sections 3.2 and 3.3**).

$$\mathrm{SEB}^{*} = (\mathrm{LW}_{net} + \mathrm{SW}_{net})_{surface} \qquad \text{(Eq. 1)}$$

EBAF is considered to be a leading benchmarking tool for evaluating the Arctic radiative budget in model simulations (Loeb et al. 2018). For **A_2** and **A_3**, I also use potential temperature from the ORAS5 ocean reanalysis product (Zuo et al. 2019).

2.2 Paleo-reanalyses and ice core and oceanic proxy data

I reduce uncertainties arising from the relatively short observational records, to meet aims **A_2** and **A_3** (**Section 3.2**) and utilize two paleoclimatic data assimilated climate model experiments (so-called paleo-reanalyses), the Ensemble Kalman Fitting (EKF) 400 version 2 (Valler et al. 2021) and the Last Millennium Reanalysis version 2.1 (Tardiff et al. 2019). Both products assimilate early instrumental observations along with proxy data including tree ring, coral and sedimentary archives, but only the LMR2.1 assimilates ice cores from the GrIS. For assimilated data details see Valler et al. (2021) and Tardiff et al. (2019). I primarily focus on the EKF400 and its timescale (1602-2003 AD) because of slight differences in available variables from the two reanalyses; the advantage of EKF400 is that it provides horizontal winds at 200hPa to calculate streamfunction from, which is a key metric used to measure circulation-driven changes over the Greenland ice sheet (see further details below in **Section 2.10**). The reason why I apply these extended reanalysis datasets is to provide evidence for the consistency of observed circulation driven GrIS climate variability over centennial timescales. I further utilize 30 Greenland ice core records (with record lengths varying between 194 and 384 years) from the Iso2k database (Konecky et al. 2020) that are *not* assimilated in the EKF400 and 33 oceanic coral records (Supplementary Table 1) from PAGES2k Consortium (2017) that *are* assimilated in the EKF400 as the basis of observational constraints when evaluating the EKF400 simulated past 400 years Greenland surface temperatures and the tropical-Arctic teleconnection in Figure 3.2-10b,d. I have selected the ice core and coral proxy records that were available with at least annual resolution. When comparing the maximum covariance analysis (MCA)

expansion coefficient time series derived from the EKF400 (see details on the MCA below in **Section 2.6**) to known decadal *SST* variability indices, I compute the Pacific Decadal Oscillation (PDO*) index along with the Atlantic Multidecadal Oscillation (AMO*) index from the EKF400, marked with an asterisk in the text. The PDO* is defined as the first principal component time-series of the EOF of SST poleward of 20ºN, while the AMO* is the spatially averaged SST in the North Atlantic basin over 0-80ºN after having removed the global mean SST (for both the PDO* and AMO*).

2.3 Observational sea-ice, GrIS mass balance and 'Modele Atmospheriqe Regional' (MAR) surface mass balance simulations

Throughout the text, sea-ice data is derived from the National Snow and Ice Data Center (NSIDC) Climate Data Record of Passive Microwave sea ice concentration (SIC), version 3 of the NSIDC (Cavalieri et al, 1996). When working towards the goals of $\mathbf{A_1}$ and $\mathbf{A_4}$ (**Sections 3.1** and **3.3)** I calculate sea-ice area (*SIA*) as the product of ice concentration and grid element area in each sea-ice grid. Then – following the definitions of the NSIDC – the September total sea-ice area index (*SIA* index) is constructed as the sum of sea-ice area in all Arctic (poleward of 60ºN) grid cells where ice concentration is greater than 15%. Given the sensitivity of sea-ice's annual minimum to climate variability in the Arctic, I focus on the September total *SIA* index from observations and each of the model simulations when examining the atmospheric drivers of sea-ice variability. To derive insights on possible delays in the timing of the first sea-ice free September ($\mathbf{A_4}$**, Section 3.3**) I calculate sea ice extent (*SIE*) as the sum of grid element area in each sea ice grid with at least 15% of ice concentration in the Arctic (poleward of 60ºN). Note, that the difference between *SIA* and *SIE* is that *SIA* considers the actual ice concentration in a grid cell, while *SIE* is more like an overall measure of ice extent. Thus, *SIA* is a more realistic measure of sea-ice, however one must also acknowledge ice-concentration measurement biases

originating from the passive microwave sensor on satellites when deciding which sea-ice index to use. The most common definition of the timing of the first "sea-ice free summer" refers to a future time point at which September *SIE* falls below one million square kilometres (Laliberté et al. 2016; Wang et al. 2009).

In an effort to fulfil the goals of $\mathbf{A_2}$ and $\mathbf{A_3}$ (**Sections 3.2** and **3.3**), I also use data from the Ice Sheet Mass Balance Inter-comparison Exercise (IMBIE) 2019 Greenland Dataset as the satellite-based observational estimate of ice mass changes in the GrIS over the period of 1980-2018 (The IMIBE Team 2020). The dataset represents reconciled mass balance estimates from three independent satellite-based techniques (gravimetry, altimetry and input-output method) (for more details see The IMBIE Team (2020)). In addition, I use surface mass balance (*SMB*; Eq. 2) and *SAT* output from the MAR, which is a regional climate model (Gallée et al. 1994) specifically designed and physically optimized for polar areas (Amory et al. 2015).

$$\mathrm{SMB} = \mathrm{precipitation}_{\mathrm{total}} - \mathrm{runoff}_{\mathrm{meltwater}} - \mathrm{sublimation/evaporation} \quad \text{(Eq. 2)}$$

The MAR combines atmospheric modelling (Gallée et al. 1994) with the Soil Ice Snow Vegetation Atmosphere Transfer Scheme (Fettweis et al. 2017) and has been thoroughly evaluated and used to simulate surface energy balance and mass balance processes over the GrIS (Fettweis et al. 2011; Fettweis 2007). I use model version 3.11 6-hourly forced at its lateral boundaries (temperature, specific humidity, wind speed, pressure, sea surface temperature, and sea ice concentration) by ERA5 reanalysis at 1×1 km^2 spatial resolution. I use monthly output during the 1980-2020 period. The MAR *SAT* fields are considered to be the closest match (relative to ERA-I or ERA5 reanalyses) to satellite observed GrIS surface temperatures (Delhasse et al. 2020).

2.4 Model experiments: large ensembles, pre-industrial & historical simulations in CMIP5/6

Internal variability is an inherent feature of the climate system. When creating SMILEs, unlike the CMIP5/6 ensemble, the same model is run several times with small perturbations in the initial condition, thus the single runs – that share the model physics and the external forcing – are considered parallel realizations of the same model. In this way internal variability and the forced component are separable *within* a certain model, which is an advantage over using multi-model simulations when exploring internal processes in the climate system (Drótos et al. 2015).

When working towards the goals set forth in $\mathbf{A_1}$ to $\mathbf{A_5}$, I utilize six currently available CMIP5/6 SMILEs of fully coupled Earth System Models collected by the US CLIVAR Large Ensembles working group (Deser et al. 2020) including (i) the Max Planck Institute 100-member Grand Ensemble (MPI-GE; Maher et al. 2019), (ii) the CanESM2 50-member LE (CanESM-LE) (Kirchmeier-Young et al. 2017), (iii) the CESM1 40-member LE (CESM-LE) (Kay et al. 2015), (iv) the CSIRO-Mk3.6 30-member LE (Jeffrey et al. 2013) and (v) the GFDL-CM3 20-member LE (GFDL-LE) (Sun et al. 2018), in addition to a more recent CMIP6 large-ensemble the (vi) 100-member CESM2 Large Ensemble (CESM2-LE, Rodgers et al. 2021). From the CMIP5 ensembles I use model output for 1979-2099 with CMIP5 historical forcing (Taylor et al. 2012) until 2005 and RCP8.5 forcing 2006 onwards. With respect to the CESM2-LE, I use CMIP6 historical forcing until 2014 (as of the protocol) and the SSP3.-7.0 scenario for 2015-2100. Additionally, I also use the other two available RCP2.6 and RCP4.5 forcing scenarios from MPI-GE for 2006-2099, which allows to examine interactions between internal climate variability and anthropogenic forcing with different intensity. In addition, I utilize historical+SSP5.-8.5 simulations with 29 CMIP6 models (21 CMIP6 models for sea ice) and 31 CMIP5 pre-industrial (PI) control simulations. The pre-industrial runs contain integrations longer than

200 years representing a realization of one individual model. The reason I include these runs to meet $\mathbf{A_1}$ is to assess whether the bias in Arctic teleconnections and atmosphere-sea-ice interactions from the large ensembles are common across all available models in CMIP5/6. In **Section 3.1**, to reduce uncertainty arising from the different model physics, I primarily focus on the mean of four large ensembles (excluding CSIRO-LE, for details see **Section 3.1.1**) and the mean of 31 PI simulations. Before averaging, all model outputs are regridded onto the ERA-I 1.5° regular grid applying the ERA-I land-sea mask.

2.5 Fast-minus-slow composite: a simple but efficient way to distinguish internal from forced variability

Teasing apart internal variability of any observed and simulated variable from its forced component is challenging. To fulfil $\mathbf{A_1}$, making use of the state-of-the-art SMILE simulations, I implement a simple method to separate atmospheric processes originating from internal climate variability from those resulting from the models' forced component. I focus on the spread of September total *SIA* index variable between the members of the ensemble that lets us separate groups of members showing relatively fast and slow melting between 1979-2012 (based on linear trends). I target the historical analysis in **Section 3.1** at the 1979-2012 period when the strongest September sea-ice melting is observed along with remarkable JJA geopotential height rise above Northeast Canada and Greenland (Ding et al, 2014;2017;2019; Mioduszewski et al, 2016). Having identified those members of the fast- and slow-melting groups I average the corresponding linear trends in JJA, e.g., 200-hPa geopotential height (*Z200*), in each group and calculate the difference between the two *Z200* composites. I do the same with zonal mean geopotential height (*Z*), zonal mean temperature (*T*), (*SAT*) and September *SIA*. I refer to the difference of the fast and slow group *Z200* (*Z, T, SAT, SIA*) trends as the **fast-minus-slow** *Z200* (*Z,T,SAT,SIA*) composite. Because all ensemble members are forced in the same way, the fast-minus-slow composites

remove the forced signal and retain signals that originate from fundamental internal atmospheric variability. Since correlation between sea-ice and a given atmospheric variable, assuming linearity, reflects the strength of the coupling between them, I can compare the composite trend patterns to the results obtained from the correlation analysis to determine whether a similar pattern is present over the two timescales. Following Ding et al. (2019), I choose ~15% (approx. 1 standard deviation from the mean) of the total number of ensemble members (members in each group: MPI-GE: 15, CanESM-LE: 7, CESM-LE: 6, CSIRO-LE: 5 and GFDL-LE: 3 members) to the fast and slow groups.

2.6 Maximum covariance analysis and its application to validate the compositing method

To (i) account for possible limitations of the fast-minus-slow composite (in **Section 3.1**) as well as to (ii) assess coupled variability between different climatic fields (**Section 3.2**) I apply maximum covariance analysis (MCA; Bretherton et al, 1992). MCA is used to reveal the maximum coupled variability using singular value decomposition of the covariance matrix between geopotential at a certain pressure level (e.g., 500hPa or 300hPa) and global *SST* or sea-ice variability. I further explore how well the aforementioned fast and slow sea-ice melting groups represent the total ensemble spread of the simulated atmosphere-sea ice interactions. In doing so, first, I calculate linear trends in all members of a given SMILE over 1979-2012 for both JJA *Z200* and September *SIC* within the Arctic (north of 60°N). Second, I remove the ensemble mean trend from each member, so the residual trends of each member only reflect inherent internal variability of a model over the selected time period. To understand how sea-ice and *Z200* are coupled in the Arctic due to pure internal variability, I calculate MCA between JJA *Z200* and September *SIC* trend fields across all the members in a given SMILE similar to Li et al. (2017), hereafter referred to as "inter-member MCA". In this way, the time expansion coefficients will not reflect temporal

changes, rather member series, which I compare to the magnitude of September total *SIA* index linear trend derived from each member. The comparison reveals that the fast and slow melting groups (based on one-standard deviation of linear trends in September total SIA index) show the strongest negative and positive loading in the inter-member MCA. Thus, the fast-minus-slow composite can basically capture the leading mode of co-variability between Z200 and sea ice for 1979-2012 as well as for the future (2020-2050) timeframe as the repeated analysis confirmed (see Haszpra et al. (2020): Figure 3 therein).

2.7 Pseudo-ensemble of pre-industrial CMIP5 simulations

Additionally, in **Section 3.1**, I extend the fast-minus-slow method (**Section 2.5**) to 31 CMIP5 models that have at least 200-yr-long pre-industrial control simulations. Cutting the 200+ year-long control runs into consecutive 34-yr periods I create a pseudo-ensemble with $n - 33$ members, where n is the length of the given CMIP5 model's control run (Rosenblum and Eisenmann, 2017, Ding et al, 2019) and each member corresponds to a 34-yr long time-series (as parallel realizations of the observed 1979-2012 period). The pseudo-ensemble members are not initialized with perturbations in the initial condition and the consecutive members have overlapping periods. Therefore, strictly speaking they do not represent the full scope of possible climate states allowed by internal variability. However, the control runs have constant external forcing thus the members of the pseudo-ensemble are assumed to be generated by the given model's purely internal climate physics. I then search for the 34-yr long periods showing the fastest and slowest sea ice melting based on linear trends and difference the corresponding *Z200* (*Z,T,TS,SIA*) trends to construct the fast-minus-slow composite. Similar to the real-ensemble calculations 15% of the total number of the pseudo-ensemble members for each of the fast and slow groups were selected. Averaging these 31 fast-minus-slow composite patterns I provide an overview of

CMIP5 model performance in capturing the observed coupling of sea-ice with both the local Arctic and remote tropical atmosphere on low-frequency timescales.

2.8 Nudging experiments

2.8.1 Imposing winds in the CESM1 fully-coupled model

First, led by Qinghua Ding at the University of California Santa Barbara, the fully-coupled CESM1 (including atmosphere (CAM5), ocean (POP2), sea ice (CICE4) and land (CLM4.5) components) was used to conduct nudging experiments to explore and quantify the influence of circulation changes on the GrIS. 6-hourly zonal and meridional winds from ERA5 were used to constrain the Arctic (>60ºN) circulation in the CESM1 from the surface to top-of-atmosphere while keeping all external forcing agents (solar, GHG, aerosols, etc.) constant at their year 2000 levels. As shown by previous studies (Huang et al. 2021; Li et al. 2022), the response of CESM1 to nudging winds is insensitive to how winds are imposed in the low levels of the model. During the nudging procedure, simulated winds are relaxed in each time step to corresponding ERA5 winds (interpolated from 6-hour interval to model time steps (1800 seconds)) by adding an additional tendency term in the momentum equations, which is calculated as the difference between ERA5 winds and models' winds at each grid in each step. In these experiments, full nudging is utilized so that zonal and meridional winds are forced to vary *exactly* as observed in the model within the Arctic. In this way, the simulations *perfectly* 'replay' observed circulation variability in the Arctic atmosphere while other components of the model solely respond to these specified wind changes. In addition, a long spin-up run is conducted before the 10-member nudging runs to ensure that the nudging simulation has no significant 'numerical shock' in the early period when reanalysis winds are suddenly added in the Arctic. To do so, a 150-year long external forcing-fixed (at year 2000 levels) nudging simulation is performed with the model perpetually nudged to winds of year 1979 in the Arctic in the same setting as what was

used in the 10-member nudging runs. 150 years was deemed an adequate period for the model to well adjust to perpetually imposed reanalysis winds (year 1979) in the Arctic and to reach an equilibrium state. The model states on 1 January of the last 10 years of this spin-up are then used as initial conditions to reinitiate a set of new 10 members of 42-yr nudging simulations in which nudged winds in the Arctic began to vary from 1979 to 2020.

I mainly focus on the ensemble mean of the 10 members in the CESM1 nudging experiments and compare it to the 40-member CESM-LE. This comparison reveals the importance of observed winds in causing the recent acceleration of GrIS melt and corresponding increase in the rate of barystatic sea-level rise relative to simulated GrIS changes in the ensemble-mean (forced response) and the ensemble spread (internal variability) in the CESM-LE, considering that the same model is used to create the nudging simulations to that of the initial-condition large ensemble.

2.8.2 Nudging experiments with the Glimmer-CISM v.1.6 ice sheet model

Second, output fields derived from one member (no. 4) of the 10-member nudging experiments were selected to drive the Community Ice Sheet Model (CISM) Glimmer version 1.6 (Rutt et al. 2009) and the model variable "*acab* = accumulation and ablation rate [m/yr]; land ice surface specific mass balance" was studied as a counterpart for MAR *SMB*. Only one member was selected due to computational limitations. The Glimmer model requires atmospheric 3-hourly (precipitation, solar radiation, temperature, pressure, humidity and winds at the surface) forcing fields that specify the state of the atmosphere and the radiative fluxes above the GrIS. All these 3-hourly forcing fields are generated by CESM1 in which the models' winds are nudged to ERA5 reanalysis in the Arctic (>60ºN). Although the CISM-Glimmer's positive-degree-day (PDD, see details in Section 1.5 in here) scheme relating surface air temperatures to ice melting is insufficient to properly model future climate changes (because the empirical formulae used for present climate may

change under climate change), it is adequate for use in the nudging approach where I only qualitatively investigate circulation driven GrIS accumulation/ablation rates. Since the CISM-Glimmer's "*acab*" approximates the MAR *SMB*, forcing the CISM-Glimmer with a member from the CESM1 fully-coupled nudging simulations enables wind-driven adiabatic Greenland *SMB* changes to be distinguished from diabatic processes. Caveats of the CISM-Glimmer nudging experiment include climatological biases in the simulation of *SMB* and an overestimated melting over the period 1980-2018 compared to MAR (Supplementary Figure 3) that is probably related to known limitations of the CISM-Glimmer such as the only available shallow ice-dynamics and the PDD scheme. In **Section 3.3**, due to data unavailability, I only use *SMB* from the CESM2-LE to compare it with the MAR derived *SMB*, when assessing the *SMB* response to the regional Arctic climate sensitivity bias. In this latter case, note that the CESM2 has an interactive ice sheet model within its land model, therefore the *SMB* calculations are more realistic.

2.9 Greenland and Arctic streamfunction indices (GSI/ASI)

When addressing $\mathbf{A_2}$ to $\mathbf{A_4}$ (**Sections 3.2 and 3.3**), to characterize wind-driven circulation aloft the Arctic and the GrIS, respectively, while synchronously taking into consideration large-scale variability, the mean of the area-weighted 300 or 500hPa streamfunction calculated from the 300 or 500hPa horizontal wind field over the Arctic (>60ºN) and over the GrIS (only land points between 80ºW-20ºW and 59ºN-85ºN) was computed to derive the Arctic/Greenland streamfunction index (*ASI*;*GSI*). I calculate the *GSI* and *ASI* in reanalyses (ERA5, NOAA20C, ERA20C) as well as in model simulations (a total of 340 members of three selected SMILES, see **Section 3.3**) and in 31 CMIP5 and 29 CMIP6 simulations separately using Eq. 3.

$$\nabla^2\Psi = -\xi \qquad \text{(Eq. 3)},$$

where $\xi = \frac{\partial v}{\partial x} - \frac{\partial u}{\partial y}$, is the vorticity of the horizontal wind field.

Also, since by definition the streamfunction $u = \frac{\partial \Psi}{\partial y}$ and $v = -\frac{\partial \Psi}{\partial x}$, it satisfies the horizontal non-divergent criteria i.e., $\frac{\partial u}{\partial x} + \frac{\partial v}{\partial y} = 0$. Thus, the *ASI*/*GSI* measures the rotational (non-divergent) component of atmospheric circulation variability over the Arctic/Greenland and since it explains the majority of large-scale circulation variability in the high latitudes, it exerts a strong force on the temperature field through surface friction-driven adiabatic processes.

The *GSI* and *ASI* represent tropical-extratropical interactions through the following considerations. It can be derived by substituting the weak temperature gradient approximation of the thermodynamic equation (Sobel et al. 2001) into the continuity equation, that tropical diabatic heating generates large-scale horizontal divergence:

$$\nabla \cdot \overline{\boldsymbol{v}}^* \approx \frac{\partial}{\partial p}\left(\frac{Q}{N^2}\right) \qquad \text{(Eq. 4)},$$

where $\boldsymbol{v}$ is the horizontal velocity vector and the overbar donates a time mean, the asterisk the departure from the zonal mean and N^2 is the static stability with Q being the diabatic heating term. Eq. (4) leads to driving *rotational* flow through the vortex stretching term in the stationary eddy vorticity equation (Eq. 5 in Lutsko (2018)). In short, these theoretical considerations motivated the use of the *GSI*/*ASI* when building the arguments described in **Section 3.3.**

2.10 Regression model and Arctic climate sensitivity to CO2

Also in **Section 3.3**, to ensure a fair comparison between the modelled and observed sensitivities of Arctic *SAT* to synchronous changes in upper tropospheric circulation, I linearly regress out the *ASI* (*GSI*) from Arctic (GrIS) SAT index (obtained as

the spatial-averaged SAT values) in ERA5 reanalysis and in a total of 240 SMILE members and in 60 CMIP-class models separately in JJA over 1979-2020. The ratio (*R*) of the linear trends (1979-2020) in the raw and residual SAT time series,

$$R_{SAT}=\left[\frac{residual\ trend\ [K*decade^{-1}]}{raw\ trend\ [K*decade^{-1}]}*100\%\right] \quad \text{(Eq. 5)}$$

is used to quantify the sensitivity of *SAT* to large-scale circulation. To circumvent possible distortions of the correlation in the regression model caused by the underlying anthropogenic forcing induced secular trend, linearly detrended (1979-2020) values of both the *SAT* and *SIE* indices and the *ASI/GSI* were used when creating the regression model. The calculations were repeated without the detrending, which yields a ~15% increase in the difference between the *R* values in observations and in the four model ensemble means. This translates into an extra ~10 years on average in the four model ensembles in terms of the delay of the projected first ice-free September (see **Section 3.3**. for details).

When translating the *SAT*-derived results to sea-ice, first, I create the September *SIE* index in observations, in the three SMILES and in 21 CMIP6 models – which constitute the raw *SIE* index – before linearly regressing out the *ASI* from the raw *SIE* in observations and each of the (single- and multi-model) ensemble members separately to get the residual *SIE* indices. Then I calculate the reduction in *SIE* per a tonne of observed CO_2 emission over 1979-2020 assuming linearity (m^2 of *SIE* change per a tonne of CO_2 emission) in both the raw and residual *SIE* indices to obtain the corresponding *SIE* sensitivities to observed cumulative CO_2 emissions. I repeat these calculations using the MAR and the CESM2-LE simulated GrIS *SMB* indices averaged over the GrIS in the melting season (JJA) and compute the reduction in *SMB* per a tonne of observed CO_2 emission over 1979-2020 assuming linearity (mm water equivalent yr^{-1} of *SMB* change per a tonne of CO_2 emission).

2.11 Observationally constraining the modelled Arctic forced response to CO_2

To reach the goals of **A_4 (Section 3.3)**, I first subtract the 1979 value of the raw *SAT* or *SIE* (GrIS *SMB*) index for each timestep between 1979 and 2100 in each of the SMILE and CMIP6 members to get the change rate of *SAT* or *SIE* (GrIS *SMB*). Then, I time the modelled change rate by the difference between the modelled ensemble mean and the observed *R* values (which is based on the 1979-2020 period) to obtain the constrained change rate of the modelled *SAT*, *SIE* and *SMB*, which is then used to obtain the constrained *SAT*, *SIE* and *SMB* model projections for the 1979-2100 period. In this way all three variables' *R* (Eq. 5) values, respectively, will be identical in the model ensemble means to the observed ones (for the 1979-2020 period). I assume that the ensemble spreads in each of the SMILEs and in CMIP6 do not change with time; the constrained spread changes in accordance with the constrained ensemble mean, which is due to that the modelled forced response underestimates the role of large-scale circulation-driven Arctic warming. This yields the constrained Arctic forced response. When using CMIP6, I assume that the forced response can be derived based on the average of the different models, but I acknowledge that this may be biased due to model interdependency and differences in the model physics (Knutti et al. 2017; Drótos et al. 2015).

Once the raw ensemble mean projection indicates an ice-free Arctic Ocean, the melting rate slows down and the variability between the ensemble members decreases, which is needed to be accounted for when calculating the constrained ice-free dates in the model ensembles. This introduces a physically not plausible slow-down in the constrained *SIE* projections too. Thus, I calculate the excess *SIE* between the constrained and unconstrained ensemble mean *SIE* projections at that time step when the raw projection indicates the first ice-free date (t_{raw_free}). I then interpolate the constrained ensemble mean SIE time series after t_{raw_free} by assuming the same *SIE* melting rate as in the preceding two

decades. I assume that the ensemble spread changes in accordance with the ensemble mean, similar to the calculations for *R* (Eq. 5), as I primarily constrain the forced response. Since the size of the time-window is selected arbitrary, I repeat the calculations using time-windows of size 15 to 25 years. Using different time-windows, the 'likely' probability ($P > 0.66$) of an ice-free date stays within 1 year of our central estimate using the 20-yr long window for the CESM-LE and MPI-GE ensembles, and within 3 years for the CESM2-LE. I attribute this difference to the low sea-ice mean state bias in CESM2 (Kay et al. 2022). I acknowledge this as a caveat to my constraining method, however it very well showcases the delay in the ice-free date due to the oversensitivity issue.

Similarly, I calculate the date when the projected GrIS *SMB* in the CESM2-LE crosses *SMB*=0, which is considered as the turning point of widespread melting. Since I did not see such slow-down as in the case of *SIE*, I simply use the adjusted time series when constraining the date of widespread GrIS melting, similar to the case of the *SAT*.

2.12 Ice-free Arctic CDFs

I compute cumulative probability density functions (CDF) using kernel density estimation (Python package seaborn) based on the histogram of each members' raw ice-free date and the ones obtained by the constraining method (see above) in the three SMILEs and in CMIP6. Similarly, I calculate the CDF of widespread GrIS melting in the raw and the constrained CESM2-LE *SMB* projections and in raw & constrained *SAT* projections corresponding to the date when it first reaches 1ºC, 1.5ºC and 2ºC JJA warming above pre-industrial levels (defined as the period of 1850-1900) in the CESM2-LE, MPI-GE and 29 CMIP6 models. These calculations are meant to exemplify how accounting for the observation-model discrepancy in their corresponding *R* values may cause a change in the modelled probability of the timing of an ice-free Arctic, especially the forced response (the central estimate). Since current CO_2 observations better follow the RCP8.5 or SSP5.-8.5

scenarios, I primarily use those scenario projections when suggesting that it is not likely to see an ice-free September before 2050 (see **Section 3.3**).

2.13 Statistical significance

In Section 3.1 I use the Student's t-test (Student 1908) to calculate significance of both correlations and composite values. Linear trends of time series are removed each time before calculating correlations. Throughout the dissertation, the effective sample size (*N*) is used to determine the statistical significance as computed by

$$N = M * \frac{(1-r_1 r_2)}{(1+ r_1 r_2)}, \qquad \text{Eq. (6)}$$

where r_1 and r_2 are lag-one autocorrelation coefficients of each variable and *M* is the original sample size. A $p = 0.05$ level is used to determine the significance.

2.14 Study area for Central Europe

To address $\mathbf{A_5}$, I use the primary target area consisting of the northeast (NE) and southeast (SE) subregions of the Greater Alpine Region (43°N-50°N; 13°E-19.5°E; Figure 3.4.1), which have been delineated by Auer et al. (2007) based on the regionalization of certain climatic variables. It was chosen to cover the region of interest (East-Central Europe), where precipitation projections of CMIP5 models show large spread for both summer and winter. To ensure the robustness of results based on the primary target area, supplementary calculations were performed on an extended domain (43°N-57°N; 4°E-20°E; Figure 3.4.1) corresponding to the east-central European part of the area used in Vogel et al. (2018).

2.15 HISTALP instrumental data

For the basis of model assessment, I use monthly surface temperature (*TS*) and precipitation (*PR*) data from the HISTALP coarse resolution subregional mean (CRSM)

series for the northeast (NE) and southeast (SE) subregions of the Greater Alpine Region (Figure 3.4-1) for 1861-2005 (Auer et al. 2007).

2.16 Ranking the individual CMIP5 models

As a preliminary step, model output was interpolated onto the same regular 1.5° grid, and anomalies (relative to 1961-1990 to match the HISTALP anomaly time series) were calculated for all the individual historical CMIP5 simulations. Boreal summer (June-July-August: JJA) and winter (December-January-February: DJF) averages were derived annually for both the CMIP5 historical (1861-2005) and future (2006-2100) simulations and the observations of TS and PR. Additionally, both observational and model data were smoothed with a centralized 31-year moving average to mostly account for multidecadal low-frequency variability (as is the standard practice to minimize the effect of internal variability in single model realizations; e.g., McCabe and Palecki 2006; Senftleben et al. 2020) and to ensure comparability to the GCM data with relatively coarse grid resolution. Data preparation resulted in area-averaged and smoothed time series for the two subregions (NE and SE) for each model, variable and season along with the observed time series.

I used three statistics for the individual CMIP5 models' assessment with root-mean square error (*RMSE*) being the primary one in addition to the fraction of temporal Pearson correlation coefficient and mean-absolute error (referred to as: *rank*) and the Nash-Sutcliffe efficiency (*NSE*, Nash and Sutcliffe 1970) calculated between the observed and simulated time series. The reason I include temporal correlation is to measure to what extent simulated long-term (the time series are smoothed with a 31-yr moving average) changes in *PR* and *TS* are in-phase with observations as it is expected for a model to reproduce observed low-frequency *TS* and *PR* changes. The *NSE* (Eq. 7) is calculated based on the observed (obs) and simulated (sim) time series pairs as:

$$NSE = 1 - \frac{\sum_{i=1}^{n}(obs-sim)^2}{\sum_{i=1}^{n}[(obs-(\overline{obs})]^2} \qquad \text{(Eq. 7)},$$

where n is the length of the timeseries and $(\overline{obs})$ indicates the time-mean of the observed time series. The NSE ranges from -∞ to 1, where 1 would mean the perfect observation-simulation match (which is not possible) and $NSE = 0$ indicates that the modeled time series' mean-square-error is commensurable with the variance of the observed time series.

For simplicity I now only go through the ranking steps for the *RMSE* as the calculations are the same for the other two statistics. First, *RMSE* corresponding to each of the two seasons (JJA and DJF) were calculated for both variables (referred to as *TS* and *PR seasonal RMSE*) for the two subregions separately. Then the *RMSE* values were averaged for the two subregions and seasons for the two variables separately (referred to as *mean RMSE* of *TS* or *PR*). I also assess the overall performance of a model in reproducing the observed past hydroclimate variability in the target region and introduce the *grand-RMSE*, which is the average of the *TS* and *PR mean RMSE* values. To ensure comparability of the *RMSE* of *PR* and *TS* I rescaled the values (for both variables) to range between 0 and 1 (Eq. 8) before averaging them into the *grand-RMSE*, which is the arithmetic mean of the scaled *mean RMSE* of *TS* and *PR*.

$$RMSE_{scaled} = \frac{meanRMSE - \min\limits_{m=1,\dots,M}(meanRMSE)}{\max\limits_{m=1,\dots,M}(meanRMSE) - \min\limits_{m=1,\dots,M}(meanRMSE)} \qquad \text{(Eq. 8)},$$

where m goes through the $M = 32$ CMIP5 models (**Table 1**). Note, that the applied rescaling is based on the maximum and minimum values of the *mean RMSE* to maintain the relative differences between each model's performance.

Table 1. 32 CMIP5 models used in $\mathbf{A_5}$ (excluding NorESM1-M (marked with *) for the future timeframe). Expansions/definitions of the models are available online (https://www.ametsoc.org/PubsAcronymList).

CMIP5 MODEL
ACCESS1-0
ACCESS1-3
CanESM2
CMCC-CESM
CMCC-CM
CMCC-CS
CNRM-CM5
CSIRO-MK3.6
FGOALS-s2
GFDL-CM3
GFDL-ESM2G
GFDL-ESM2M
GISS-E2-CC
GISS-E2-H
GISS-E2-R-CC
GISS-E2-R
HadGEM2-AO
HadGEM2-CC
HadGEM2-ES
INM-CM4
IPSL-CM5A-LR
IPSL-CM5A-MR
IPSL-CM5B-LR
MIROC-ESM-CHEM
MIROC-ESM
MIROC5
MPI-ESM-LR
MPI-ESM-MR
MRI-CGCM3
MRI-ESM1
NorESM1-M*
NorESM1-ME

Table 2. Single-model initial-condition large ensemble (SMILE) simulations used in the dissertation.

Modelling center	Model version	Abbreviation	Number of members	Time period	Reference
CCCma	CanESM2	CanESM-LE	50	1950-2080	Kirchmeier-Young et al. (2017)
CSIRO	MK3.6	CSIRO-LE	30	1950-2080	Jeffrey et al. (2013)
GFDL	ESM2M	GFDL_ESM2M -LE	30	1920-2080	Rodgers et al. (2015)
MPI	MPI-ESM-LR	MPI-GE	100	1850-2099	Maher et al. (2019)
NCAR	CESM1	CESM-LE	40	1920-2080	Kay et al. (2015)
NCAR	CESM2*[3]	CESM2-LE	100	1850-2100	Rodgers et al. (2021)
SMHI/KNMI	EC-EARTH	EC_EARTH-LE	16	1850-2080	Hazeleger et al. (2010)

[3] *CESM2-LE is only used in **Section 3.3** due its relatively recent release (2021 October).

2.17 Rank histogram to assess the performance of an ensemble

Additionally, to assess the performance of an ensemble as a whole, I apply the rank histogram on year-to-year seasonal (JJA and DJF) averaged HISTALP and simulated data (Talagrand et al. 1997; Annan and Hargreaves 2010; Maher et al. 2019) for the two SMILEs with sufficiently long historical simulations (MPI-GE and EC_EARTH-LE) and for the CMIP5 ensemble. To do so, let us consider an ensemble with n members and initially let the $rank = 1$. At each time-step (1861-2005) I count the number of members of a given ensemble that are greater than the observed value at that time-step, which can be between $count = 0$ and $count = n$. If $count = 0$, then the $rank = 1$, or if $count = n$, then the $rank = n + 1$, else the $rank = count$. I plot the histogram of the ranks and check for consistency with uniformity based on a chi-squared test (Annan and Hargreaves 2010). If the ensemble underestimates the observed variability, then observations will frequently lie close to, or outside the edges of the ensemble resulting in a u-shaped rank histogram, while a well performing ensemble would yield a flat rank histogram.

3 RESULTS AND DISCUSSION

3.1 An internal atmospheric process determining summertime sea-ice melting in the next three decades and its representation in climate models

This section is based on *Topál et. al (2020a)* addressing A_1.

In **Section 1.1** I highlighted that although internal variability has been acknowledged to play an important role in regulating sea-ice decadal variability in the past (Day et al, 2012; Notz and Marotzke, 2012; Zhang, 2015; England et al, 2019), its relative contribution to the total sea-ice change and how models simulate those processes are still unclear. I was also curious how the interaction between summertime atmospheric and sea-ice changes observed over the historical record behaves under future global warming scenarios. With this I hope to contribute to lessening uncertainties regarding projections of Arctic sea-ice melting in the upcoming decades. Recent studies showed that atmosphere-sea-ice interactions share similar coupling mechanisms on year-to-year and low-frequency timescales in observations (Ding et al, 2017;2019), hence here I focus the analysis on both year-to-year (using correlation analyses in **Section 3.1.1**) and low-frequency (using the fast-minus-slow composite method in **Section 3.1.2**) timescales.

Preceding *Topál et al. (2020a)*, studies had not yet assessed atmospheric circulation driven sea-ice changes in a comprehensive modelling framework including pre-industrial, historical and future simulations of both individual CMIP-class models and SMILEs. I further increased models' diversity by applying a complementary way to explore models' internal variability – in addition to a total of five large ensembles – and utilized a pseudo-ensemble method (**Section 2.7**; Rosenblum and Eisenmann, 2017, Ding et al, 2019) focusing on the pre-industrial control simulations from CMIP5. By comparing the five large ensembles with 31 long (>200 years of integration) control simulations from CMIP5,

the aim was to search for common features of local and remote atmospheric drivers of internal sea-ice variability in the pre-industrial, historical and future simulations.

3.1.1 September sea ice changes in the historical and future warming scenarios

First, I study the interannual variability (Figure 3.1-1a-g) and the long-term trends (Figure 3.1-1h) in the September total *SIA* index (as defined in **Section 2.3**) in observations and model simulations over the instrumental era (1979-2018). The observed prominent rate of melting and interdecadal variability are not well captured in any of the single-model or the CMIP5 multi-model ensemble mean simulations (Figure 3.1-1a; *Baxter et al, 2019*). This readily – yet unsurprisingly – indicates that anthropogenic forcing alone cannot explain the observed total year-to-year variability in the SIA time series and indicates a role for internal variability. Furthermore, the large decline seen in the observed record between 1979 and 2012 lies out of 1.5×interquartile interval (IQI) of four SMILE simulations' spread, except for the GFDL-LE, which shows extensive melting (Figure 3.1-1h). Sources for this underestimation may be rooted in a lower sea ice sensitivity (Rosenblum and Eisenman, 2017; Notz and Stroeve, 2016) of most current climate models or other processes inherent to the climate dynamics, part of which is the subject of the present Section.

I find that the CMIP5 ensemble mean relatively well represents the average of the other SMILE's sea-ice conditions on the historical timeframe, however after the early 2010s four out of five SMILEs (except for the CSIRO-LE) start to melt sea-ice considerable faster than the CMIP5 mean. Out of the five model ensembles, the GFDL-LE and the CanESM-LE indicate the fastest sea-ice retreat since 1979 with ice-free conditions ($<10^6$ km^2) in the near future, while the MPI-GE and the CSIRO-LE mean simulations show more moderate melting (Figure 3.1-1a). The rate of summer sea ice melt in the CESM-LE accelerates after 2012 picturing a seasonally ice-free Arctic Ocean in the model within the next three decades (Screen and Deser, 2019).

After having taken a look at the area-averaged *SIA* change (Figure 3.1-1), in Figure 3.1-2 I demonstrate September sea-ice spatial melting rates in observations (Figure 3.1-2a), in the mean of the 4 SMILE's ensemble mean (excluding CSIRO-LE, Figure 3.1-2b), in the mean of 31 CMIP5 (Figure 3.1-2c) and in each of the five SMILE's historical (Figure 3.1-2d-h) and future (Figure 3.1-2i-m) ensemble mean simulations. In general, on the historical timeframe the mean of four SMILE and the 31 CMIP5 mean model simulations share the observed sea-ice melting spatial pattern, albeit with some differences in the melting trend magnitudes (Figure 3.1-2b-c). As I will show below, although each model exhibits different total *SIA* variability, the coupling patterns of *SIA* with the atmosphere from year-to-year are very similar, indicating that the models' bias in simulating the mean *SIA* is not critical to the determination of the coupling of the atmosphere to sea ice, which is mainly associated with *SIA* anomalies. This finding is consistent with the results based on the composites that are focused on low-frequency sea-ice variability, however, it seems to be *contingent* upon simulating the real summer mean state relatively well. For this reason, I excluded the CSIRO-LE from the multi-model SMILE mean when focusing on the average response of the different SMILEs to anthropogenic forcing.

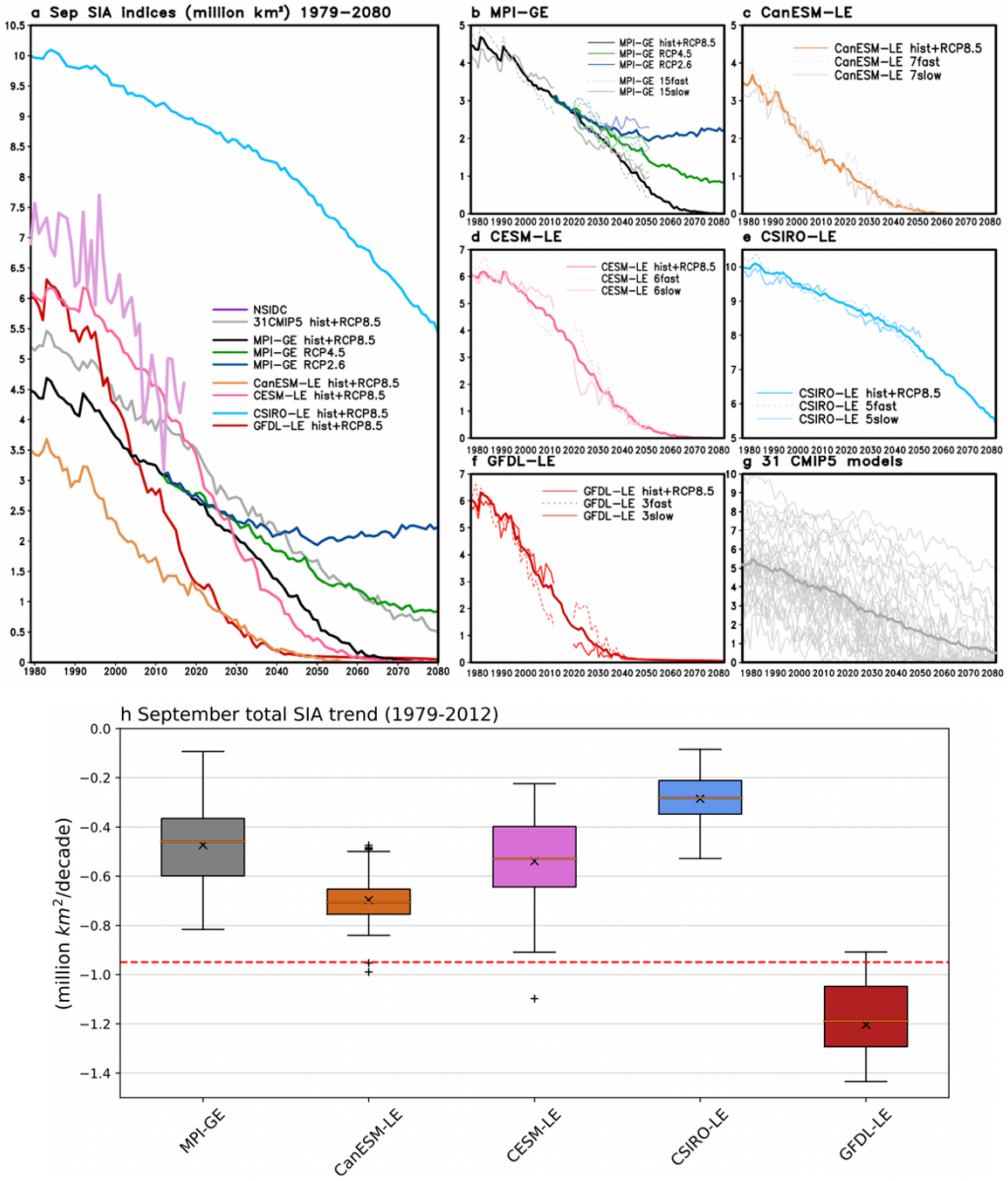

FIG. 3.1-1. Interannual September total sea-ice area variability in observations and model simulations. (a) Time evolution of the observed (1979-2017) (purple), the multi-model ensemble mean of CMIP5 models (grey) and the forced model component of 5 SMILE simulations (ensemble mean) September total sea-ice area (*SIA*) indices (1979-2080) as indicated in the legend (unit: million km^2). Also shown: (b)-(f) time evolution of the ensemble mean (thick solid line), the slow (thin solid line) and fast (dashed line) groups (based on 15% of the total ensemble members) for (b) MPI-GE, (c) CanESM-LE, (d) CESM-LE, (e) CSIRO-LE and (f) GFDL-LE and (g) 31 CMIP5 model *SIA* indices (thin grey lines) and the multi-model ensemble mean (thick grey line). In (h) Box-Whiskers of September total *SIA* linear trends (1979-2012) in the 5 SMILE simulations (indicated below the x-axis) and the observed trend (red dashed line: -0.95×106 km^2 decade^{-1}) is shown. The boxes (h) indicate the interquartile interval (IQI), the whiskers extend up from the top of the box to the largest value less than or equal to 1.5 times the IQI and down from the bottom of the box to the smallest value that is larger than 1.5 times the IQI. Values outside this range are considered to be outliers and are indicated by crosses. The × shows the mean and the horizontal orange line the median (Kovacs et al. 2012). *This Figure is adopted from Topál et al. (2020).*

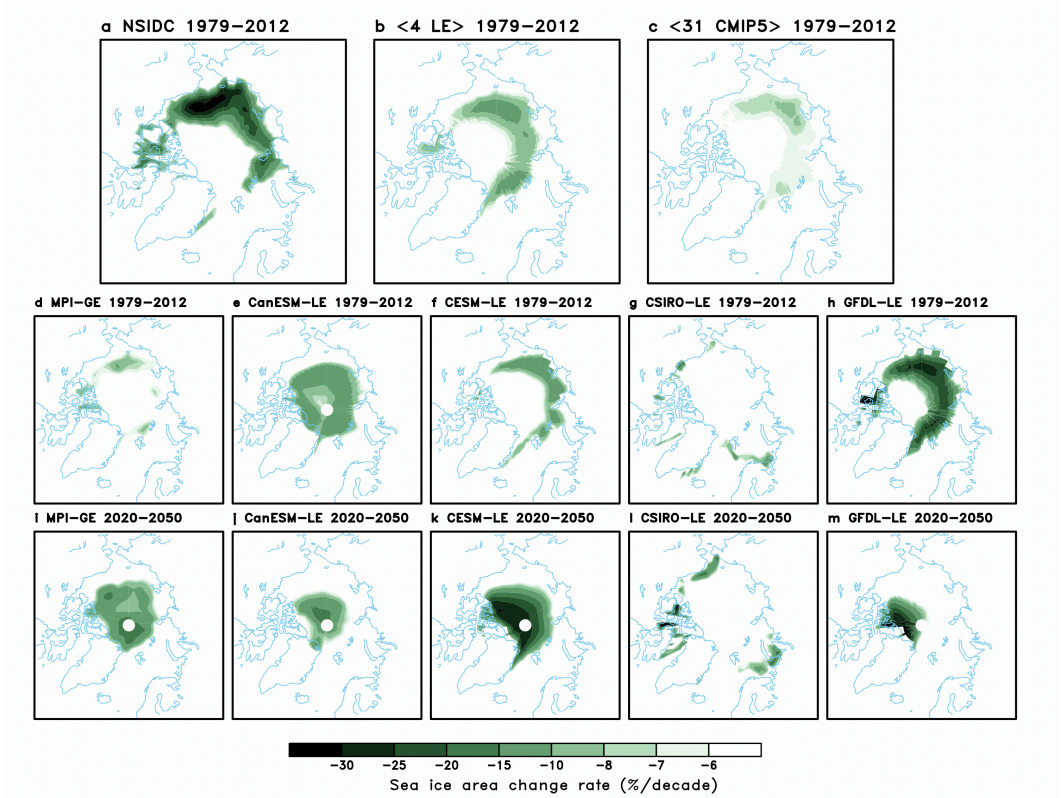

FIG. 3.1-2. Spatial patterns of the linear change rate (% decade^{-1}) in September sea-ice area over 1979-2012 and 2020-2050. Linear trend of September sea-ice area in: (a) observations (NSIDC), (b) the mean (denoted with < >) of the four SMILE's ensemble mean historical+RCP8.5 simulations (excluding CSIRO-LE) and (c) the mean of 31 CMIP5 historical+RCP8.5 simulations for 1979-2012. Also shown: (d)-(m) the same as (a)-(c) but (d)-(h) for the 5 individual SMILE's ensemble mean simulations for 1979-2012 and (i)-(m) for 2020-2050 based on the RCP8.5 scenario. *This Figure is adopted from Topál et al. (2020a).*

3.1.2 Year-to-year atmosphere-sea ice interactions

Observations reveal a recent intensification of an anticyclonic circulation anomaly over the Arctic Ocean, which has warmed and moistened the lower atmosphere resulting in an increase in downwelling longwave radiation (Ding et al. 2019). To better illustrate sea-ice melt anomalies associated with atmospheric circulation changes on the year-to-year timescales, I first computed Pearson correlation between linearly detrended JJA *Z200*, zonal mean geopotential height (*Z*) and temperature (*T*) and linearly detrended September total *SIA* index in ERA-Interim (**Section 2.5**; Figure 3.1-3a-c), in the five model ensembles and in 31 CMIP5 models for 1979-2012. Correlations had first been computed in each of the ensemble members then averaged over the whole given ensemble. By averaging the

four correlation maps belonging to each of the four large ensemble simulations (Figure 3.1-3d-f), I obtained an overall picture of how models capture the observed Arctic atmosphere-sea ice interactions on interannual timescales. Similarly, I average the 31 correlation maps derived from each of the individual CMIP5 model historical+RCP8.5 runs (Figure 3.1-3g-i). I also show correlations between Arctic area averaged (north of 60°N) JJA *Z200* and total September total *SIA* index for the 31 CMIP5 multi-model and five single-model ensembles' individual members (Figure 3.1-3j).

The inverse relationship between September total *SIA* index and both JJA upper-level geopotential height and lower-to-mid-tropospheric temperature is seen in both observations and the CMIP5 multi-model or single-model ensemble mean simulations (Figure 3.1-3). However, observations reveal stronger interannual coupling between sea ice and both upper-level geopotential heights (r = -0.65 vs. r = -0.3) and lower-tropospheric temperatures (r = -0.75 vs. r = -0.5) than the models (Figure 3.1-3). The underestimated sea-ice-atmosphere correlations' magnitudes are especially profound in the CSIRO-LE and the CanESM-LE, which is in line with the lack of a correctly resembled summer mean sea ice state (Figure 3.1-2g) or melting spatial pattern (Figure 3.1-2e,g) in those models. Nonetheless, the SMILEs show improvements in capturing the observed interactions relative to the CMIP5 ensemble and the CESM-LE appears the best in resembling the observed correlation. Overall, both the perturbed initial condition and CMIP5 models capture the observed interannual coupling of Arctic summertime circulation and September sea-ice variability but with weaker magnitudes and with a somewhat different horizontal *Z200* and vertical height/temperature profiles, which is an important limitation common to all the models (Figure 3.1-3). Hence, this suggests that simulated sea-ice appears to be less sensitive to changes in the atmosphere than observed in the past 40 years in line with previous studies (Ding et al, 2017;2019; *Baxter et al. 2019*).

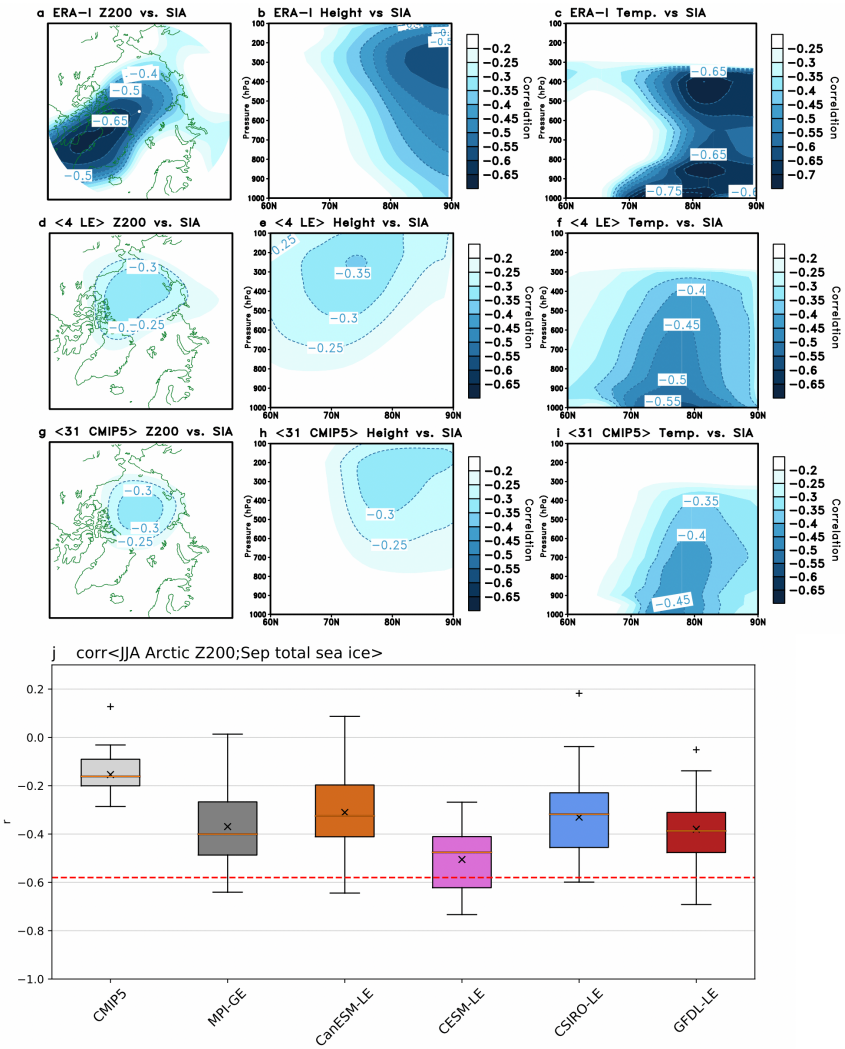

FIG. 3.1-3. Interannual coupling between sea-ice and overlying atmospheric circulation. Linear correlation of: (a) JJA *Z200*, (b) zonal mean geopotential height (*height*) and (c) temperature (*temp*) with September total sea ice area (*SIA*) index in ERA-I reanalysis for 1979-2012 (contoured values are significant at 95% confidence level). Correlation of (d) JJA *Z200*, (e) zonal mean geopotential height and (f) zonal mean temperature with September total *SIA* index for 1979-2012 averaged over four SMILE's historical+RCP8.5 runs (correlations are computed as the mean (denoted with < >) of the four correlation maps (excluding CSIRO-LE) each of which is constructed as first computing correlation in each of the members of a given single-model LE and then averaging over the whole given SMILE). Correlation of (g) JJA *Z200*, (h) zonal mean geopotential height and (i) zonal mean temperature with September total *SIA* index for 1979-2012 averaged (denoted with < >) over 31 CMIP5 models' historical+RCP8.5 runs (correlations are first computed in each of 31 models then the 31 correlation patterns are averaged to construct a 31-member multi-model ensemble). Contours on (d)-(i) do not represent significance as I do not account for the significance of the averaged correlation maps. (j) Correlation of Arctic area averaged (60-90°N; 0-359°E) JJA *Z200* and September total *SIA* index in each of the members of the five SMILE simulations: The boxes (h) indicate the interquartile interval (IQI), the whiskers extend up from the top of the box to the largest value less than or equal to 1.5 times the IQI and down from the bottom of the box to the smallest value that is larger than 1.5 times the IQI. Values outside this range are considered to be outliers and are indicated by crosses. The × shows the mean and the horizontal orange line the median (Kovacs et al. 2012). The red dashed line indicates the ERA-I correlation value (r = –0.58). All variables are linearly detrended before calculating correlations. *This Figure is adopted from Topál et al. (2020a).*

3.1.3 Low-frequency atmosphere-sea ice coupling from 1979 to 2012

Ding et al. (2019) showed evidence (using only the CESM-LE) that a similar physical mechanism dominates atmosphere-sea-ice interactions on low-frequency timescales as in interannual timescales. The *Z200*, zonal mean geopotential height (*Z*) and zonal mean temperature (*T*) fast-minus-slow composites (Section 2.5) reflect the coupling between *trends* in the atmospheric variables and sea-ice. Therefore, next I compare the composite trend patterns to the ones obtained previously (Section 3.1.2) with correlation analysis and use the similar features of the two to assume an alike physical mechanism over the two timescales.

The observed circulation trend pattern (Figure 3.1-4a-c) is reproduced in the mean of four SMILE simulations' historical fast-minus-slow composites (i.e., internal variability; Figure 3.1-4e-g) rather well, in contrast to the linear trend patterns derived from the ensemble mean (forced component) simulations, which show uniform height rise and warming in the Arctic without any regional anticyclone-driven features (Figure 3.1-4i-k). Note that the composite trend magnitudes (Figure 3.1-4e-g) are markedly weaker than the observed trend magnitudes (Figure 3.1-4a-c) suggesting that internal atmospheric variability may play a key role in the observed summer circulation changes, however models exhibit limitations in fully capturing the magnitude of the internal atmospheric process. Because the spatial patterns of changes in the atmospheric variables on the low-frequency timescales (Figure 3.1-4e-g) strongly resemble the ones we have seen in the atmosphere-sea ice correlation maps (Figure 3.1-3), the weaker composite magnitudes can be related to the tendency for models to underestimate atmosphere-sea ice correlations (Figure 3.1-3) relative to observations.

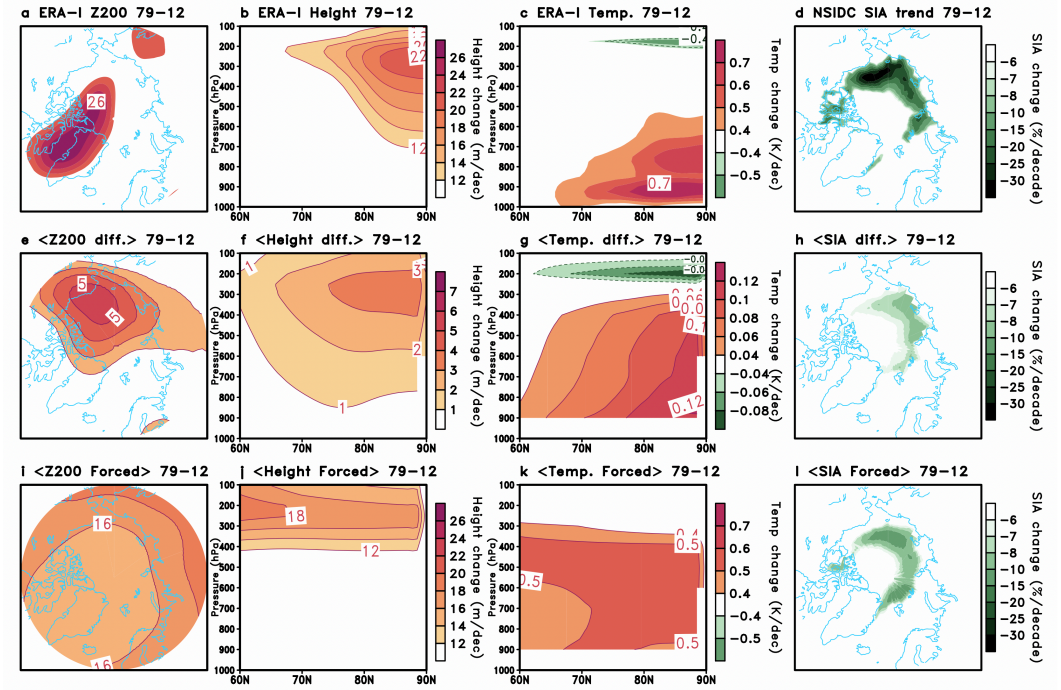

FIG. 3.1-4. Low-frequency coupling between September sea-ice variability and overlying atmospheric circulation in ERA-I and SMILEs. Observed (ERA-Interim Reanalysis/NSIDC) (a) *Z200*, (b) zonal mean geopotential height (*height*), (c) zonal mean temperature (*temp*) and (d) September sea ice area linear trends for 1979-2012. Also shown: (e) Z200, (f) zonal mean geopotential height, (g) zonal mean temperature and (h) September sea ice area fast-minus-slow composite trends and the ensemble mean (i) Z200, (j) zonal mean geopotential height, (k) zonal mean temperature and (l) September sea ice area trends averaged over the 4 SMILE historical+RCP8.5 experiments for 1979-2012 (excluding CSIRO-LE the mean of four Z200, height, temperature and sea ice either fast-minus-slow composite or ensemble mean (forced) trends are denoted with < >). Note, the colourbar differences between (e)-(g) the composite and (i)-(k) the forced or (a)-(c) observed trend magnitudes. *This Figure is adopted from Topál et al. (2020a)*

For further investigation let us compare the mean of four SMILE's fast-minus-slow composite of September *SIA* (Figure 3.1-4h) to the forced component (Figure 3.1-4l). Notice that the mean of the four SMILE simulations' *Z* or *T* composite trend magnitudes are three-to-four times smaller than the corresponding forced component magnitudes (Figure 3.1-5e-g vs. Figure 3.1-5i-k), however the difference between the internal and the forced sea-ice melting pattern magnitudes or spatial distributions is less pronounced. Hence, the prominent difference between internal and forced atmospheric trend magnitudes does not yield large differences between forced and internal sea-ice melting rates, which further emphasizes the necessity to search for associated atmospheric changes to

understand the underlying mechanism responsible for the melting. I present such evidence in 31 CMIP5 pre-industrial control simulations' composite patterns for 1979-2012 in Figure 3.1-5. The same patterns representing the low-frequency atmosphere-sea ice coupling are reproduced in the pseudo-ensemble of 31 CMIP5 pre-industrial runs without the presence of anthropogenic forcing (Figure 3.1-5).

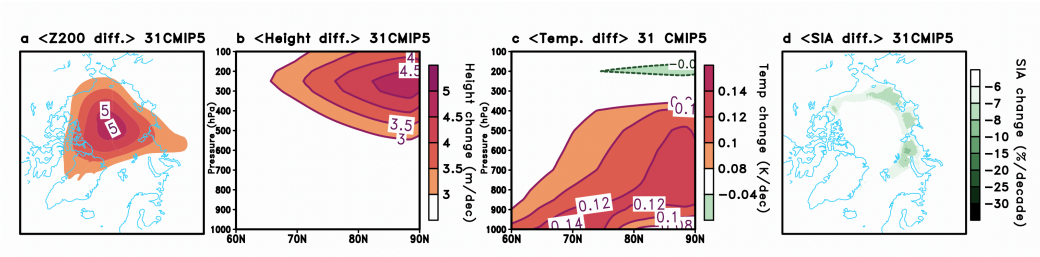

FIG. 3.1-5. Low-frequency coupling between September sea-ice variability and overlying atmospheric circulation in pre-industrial simulations from CMIP5. The mean (denoted with < >) of fast-minus-slow (a) *Z200*, (b) zonal mean geopotential height (*height*), (c) zonal mean temperature (*temp*) and (d) September sea ice area composites constructed using each 34-yr long periods of long pre-industrial control integration of 31 individual CMIP5 models aka. the pseudo-ensemble method (see Section 2.7). *This Figure is adopted from Topál et al. (2020a)*

With the *qualitative* analysis of historical and pre-industrial fast-minus-slow composites in the various model experiments robust evidence was shown that the regional barotropic height increase over the Arctic in summer – favouring adiabatic warming and moistening of the lower troposphere – also dominates summer sea ice variability on low-frequency timescales in both the real- and pseudo-ensemble simulations (Figures 3.1-4 and 3.1-5). Our results further support previous findings (Wernli and Papritz 2018) that this internal atmospheric process is a contributor to sea-ice melt across different model environments (Ding et al. 2019). I also draw attention to the fact that current climate models possibly underestimate the strength of atmosphere-sea-ice coupling relative to the observed one in ERA-I on both year-to-year and low-frequency timescales. The weaker year-to-year coupling of sea-ice with the atmosphere (Figures 3.1-3 and 3.1-4) may indicate a weaker coupling mechanism in the trend-related composites as well. In ERA-I the maximum JJA *Z200* (*SAT*) change over 1979-2012 in the Arctic is 26 m decade^{-1} (0.6 °C decade^{-1}), while

models show only 4-7 m decade^{-1} (0.12°C decade^{-1}) in the fast-minus-slow composites. The relative role of the internal component, therefore, needs further estimation (Roach and Blanchard-Wrigglesworth 2022), however these results indicate that models fail to replicate the full strength of the observed atmosphere-sea ice connection (*Topál et al. 2020a*).

3.1.4 Low-frequency atmosphere-sea ice coupling from 2020 to 2050

How this atmospheric process, identified in observations and historical/pre-industrial model simulations, will behave in the future has so far been unaddressed in the literature. Therefore, I now evaluate the fast-minus-slow composites in all the available future scenario runs of the five large ensembles for 2020-2050.

In general, the mean of the fast-minus-slow composites corresponding to the four models' (excluding the CSIRO-LE) RCP8.5 scenarios (Figure 3.1-6a-c), unlike the forced model component linear trends (Figure 3.1-6e-g), are reminiscent of the atmospheric structure that dominates sea-ice variability on interannual to interdecadal timescales in observations, historical and pre-industrial model simulations. Similar to the historical period, all individual models show high pressure in the Arctic upper troposphere along with surface warming concomitant to sea-ice loss (Figure 3.1-6). The composite trend magnitudes are comparable to the small historical and pre-industrial composite magnitudes (relative to the observed trends). The small magnitudes seen in the future fast-minus-slow composites (Figure 3.1-6) can also be linked with the underestimated atmosphere-sea ice interannual coupling (Figure 3) rooted in the models' physics. Examining the mean of 4 SMILE's September *SIA* composites we can also see that future sea-ice melt occurs over the Arctic Ocean, north of Greenland and Canada in the internal component reminiscent of the ensemble mean *SIA* trends (forced component) (Figure 63.1-d,h). Despite minor differences in the magnitudes and spatial patterns of sea-ice melt between the forced and

internal sea-ice trend components (Figure 3.1-6d vs. h) the atmospheric circulation patterns differ considerably (Figure 3.1-6a-c vs. e-g). Also, while models show discernibly more sea-ice melt during 2020-2050 compared to 1979-2012 (Figure 3.1-2), the differences in the magnitude of sea-ice associated atmospheric changes are not so pronounced between the two periods (Figures 3.1-4 and 3.1-6). This raises concerns about the accuracy of the modelled sea-ice sensitivity to atmospheric circulation driven changes compared with its response to anthropogenic forcing.

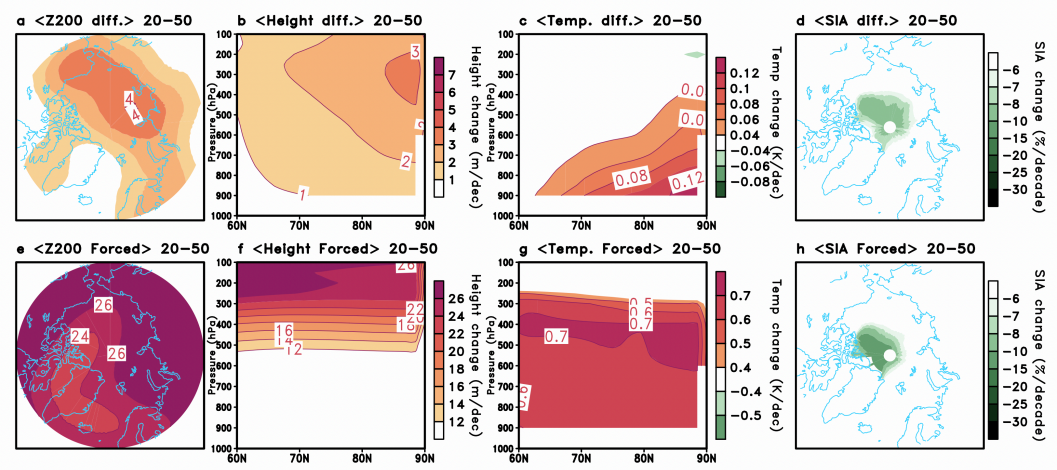

FIG. 3.1-6. Future (a) *Z200*, (b) zonal mean geopotential height (*height*), (c) zonal mean temperature (*temp*) and (d) September sea ice area (*SIA*) fast-minus-slow composite trends and the ensemble mean (e) *Z200*, (f) zonal mean geopotential height, (g) zonal mean temperature and (h) September sea ice area trends averaged over four large ensembles' RCP8.5 experiments for 2020-2050 (excluding CSIRO-LE the mean of each of the four *Z200*, *height*, *temp* and *SIA* either fast-minus-slow composite or ensemble mean (forced) trends are denoted with < >). Note, the colourbar differences between (a)-(d) the composite and (e)-(h) the forced trend magnitudes. *This Figure is adopted from Topál et al. (2020a).*

The presented analyses, however, were solely focused on reaching a *qualitative* understanding of internal drivers of sea-ice loss across different model environments, thus, the relative contribution of internal variability remains an open question (and to be addressed further on in **Sections 3.2** and **3.3**) in light of limited model performance. Because of the similarities between the atmosphere-sea-ice interactions seen on year-to-year and low-frequency timescales, it is reasonable to assume that the underestimated year-to-year coupling has an impact on the low-frequency focused composite calculations as

well, likely contributing to the consistently weak magnitudes captured in the fast-minus-slow composites. Model limitations in simulating wind-driven mechanisms (Hofer et al. 2019) or moisture and cloud variability (Huang et al, 2019) could be sources of biases in replicating the observed atmosphere-sea ice coupling. I also note that in models the local Arctic atmosphere-sea ice coupling still exists without prominent remote tropical forcing (see further details in *Topál et al. 2020a*) although the magnitude of the coupling is weaker. This indicates that the generation of the local coupling could also be due to local feedback. Further research toward identifying the relative role of the local and remote forcing mechanisms in the observed atmosphere-sea-ice interactions is needed.

Although Olonsheck et al. (2019) also emphasized that atmospheric processes dominate Arctic sea-ice variability, I cannot rule out the role of the heat content change in the ocean (Steele et al, 2008;2010; Zhang et al, 2013). Limitations of our methodology can also leave undetected variability belonging to either atmospheric or oceanic processes, since the fast-minus-slow method relies on a subjective choice of ensemble members belonging to the fast and slow groups. I am also aware that there is no guarantee that the strength of the teleconnections remains constant in the future under high emission scenarios (Herein et al, 2016;2017; Tél et al, 2019), therefore non-linear, higher order processes may also play a significant role (*Haszpra et al, 2020a*).

In what follows, I will further guide the reader to reach a better understanding of the relative importance of internal atmospheric variability in regulating Arctic cryosphere changes with a special focus on the GrIS. Others (Ding et al. 2022; Baxter and Ding, 2022; Li et al. 2022) have continued the line of thinking presented above ***(Section 3.1****) regarding sea-ice and Arctic Ocean changes associated with upper-level wind anomalies in the Arctic. I led the evaluation of a new, comprehensive modelling framework (the so-called nudging simulations) in terms of the mass balance of the GrIS.*

3.2 Discrepancies between observations and climate models of large-scale wind-driven Greenland melt impact sea-level rise projections

This Section is based on *Topál et al. (2022)* addressing A_2 and A_3.

Given the considerations in **Section 1.2**, the separation of the physical mechanisms behind GrIS surface warming into adiabatic (causing *vertically non-uniform* warming) and diabatic (causing *vertically-uniform* warming) processes offers the potential for not only showcasing potentially divergent physical mechanisms behind observed and modelled GrIS warming, but also for quantifying the contribution of large-scale winds to accelerating sea-level rise. This is only possible by taking a conceptually different, dynamical approach contrary to previous studies that have mainly applied diagnostic and statistical approaches to observations and model simulations forced by constant or varying greenhouse gases over the past 40 to 150 years when examining the effects of atmospheric circulation on GrIS melt (Delhasse et al. 2018; Bevis et al. 2019; Hanna et al. 2013; Sherman et al. 2020). In this Section I present results based on purpose-designed "wind nudging" model experiments, which helps to quantify the role of large-scale winds – dominantly representing internal variability, see discussion on caveats below – in enhancing the rate of sea-level rise by accelerating Greenland summer surface melt.

To distinguish between the two dominant mechanisms of observed GrIS summer warming as manifested in the circulation-driven adiabatic component and the radiative forcing-induced diabatic warming, a two-step approach is taken in a dynamical modelling framewor. First, the fully-coupled Community Earth System Model 1.2 (nominal 1 degree resolution) and second, the Community Ice Sheet Model (CISM) Glimmer with a higher spatial resolution (~5 km) was used to conduct atmospheric wind-nudging experiments (from ERA5) without interaction from time-varying anthropogenic forcing. To do so, external forcing (greenhouse gases, aerosols, solar) is set to constant values at the level of

the year 2000 (367 ppm), which roughly represent the climatological mean values over 1980-2018 (see further details in **Sections 2.8**).

Since the same model is used to conduct the nudging runs as the SMILE version of the CESM1 (CESM-LE), I can also compare our 10-member wind-nudging experiment to the CESM-LE. While the winds from ERA5 may already contain fingerprints of anthropogenic forcing – through proportional relationship between temperature and geopotential heights –, this comparison reveals the importance of observed winds in causing the recent acceleration of GrIS melt and corresponding increase in the rate of barystatic sea-level rise relative to simulated GrIS changes in the ensemble-mean (forced response) and the ensemble spread (internal variability) in the CESM-LE. Further, forced wind changes might be affected by model structural biases, which complicates the quantification of the internal/forced observed wind changes. Therefore, I compare our nudging experiment to simulations of 31 CMIP5 models, which is expected to help in clarifying whether any structural bias in the CESM-LE may be common across other models. In addition, I extend the analysis beyond the observational era by utilizing two recently available paleoclimatic proxy data-assimilated reconstructions (paleo-reanalyses) in addition to independent Greenland ice core and oceanic coral proxy records spanning the past 400 years. These analyses offer the opportunity to derive further insights into the persistence and robustness of the observed wind-driven GrIS warming mechanisms during periods with much less influence from anthropogenic emissions. By doing so the aim was to advance the current understanding of large-scale atmospheric forcing driven GrIS surface changes since the early 17th century and contribute to contextualizing uncertainties of current model projections of sea-level rise.

3.2.1 Observed and modelled summer GrIS melt and overlying circulation changes

I first describe past changes in GrIS surface conditions using mass balance estimates from the Ice Sheet Mass Balance Inter-comparison Exercise (IMBIE; The IMBIE Team 2020). In addition, I use surface mass balance (SMB, Eq. 2 in **Section 2.3**) and *SAT* simulations from a widely used and GrIS optimized (Fettweis et al. 2017; Fettweis et al. 2011; Delhasse et al. 2020) regional climate model, *Modéle Atmosphérique Régional*, (MAR, **Section 2.3**), which is 6 hourly forced by the ERA5 (Delhasse et al. 2020; Hersbach et al. 2020) reanalysis at its boundaries. I also characterize synchronous changes in the overlying atmospheric circulation in ERA5 since 1980 alongside increasing GrIS mass loss (Hanna et al. 2021; The IMBIE Team 2020).

Both the satellite-observed rate of annual total mass change (The IMBIE Team 2020) and MAR climate model simulations of JJA *SAT* and *SMB* anomalies over Greenland show substantial interannual variability during the 1980-2018 period (Figure 3.2-1a). Similar year-to-year variability is observed with sea surface temperatures (*SST*) over Baffin Bay (60º-80ºN; 50º-70ºW) ($r_{SST;SAT}$ = 0.78 (0.67); $r_{SST;SMB}$ = 0.85 (0.77) for raw (linearly detrended) data). This indicates a possible shared driving mechanism behind Greenland and proximate ocean surface changes beyond anthropogenic forcing (Figure 3.2-1b). Associated changes in atmospheric circulation over the GrIS are revealed by re-creating an often used metric – the Greenland Blocking Index (*GBI*; Hanna et al. 2021; Hanna et al. 2018; Hanna et al. 2016) – and developing the Greenland Streamfunction Index (*GSI*, Figure 3.2-1c). The *GSI* is calculated from the ERA5 500hPa streamfunction (Ψ500) by spatially averaging the area-weighted Ψ500 anomaly field over the GrIS (20-80ºW; 60-80ºN) in JJA. The *GSI* is strongly correlated (~0.88) with the *GBI* in summer, but because it reflects the rotational features of large-scale circulation that control the adiabatic

warming process in the lower troposphere, it better represents the physical mechanisms discussed herein (**Section 2.9**).

The ERA5 *GSI* explains significant part of the interannual variability in MAR simulated summer *SAT*/*SMB* and Baffin Bay SSTs over 1980-2018, regardless of whether the underlying trend is removed or maintained, suggesting that this relationship results primarily from internal variability ($r^2_{GSI;SAT}$ = 0.56 (0.46); $r^2_{GSI;SMB}$ = 0.69 (0.61); $r^2_{GSI;SST}$ = 0.56 (0.53) for raw (linearly detrended) data). The accompanying spatial trends in the MAR simulated GrIS *SAT* (0.446 K decade^{-1}) and circulation – as described by ERA5 500hPa geopotential height (Z500; 12-15 m decade^{-1}) and horizontal winds (*GSI*; 0.844 10^6 m^2 s^{-1} decade^{-1}) – show synchronous changes over 1980-2018. Such trends suggest that the aforementioned high-pressure-driven adiabatic warming process has likely acted in concert with anthropogenic forcing in shaping GrIS climate variability over the past four decades (Figure 3.2-1d).

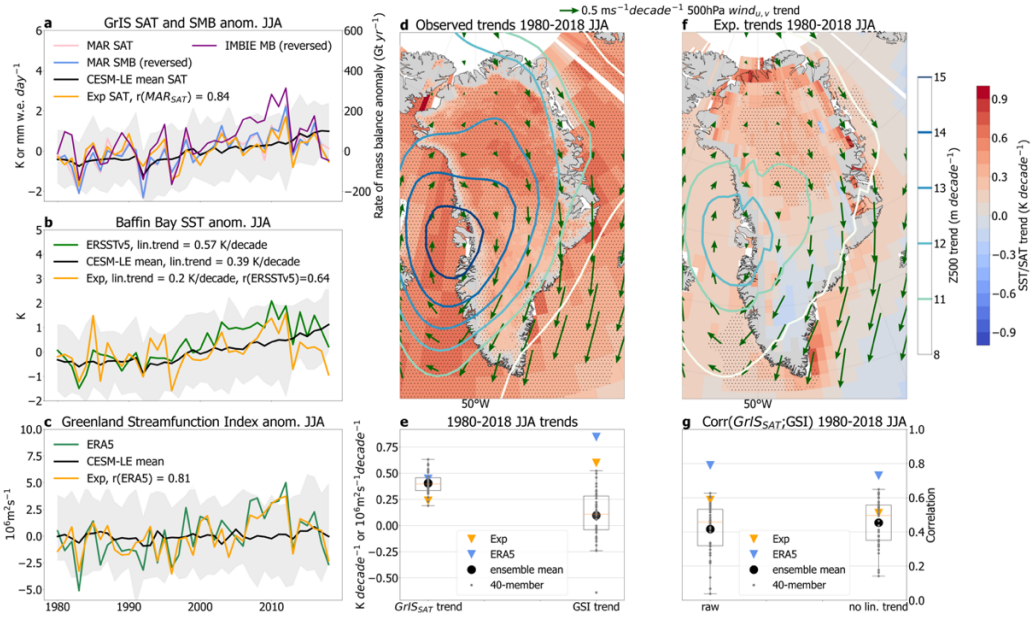

FIG. 3.2-1. Observed and simulated circulation-driven GrIS summer surface conditions over 1980-2018. (a) GrIS spatially-averaged time-series of anomalies in MAR surface air temperature (*SAT*, pink) and surface mass balance (*SMB*, blue), the ensemble mean *SAT* from CESM1 large ensemble (CESM-LE, black) and the *SAT* from the wind-nudging experiment (Exp) in CESM1 (orange) in summer (June-July-August, JJA) as well as the observed annual rate of total GrIS mass change (IMBIE) (purple). The grey shading in (a) represents the range of all members' *SAT* anomalies from the CESM-LE. In (b) ERSSTv5 sea surface temperatures averaged over the Baffin Bay (60º-80ºN; 50º-70ºW) (green) is compared with the ones calculated using the CESM-LE mean (with black), the spread in CESM-LE (grey shading) and the wind-nudging experiment (Exp, orange) for JJA. (c) is same as (b), but for the 500hPa Greenland streamfunction index (*GSI*, **Section 2.9**). In (d), spatial maps of the linear trend in (MAR) *SAT* (shading), ERSSTv5 *SST*s (shading), 500hPa geopotential height (*Z500*, contours, unit: m/decade) and 500hPa horizontal winds (arrows) in ERA5 and (f) in the wind-nudging experiment (Exp) in JJA for 1980-2018. Panel (e) shows the linear trends in GrIS spatially-averaged *SAT* (first box-and-whiskers plot), the *GSI* (second box-and-whiskers plot) and (g) the raw (detrended) correlations between GrIS *SAT* and *GSI* in the first (second) box-and-whiskers plots as shown with markers corresponding to the legend. The whiskers extend to 1.5 times the interquartile-range (IQR) and the median is indicated with an orange horizontal line, outliers (that extend 1.5 IQR) with crosses. Hatching in (d) and (f) indicate areas with statistically significant linear trends based on the Mann-Kendall test ($p<0.05$).

Contrary to the observed synchrony between GrIS surface and overlying atmospheric circulation changes, 31 CMIP5 climate models and the 40-member CESM-LE also indicate less of an influence from wind-changes on GrIS warming (Figure 3.2-2). It is also the case in version 2 of CESM (Noël et al. 2020) and more generally in the CMIP6 models (Hofer et al. 2020; Delhasse et al. 2018). These findings suggest the possibility that

climate models may misrepresent driving mechanisms; hence, to further interpret the potential consequences, I describe the results based on the aforementioned wind-nudging model experiments.

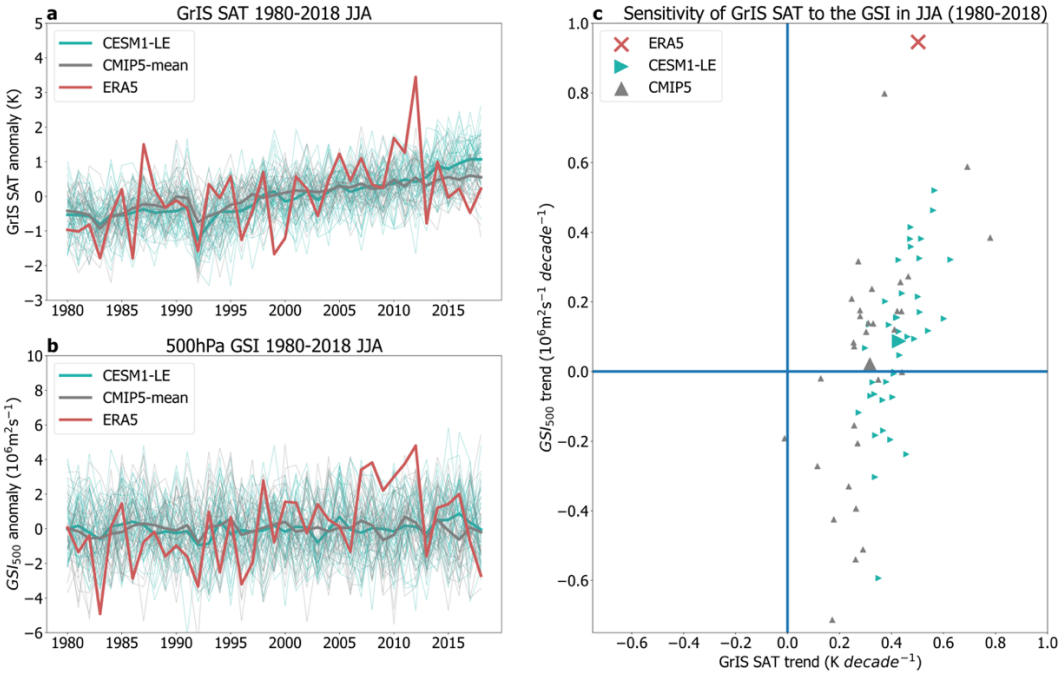

FIG. 3.2-2. Observed and simulated sensitivity of the Greenland Ice Sheet (GrIS) to large-scale atmospheric circulation. (a) Greenland ice sheet (GrIS) surface air temperatures (*SAT*) in ERA5, the 40 member CESM-LE (ensemble mean with thick light blue line) and in 31 CMIP5 models (multi-model ensemble mean with thick grey line) between 1980-2018 in June-July-August. (JJA). (b) the same for the Greenland Streamfunction Index (*GSI*) calculated from 500hPa horizontal winds, and (c) scatter plot of the trends in the GSI and the GrIS *SAT* in each member of the CESM-LE (seagreen triangles; ensemble mean with larger marker), each CMIP5 model (grey markers; ensemble mean with larger marker) and in ERA5 (red 'x'). Note how each CMIP5 and CESM-LE members simulate GrIS warming without concomitant changes in their simulated *GSI*.

3.2.2 Separating diabatic vs. adiabatic mechanisms driving GrIS melt

Observationally constraining winds in the CESM1 (i.e., the nudging) results in the model closely resembling the interannual variability in ERA5 *GSI* (Figure 3.2-1c, $r = 0.81$), in MAR GrIS *SAT* (Figure 3.2-1a, $r = 0.84$) and in ERSSTv5 Baffin Bay *SST*s (Fig. 1b, $r = 0.64$). As for the summertime spatial trend patterns, on average, 53% of observed *SAT*, 74% of the Z500 and 35% of the Baffin Bay *SST* changes between 1980 and 2018 are captured in the nudging experiment (Figure 3.2-1d,f). A further comparison between the

nudging-run derived GrIS surface conditions and those simulated by each of the CESM-LE members reinforces the differences between the simulated and observed sensitivity of the ice sheet to wind-changes seen in other CMIP models (Hofer et al. 2020; Delhasse et al. 2018; Noël et al. 2020) (Figure 3.2-2). I also highlight the contrast between the summer GrIS *SAT*/*GSI* trends over 1980-2018 in the observations and simulated in individual members comprising the CESM-LE, which underestimate the ERA5 *GSI* trend while encompassing the observed *SAT* trend during the 1980-2018 period (Figure 3.2-1e). Furthermore, the correlations between *GSI* and GrIS spatial averaged *SAT* are weaker in each individual CESM-LE member than in ERA5 ($r \sim 0.75$), and only three of these members exhibit equal or greater correlations compared to the nudging experiment ($r \sim 0.6$) (Figure 3.2-1g).

To account for observed wind changes that may stem from anthropogenic forcing, I also examine wind-changes in the CESM-LE mean and in the multi-model mean of 31 CMIP5 models. Although the CESM-LE (CMIP5) mean GrIS SAT trend is ~90% (~60%) of its ERA5 counterpart, the equivalent value for the *GSI* is only ~10% (~2%). Compared to the significant wind changes in ERA5, the year-to-year *GSI* series (Figures 3.2-1c and 3.2-2b) show only subtle changes over the 1980-2018 period in both CESM-LE and CMIP5 ensemble means. These findings are similar to both the weak trend in 500hPa horizontal winds in the CESM-LE mean (Figure 3.2-3a) and the uniform geopotential height response simulated by other single-model large ensembles (*Topál et al. 2020a*). While <10% of observed wind changes may be affected by anthropogenic forcing, a note of caution is warranted as models may also suffer from structural biases that can obstruct a realistic wind response to external forcing, and this shortcoming may limit the certainty of calculations that are currently available.

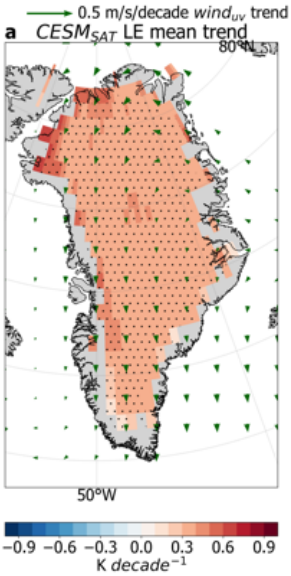

FIG. 3.2.-3. The forced response of winds and surface temperature over the GrIS in CESM-LE. Spatial pattern of the linear trends in the 40-member CESM large ensemble mean surface air temperature (*SAT*) and 500hPa horizontal winds (arrows; $wind_{uv}$).

To further interpret the implications of the lack of circulation changes in models for GrIS melt-driven processes, next, I analyze *SMB* changes, which are directly linked to sea-level rise. First, I separately assess the surface energy balance (*SEB*; Eq. 1 in **Section 2.1**) and total precipitation in the nudging simulation, which are the two key *SMB* components (Lenaerts et al. 2019) (Eq. 2 in **Section 2.3**). Similar to what we have seen for the GrIS *SAT*, imposing observed winds in our model experiment is sufficient to simulate a close match with both the summer and annual *SEB* interannual variabilities (Figure 3.2-4a-b) seen in the ERA5 (1980-2018) and the satellite product (CERES-EBAF (Kato et al. 2018), 2001-2020; **Section 2.1**). As for interdecadal time scales, the linear trends in the SEB also indicate an overall adequate simulation of satellite-observed changes in the nudging experiment in JJA (Supplementary Figure 1a-b) and annual means (Supplementary Figure 1d-e). These results suggest a decisive role for atmospheric circulation in controlling GrIS climate variability from an energy balance perspective. However, in line with the above-demonstrated limitations of the CESM-LE in capturing the circulation-related adiabatic component of GrIS melt, all members of the CESM-LE show relatively small year-to-year

coupling between *SEB* and the *GSI* compared with ERA5 and the nudging simulation (Supplementary Figure 2b) and show *SEB* changes with opposite sign compared with the EBAF over 2001-2020 (Supplementary Figure 2c,f,g). As for the total precipitation averaged over the GrIS, the nudging experiment performs reasonably well in replicating ERA5 summer and annual mean precipitation (Figure 3.2-4c,d). Although the nudging experiment seems to overestimate precipitation variability over the GrIS, especially before 2000 (~2.8 (~1.6) times greater standard deviation between 1980-2000 (2000-2018)), I conclude that precipitation is highly sensitive to imposed winds in the nudging run and, therefore, in reality.

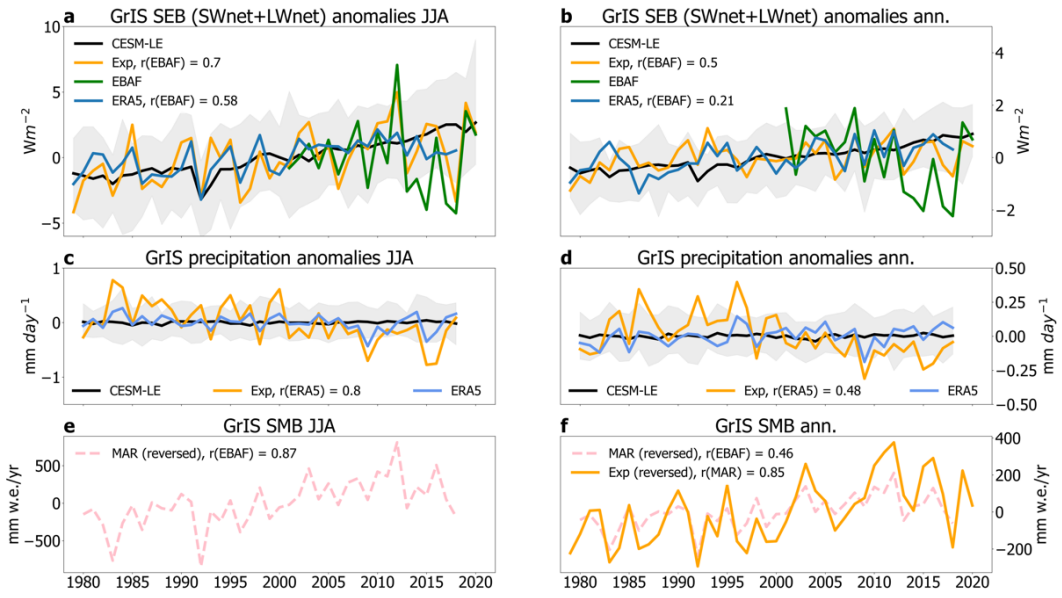

FIG. 3.2-4. The critical role of circulation in determining observed GrIS surface mass/energy balance over 1980-2018 as simulated by the nudging experiment. Comparisons between the Greenland spatially-averaged surface energy balance (*SEB*) anomaly time series in ERA5, EBAF satellite product (**Section 2.1**), the nudging experiment and the CESM-LE (grey shading and black line for the ensemble mean) for (a) JJA and (b) for annual means. Comparison between ERA5, the nudging experiment and the CESM-LE (grey shading and black line for the ensemble mean) GrIS spatially-averaged precipitation for (c) JJA and (d) the annual means. Panel (e) shows the MAR-simulated GrIS surface mass balance (*SMB*) anomalies for JJA along with (f) showing the comparison of annual *SMB* between MAR and the nudging experiment involving CISM-Glimmer. In the legends, 'r()' indicates the correlation coefficients between the corresponding variable and the one in the bracket.

To shed light on the contribution of wind-driven circulation directly to *SMB* variability, I analyze nudging experiments with the Glimmer-CISM (**Section 2.8.2**). The resulting Glimmer-CISM annual mean GrIS *SMB* exhibit similar climatology to the ERA5-forced MAR simulation, albeit with overestimating the ablation zone melt during the 1980-2018 period (Supplementary Figure 3). Despite the climatological bias, the nudging experiment qualitatively reproduces the observed features of *SMB* variability of the past four decades, as shown by the comparison between the spatially-averaged *SMB* anomaly time-series from our Glimmer-CISM experiment and the ERA5-forced MAR simulation (Figure 3.2-4f; r = 0.85; Supplementary Figure 4). Note that I have analysed a similar set of nudging-runs within the CESM2, which has an active dynamic ice-sheet model. The conclusions on the role of large-scale in driving GrIS *SMB* variability are valid even with a more complex ice-sheet model (not shown).

3.2.3 Wind-driven GrIS mass loss and sea-level rise acceleration

We have seen that, alongside anthropogenically-forced diabatic warming, atmospheric circulation changes are an important influence on the energy budget, precipitation and hence surface mass balance of the ice sheet. Besides the total cumulative ice loss from the GrIS, that has led to 10.8 ± 0.9 mm increase in global mean sea-levels over the past three decades (The IMBIE Team 2020), an additional key aspect is the observed acceleration in the rate of GrIS mass loss (–132.8 Gt yr^{-1} $decade^{-1}$) over 1990-2012 that was a dominant contributor to enhanced sea-level rise (Ablain et al. 2019; Chen et al. 2017) (1.2±0.7 mm yr^{-1} $decade^{-1}$ over 1993-2017). During 1990-2012, both the ERA5 and the nudging-derived GSI show concomitant increase, followed by a levelling-off until 2018 (Figure 3.2-1c), which corresponds with the lack of tropical forcing and a generally positive North Atlantic Oscillation phase (and less Greenland blocking) linked to colder conditions over Greenland (Hanna et al. 2021; Baxter et al. 2019). Quantifying the

contribution of wind-driven circulation to increased GrIS melt and resulting sea-level rise over 1990-2012 is crucial to better contextualize not only the misrepresentation of the adiabatic/diabatic driving mechanisms in the CESM-LE, but also identify the future potential of atmospheric circulation to further amplify as well as to counteract anthropogenically-forced GrIS changes.

Our model experiment suggests that – based on the ratio of observed and the nudging-run derived spatial-averaged SAT trends – atmospheric circulation alone explains 56% (55%) of the observed GrIS *SAT* (Baffin Bay SST) rise during 1990-2012 (Figure 3.2-5a-b). Areas located along the west, northwest, and north coasts of Greenland and in the north Labrador Sea show the largest contribution from atmospheric circulation towards explaining the observed *SAT* trends. These patterns are in line with the spatial structure of the high-pressure anomaly above the ice sheet that favours anomalous moisture fluxes to the northwest of the ice sheet (Noël et al. 2019) and subsidence over the west and southwest regions (Figure 3.2-5b; Figure 3.2-1d,f).

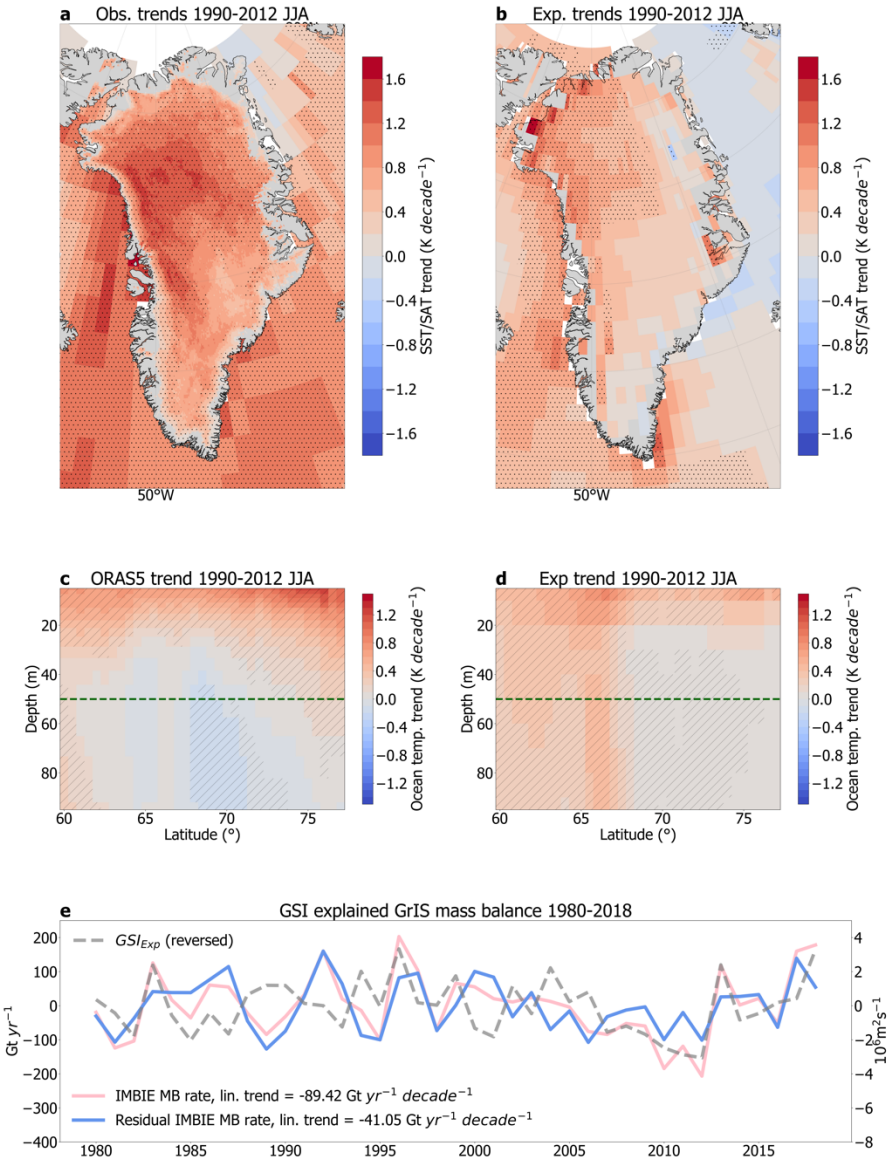

FIG. 3.2-5. The wind-driven acceleration of Greenland ice loss and Baffin Bay upper-ocean warming between 1990 and 2012. Linear trends in summer (June-July-August, JJA) (a) ERA5 surface air temperature (*SAT*) and ERSSTv5 sea surface temperature (*SST*), (b) the nudging experiment-derived *SAT*/*SST*, (c) ORAS5 upper-ocean (0 – 100 m) temperature (zonal mean over 50ºW-70ºW longitudinal band) and (d) nudging experiment derived upper-ocean (0 – 100 m) temperature (zonal mean over 50ºW-70ºW longitudinal band) between 1990-2012. The green dashed lines in (c)-(d) indicate the section used to average ocean temperatures shown in Figure 3.2-6b. Hatching indicates statistically significant ($p<0.05$) trends. Panel (e) shows the linearly detrended annual mean rate of Greenland mass balance anomaly from The IMBIE Team (2020) (pink) and the linearly detrended summer Greenland streamfunction index derived from the nudging experiment (GSI_{Exp}, grey). The residual rate of Greenland mass balance anomaly (blue) based on having linearly regressed out the GSI_{Exp} (grey) from the annual mean rate of Greenland mass balance anomaly (pink) is also shown. The linear trend values in the legend refer to the 1990-2012 period. Note that these values differ from those mentioned in the text, because these are obtained after having removed the 1980-2018 linear trend from the mass balance time series as a first order approximation of anthropogenic forcing.

About half of the observed total Greenland ice loss is due to reduced *SMB*-driven meltwater runoff, which we have addressed in the nudging simulations. However, the other half is attributable to glacier dynamical imbalance (The IMBIE Team 2020). Since the CISM-Glimmer model used in this study is developed to simulate *SMB* in relatively slow-flowing regions of the GrIS, rather than fast outlet glacier changes, I statistically assess how the melting rates of 260 Greenland outlet glaciers/ice caps (Mouginot et al. 2019) may be regulated by overlying wind changes. To do so, I utilize the nudging run-derived *GSI* that explains significant interannual variability over 1980-2018 of 94 glaciers flanking the southwest (SW), central west (CW) and northwest (NW) of the island (Figure 3.2-6a; r_{average} = 0.43, with up to r_{maximum} = 0.6). The underlying trend in the glaciers' mass balance time series, which is a combination of the anthropogenic forcing-induced diabatic warming and the wind-driven adiabatic warming, influences the correlations and only 41 glaciers, located mostly in the SW, show significant correlations after removing the linear trends from the data (r_{average} = 0.39; r_{maximum} = 0.48). Similar spatial differences to overlying atmospheric circulation was documented in geochemical parameters over the past millennium across the GrIS (Hatvani et al. 2022). Based on the nudging simulations, I speculate that winds may directly influence Greenland glacier melt in a similar manner as *SAT* and *SMB* in addition to indirectly, through ocean warming.

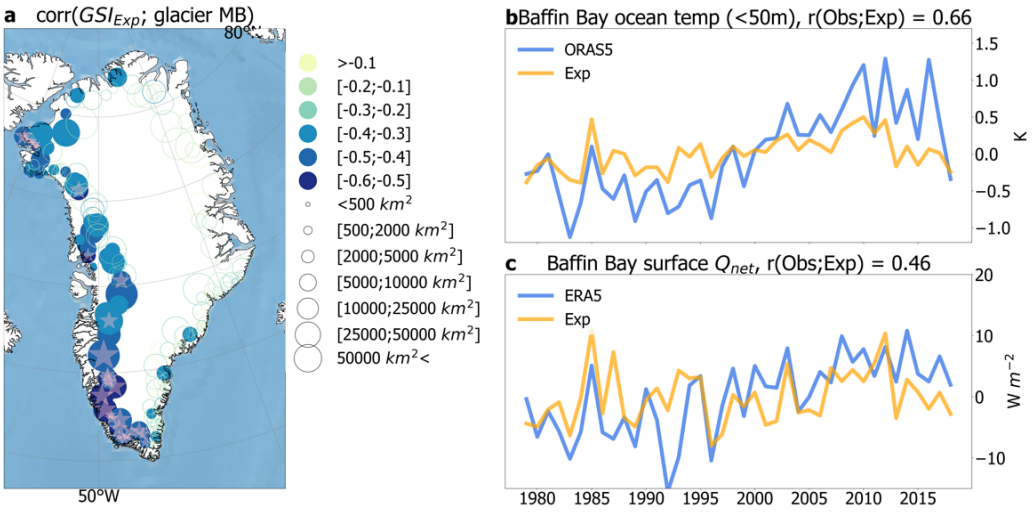

FIG 3.2-6. Effect of winds on Greenland glaciers and upper-ocean heat content changes. In (a) the correlations between the summer *GSI* and the annual mean rate of mass balance of 260 glaciers from Mouginot et al. (2019) during 1980-2018 are shown. Filled circles indicate statistically-significant correlations ($p<0.05$) and pink stars denote those glaciers that show significant correlations even after detrended. The size of the markers are proportional to the area of the given glacier (see legend). Also shown: (b) JJA upper-ocean (0 – 50 m) temperature anomalies and (c) surface net heat flux anonmalies (reltive to the 1980-2018 period) from the atmopshere into the ocean spatially averaged over 50-70°W 60-77°N between 1990-2012 in ORAS5/ERA5 reanalysis (blue) and in the nudging experiment (Exp, gold).

In an effort to account for Baffin Bay upper-ocean (0-50 m) warming that influences air-sea-ice interactions, I utilize the ocean component of the nudging experiment to compare upper-ocean temperature trends in the wind-imposed simulation with the ORAS5 ocean-reanalysis during 1990-2012 (Figure 3.2-5c,d). I find significant upper-ocean warming in the wind-nudging simulations over the north Labrador Sea – Baffin Bay area (50-70°W; 50-78°N), resembling the vertical cross-section of warming along the west coast of Greenland in the reanalysis (Figure 3.2-5c-d). A comparison of the spatially and vertically averaged upper-ocean temperature time series (Figure 3.2-6b) in the nudging experiment with its reanalysis counterpart reveals that about third of the trend can be simulated in our model via the sole imposition of Arctic winds. This warming seems to be closely related to the surface net fluxes from the atmosphere into the upper ocean (Q_{net}; Figure 3.2-6c) with a prominent lead-lag relationship developing in early summer Q_{net} that

leads ocean temperatures until September in both the reanalysis and the nudging experiment (Figure 3.2-7). These findings suggest that atmospheric circulation plays an important role in governing Baffin Bay upper-ocean temperatures. Similar findings have recently been shown for other parts of the Arctic Ocean (Li et al. 2022).

Note that those ocean waters that primarily force Greenland termini retreat tend to be situated at the grounding lines of the glaciers (Wood et al. 2021) whose depths extend beyond the scope of this study. However, climate models' inability to simulate observed wind-driven circulation over the GrIS likely translates into uncertainties involving the simulation of wind-driven Atlantic Water intrusion into the Baffin Bay, which is of importance, for example, to the destabilization of GrIS outlet glaciers (Wood et al. 2021; Rignot et al. 2012; Holland et al. 2008) and thus warrants future analysis.

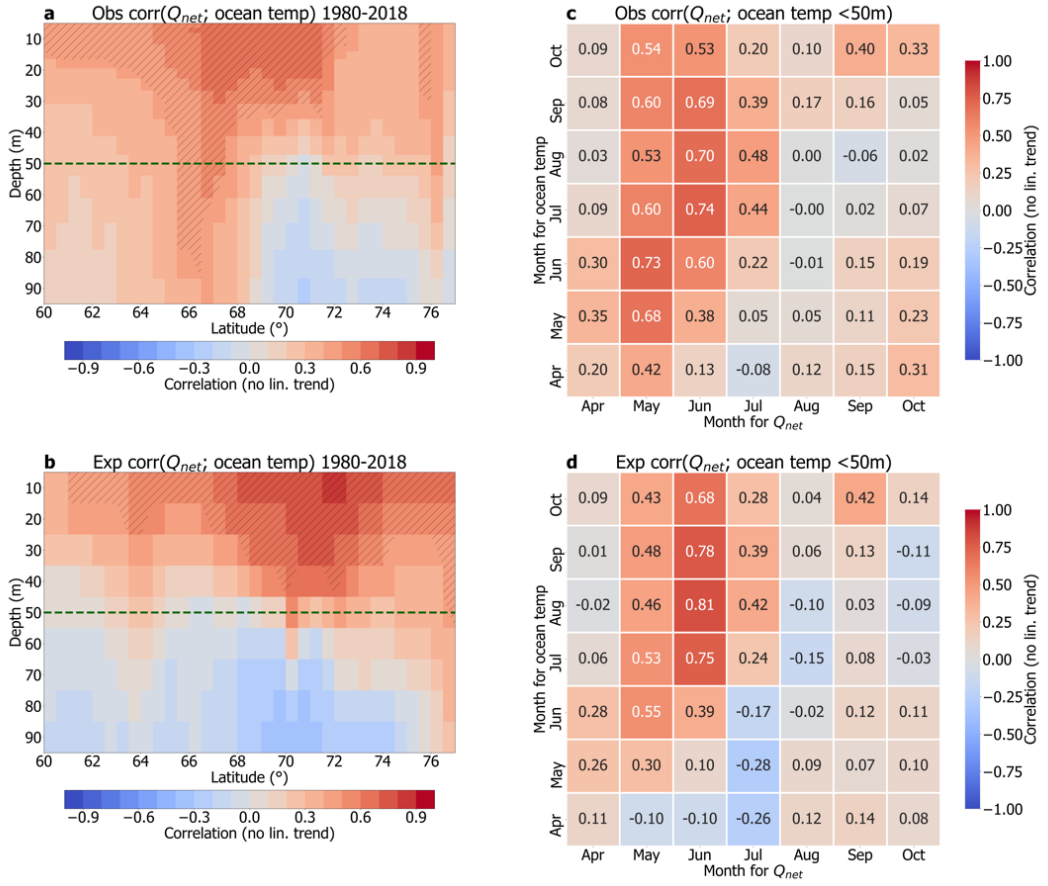

FIG. 3.2-7. Lead-lag relationships between wind-forcing and upper-ocean temperatures. Correlations between the net surface heat flux from the atmopshere into the ocean (Q_{net}) averaged over the Baffin Bay (50-70ºW; 60-77ºN) and upper ocean temperature (zonal mean over 50ºW-70ºW longitudinal band) in (a) the ORAS5 reanalysis and (b) in the nudging experiment over 1980-2018. Hatcing indicates statistically significant trends ($p<0.05$). Also shown: lead-lag correlation between the net surface heat flux from the atmopshere into the ocean (Q_{net}) averaged over the Baffin Bay (50-70ºW; 60-77ºN) and the upper 50m averaged ocean temperature (zonal mean over 50ºW-70ºW longitudinal band) in (c) ERA5/ORAS5 and (d) in the nudging experiment from April to October between 1980-2018. The linear trends are removed before correlations are calculated.

Lastly, motivated by the *dynamical* understanding of driving mechanisms based on the wind-nudging simulations, I *statistically* estimate the total Greenland ice loss acceleration driven by the changes in the *GSI* and its contribution to the increasing rate of sea-level rise. The calculations are only statistical in nature, because, as I have demonstrated above, half of the total GrIS ice loss is attributable to glacier imbalance, whose spatial scales and underlying dynamics (e.g., calving) are still beyond current modeling capacities (even with regional climate models). The summer *GSI* obtained from

the nudging run accounts for about 40% of the interannual variability in the GrIS annual mean mass balance (MB; The IMBIE Team 2020) whether or not the underlying trend is removed over 1980-2018 ($r_{GSI;MB}$ = -0.67 (-0.62) for raw (linearly detrended) data). Similar correlations using detrended and raw data motivates the construction of a simple linear regression model to quantify the *GSI*-driven Greenland ice mass loss acceleration since 1990. After regressing out the summer *GSI* time series derived from the nudging experiment from the GrIS annual mean rate of mass balance anomaly over 1980-2018 (Figure 3.2-5e), I find that the GSI contributed ~54% of the GrIS mass loss acceleration over 1990-2012 regardless of using linearly detrended or raw data to construct the regression model. *This indicates that a substantial portion, –71.7 Gt yr^{-1} decade^{-1} (out of the –132.8 Gt yr^{-1} decade^{-1}) total ice mass change equalling ~0.2 mm yr^{-1} decade^{-1} sea-level rise acceleration related to wind-induced adiabatic warming between 1990-2012, which holds potential for atmospheric circulation to affect the rate of sea-level rise to a similar extent in the coming decades.*

3.2.4 Fingerprints of remote forcing on the GrIS since 1979

I have discussed challenges in quantifying the relative contributions from internal/forced sources behind the observed GrIS ice loss and consequent sea-level rise. I follow-on this discussion first by studying the extent to which the local GrIS circulation variability is excited by remote forcing, i.e., teleconnections induced by tropical *SST* anomalies. Examining the large-scale picture is important to shed more light on the sources of model biases in simulating the local GrIS circulation-surface coupling, since known limitations of climate models to replicate tropical-Arctic linkages are likely to play a role in the aforementioned model uncertainties (*Topál et al. 2020a*). Then I assess whether this large-scale mechanism is stable beyond the observational era by utilizing paleoclimatic proxy-data assimilated model experiments and ice-core/oceanic coral derived temperature

proxies over the past 400 years. Through these analyses, I strive to refine the pathway ($\mathbf{A_2}$) by which large-scale winds impact GrIS melt, particularly during the period before 1850 under less anthropogenic forcing relative to present day, as a next step to contextualize the model sensitivity issues.

In an effort to address these complexities I utilize that besides describing the local atmosphere-GrIS coupling, the *GSI* inherently contains information from the rotational feature of large-scale atmospheric circulation. This enables to study how the local atmospheric circulation variability may be excited by forcing from the lower latitudes. The linearly detrended correlations between the *GSI* and global *Z500* and *SST*, despite differences in the magnitudes between the JJA and annual mean correlations (Figure 3.2-8), show features of a teleconnection linking tropical Pacific cold *SST* anomalies with anomalous Greenland warming as seen in previous studies (Ding et al. 2014; *Baxter et al. 2019*; Ballinger et al. 2021). Using maximum covariance analysis (MCA, **Section 2.6**), I reveal the primary internal coupled mode of variability between *Z500* and *SST*. The MCA(1)[4] spatial patterns of *Z500* (Figure 3.2-9a) and *SST* (Figure 3.2-9b) exhibit a hemispheric teleconnection bridging atmospheric circulation variability over the GrIS with opposite-sign (negative Pacific Decadal Oscillation (PDO)-like) changes in the tropical Pacific, and same-sign (positive Atlantic Multidecadal Oscillation (AMO)-like) changes in the tropical Atlantic. This mode explains ~55% covariability between large-scale circulation and *SST* (Figure 3.2-9c) and shows robust correspondence with the observed rate of Greenland ice loss especially between 1990-2012 (r ~ 0.6). The regression of 200hPa streamfunction onto the *Z500* expansion coefficient time series (Figure 3.2-9a) resembles the Pacific-Arctic (PARC) teleconnection (*Baxter et al. 2019*) and hence indicates the key role of tropical forcing in forming the mid-tropospheric high-pressure

[4] MCA(n) refers to the nth leading mode.

pattern over Greenland through the propagation of stationary Rossby-waves (Ding et al. 2014) (Figure 3.2-9a). *This result, alongside a regression of Z500 time series on the year-to-year variability of 200hPa horizontal winds and GrIS SAT in Figure 3.2-9d support the idea that a substantial portion of the observed local GrIS high-pressure is likely driven by remote tropical forcing, however the quantification remains uncertain.*

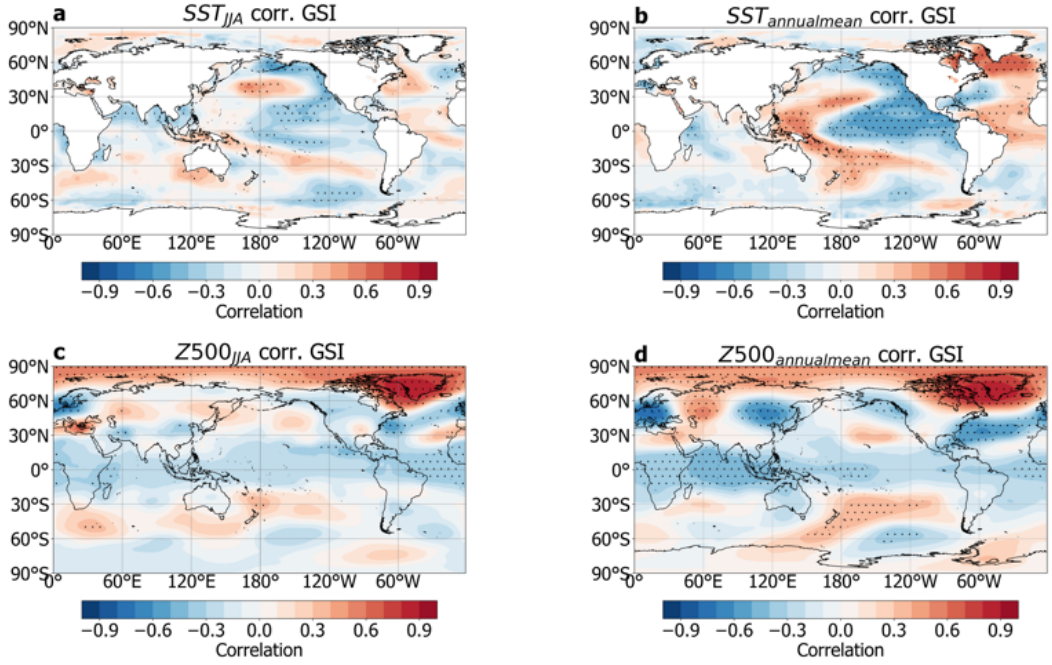

FIG. 3.2-8. Year-to-year connection between the *GSI* and global atmospheric circulation and *SST*. Correlation between detrended 500hPa Greenland streamfunction index (*GSI*, **Section 2.9**) and detrended sea surface temperatures (*SST*) in (a) summer (June-July-August, JJA) and in (b) the annual means using ERA5 and ERSSTv5 for 1980-2018. Hatching indicates statistically-significant correlations ($p<0.05$).

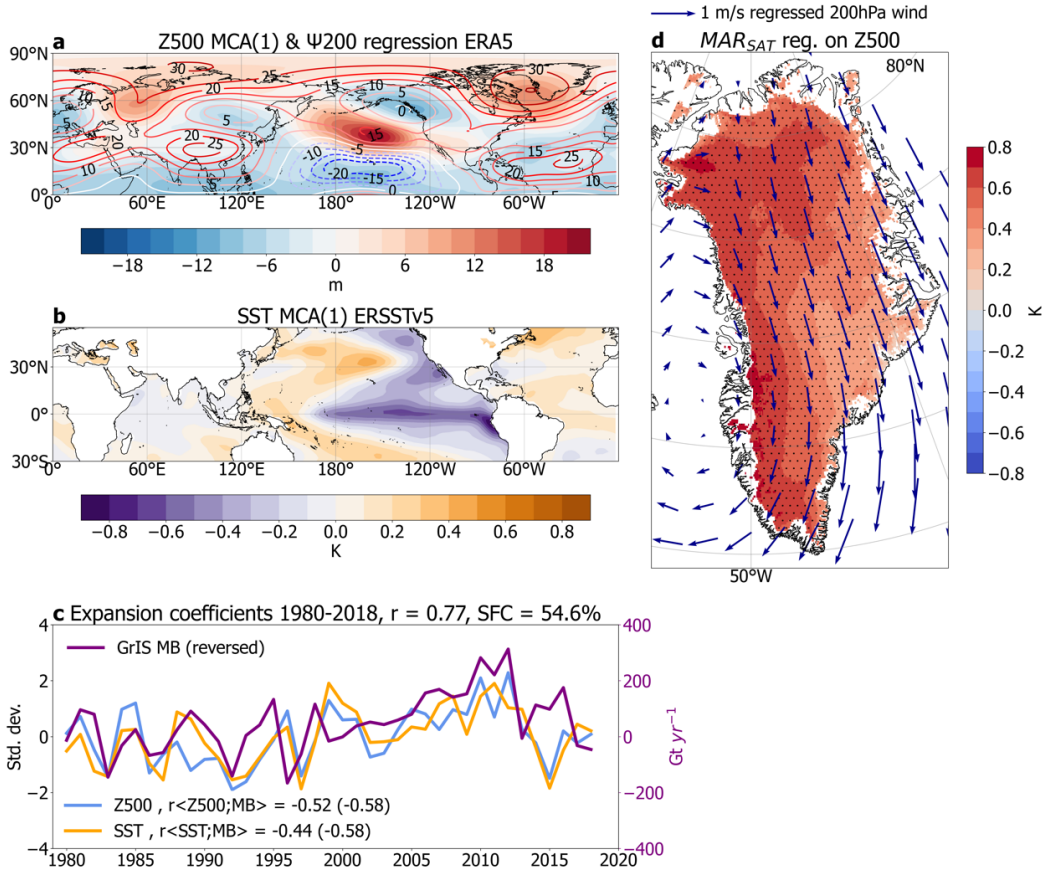

FIG. 3.2-9. The contribution of remote forcing to high-pressure driven adiabatic processes over the GrIS during 1980-2018. Spatial patterns corresponding to the leading internal mode of covariability between Northern Hemisphere annual mean (a) ERA5 500hPa geopotential height (*Z500*) and (b) sea surface temperatures (ERSSTv5, *SST*) (30°S-55°N). The corresponding expansion coefficients (EC, shown as units of standard deviations) for Z500 (blue) and *SST* (ERSSTv5, orange) as revealed by maximum covariance analysis (MCA, **Section 2.6**) also shown in (c). The shared fraction of covariance (SFC) is 54.6% and the correlation between the ECs is r=0.77. The area-weighted global mean is removed before MCA from *Z500* and the 60ºS-60ºN mean from *SST*. Panel (c) also shows the spatially-averaged GrIS mass balance (*MB*) anomaly time-series from The IMBIE Team (2020) (purple) and the correlation between the MB and the Z500/SST expansion coefficients over 1980-2018 in the legend (with brackets showing correlations over 1990-2012). In (a), the regression of Z500 EC(1) onto the 200hPa streamfunction (Ψ200) calculated from ERA5 is shown with contours overlaid (unit: $10^6 m^2 s^{-1}$). Panel (d) shows the regression of Z500 EC(1) onto the MAR simulated surface air temperatures (SAT) (shading) and ERA5 200hPa horizontal winds (blue arrows) for the GrIS.

3.2.5 Tropical forcing on the GrIS since 1603 AD

Recent studies have raised concerns about non-stationary features of tropical-Arctic teleconnections (Bonan and Blanchard-Wrigglesworth 2020) that cast doubt on the reliability of using this framework to guide future climate projections over Greenland. Therefore, I address this point by evaluating the observed teleconnection's impact on GrIS warming over centennial time scales using the Ensemble Kalman Fitting 400 (EKF400) paleo-reanalysis version 2 (Valler et al. 2021) spanning 1603-2002 AD. This dataset was created by assimilating early instrumental temperature, surface pressure and precipitation observations, temperature and moisture sensitive proxies from tree-ring measurements into the ECHAM5.3 atmospheric general circulation model (see also **Section 2.2** for details).

Having repeated the MCA between *Z500* and *SST*, the leading internal SST-Z500 coupled mode in the EKF400 explains nearly the same (~50%) covariance as the PARC and features strikingly similar spatial patterns to their observed counterparts (Figure 3.2-10a-b vs. Figure 3.2-9a-b). To further emphasize the dynamical linkage between the tropics and Greenland, I regress the 200hPa streamfunction from EKF400 onto the *Z500* expansion coefficient time series. The resulting regression map closely resembles the one seen using the ERA5 reanalysis (Figure 3.2-10a vs. Figure 3.2-9a). Furthermore, the significant correlations between the *SST* MCA(1) time series and the PDO* ($r \sim -0.9$, **Section 2.2**) or the AMO* ($r \sim 0.4$, **Section 2.2**) indices calculated from the EKF400 as well as an Atlantic Meridional Overturning Circulation (AMOC) index reconstruction (Rahmstorf et al. 2015) ($r \sim 0.4$) altogether suggest that the notable multidecadal low-frequency variabilities seen in the *Z500* and *SST* MCA(1) time series are analogous to these well-known indices of multidecadal climate variability. In addition, 15 out of the 30 ice core δ^{18}O records available across the ice sheet, and 10 out of 33 available oceanic coral δ^{18}O records from

PAGES2k Consortium (2017) show statistically significant correlations with the EKF400-derived *GSI* (triangles in Figure 3.2-10c-d; Supplementary Table 1).

These observational constraints along with the regression maps of the *Z500* expansion coefficient time series onto the *SAT* and 200hPa horizontal winds over the ice sheet (Figure 3.2-10d) closely match the circulation-surface coupling seen in the observations, and together bolster confidence that the observed large-scale wind-driven Greenland changes are part of a mode of large-scale variability that is consistent over at least the past 400 years. To verify the EKF400 results, I repeated the MCA using the Last Millennium Reanalysis (Tardiff et al. 2019). Although discrepancies exist between the two paleo-reanalyses, they altogether *support the idea that the significant enhancement of GrIS melting between 1990-2012 and associated acceleration in the rate of sea-level rise have been a manifestation of low-frequency variability in the climate system, predominantly arising from natural variability (Ding et al. 2017; Baxter et al. 2019).*

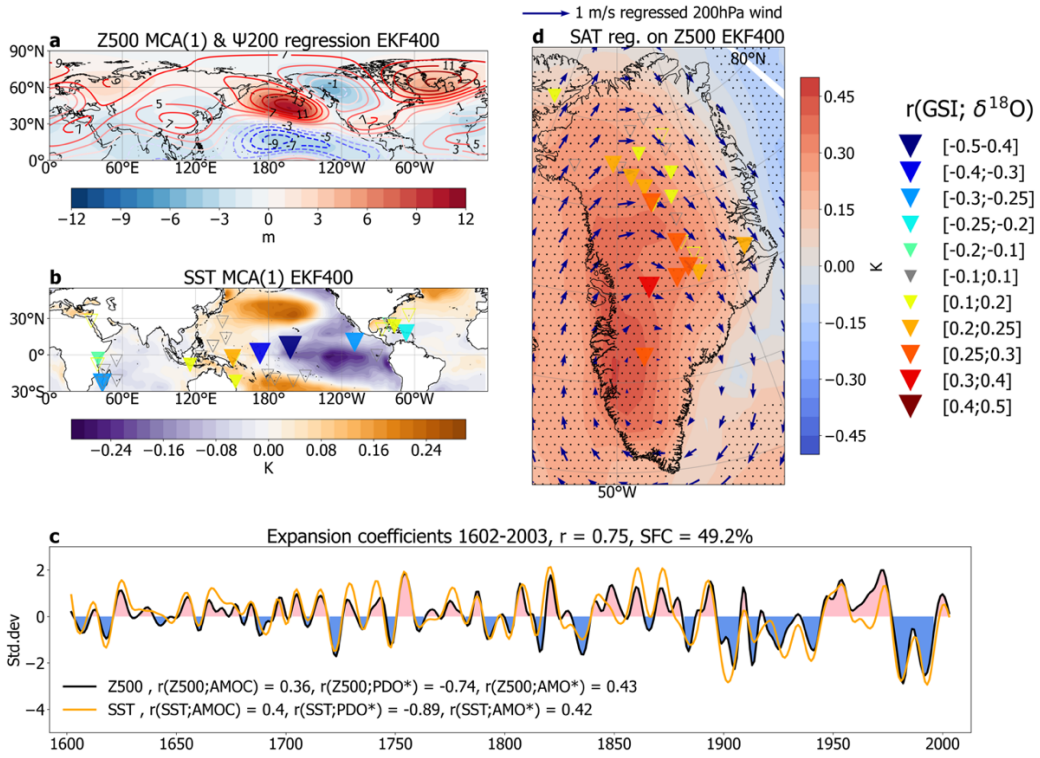

FIG. 3.2-10. The temporal consistency of the observed teleconnection influencing Greenland over AD 1602-2003 as simulated by the EKF400. Spatial patterns corresponding to the leading internal mode of co-variability between Northern Hemisphere annual mean (a) 500 hPa geopotential height (*Z500*) and (b) sea surface temperatures (*SST*) (30°S-55°N) and (c) the corresponding expansion coefficients (EC, shown as units of standard deviations) for *Z500* (blue) and *SST* (orange) as revealed by maximum covariance analysis (MCA, **Section 2.6**) in the Ensemble Kalman Fitting (EKF400) paleo-reanalysis over 1602-2003. The ECs are filtered with a 10-yr lowpass filter to elucidate decadal variability. The shared fraction of covariance (SFC) is 49.2%, the correlation between the ECs is r=0.75. The area-weighted global mean is removed before MCA from Z500 and the 60ºS-60ºN mean from SST. Panel (c) also shows the correlations between the (non-filtered) ECs and an Atlantic Meridional Overturning Circulation (AMOC) reconstruction (Rahmstorf et al. 2015) and the EKF400 derived Pacific Decadal Oscillation (PDO) and Atlantic Multidecadal Oscillation (AMO) indices (**Section 2.2**) in the legend. In (a) the regression of *Z500* EC(1) onto the 200hPa streamfunction *(Ψ200)* calculated from EKF400 is shown with contours (unit: $10^6 m^2 s^{-1}$). Panel (d) shows the regression of Z500 EC(1) onto *SAT* (shading) and 200hPa horizontal winds (blue arrows) for the GrIS in the EKF400, while the triangle markers correspond to the correlation between the *GSI* derived from EKF400 and 30 individual ice core records across the ice sheet with filled triangles indicating significant correlations ($p<0.05$) (also see Supplementary Table 1). Hatching indicates statistically significant regression values ($p<0.05$). In (b), the triangles correspond to the correlation between the 500hPa Greenland streamfunction index (GSI) derived from EKF400 and 33 individual coral records from PAGES2k with filled triangles indicating significant correlations ($p<0.05$).

3.2.6 Possible mechanisms behind the observation-model discrepancies

Results based on the wind-nudging experiment highlight the contribution of large-scale winds to rapid Greenland warming, the acceleration in GrIS mass loss and related sea-level rise since the early 1990s through a tropically-excited teleconnection that modulates the high-pressure driven adiabatic warming over the ice sheet. This constitutes a new framework for tropical decadal variability to influence global sea-levels through GrIS-related barystatic sea-level rise in addition to regulating ocean thermal expansion (Han et al. 2014; Hamlington et al. 2019). The out-of-phase relationship between tropical Pacific *SST* and Greenland *SAT* anomalies associated with the PARC teleconnection results in accelerated GrIS melt and thus an increase in sea-levels during PDO-negative, which counteracts the coherent decrease in ocean thermal expansion and the increase in ocean-to-land water transport yielding a drop in sea-levels (Boening et al. 2012). This may explain why GrIS-driven barystatic sea-level rise shows acceleration since the 1990s, whereas the rate of thermal expansion-related sea-level rise is rather constant (Chen et al. 2017). Although the quantification of the tropical forcing in regulating the local wind-driven process remains unclear, evidence based on paleo-reanalyses and proxy records lends temporal credibility to the persistence of the abovementioned pathway.

To further discussion on the forced/internal nature of observed GrIS surface and overlying circulation changes, I show the contrast between temperature changes over the GrIS in ERA5 and in the forced response in the CESM-LE (ensemble mean) by examining the summertime trend in temperature, geopotential height, and vertical motion (omega) zonally averaged over the ice sheet (Figure 3.2-11). In contrast to the vertical structure of temperature and geopotential height changes accompanied by significant *downward motion* in the lower troposphere in ERA5 (Figure 3.2-11a), the 40-member ensemble mean reflects anthropogenically-induced warming processes by simulating *vertically uniform*

temperature and geopotential height changes associated with *upward vertical motion* (Figure 3.2-11b). Imposing ERA5 winds in the CESM1, however, captures the observed vertical temperature and geopotential height structures as well as the *downward motion* (Figure 3.2-11c) albeit with differences in the boundary layer likely related to vertical resolution of the CESM1. These features are also seen on the corresponding correlation maps between the *GSI* and the zonally averaged temperature over the ice sheet (Figure 3.2-11d-f). *This analysis may offer a guide to future efforts targeting the nudging of winds in other climate models – possibly at higher resolution to better account for boundary layer processes, e.g., inversions, which are suggested to be a key contributor to GrIS surface changes (Shahi et al. 2020) –, and also points to a possible source of model deficiency that needs further attention and evaluation to better constrain the forced temperature response over the ice sheet.*

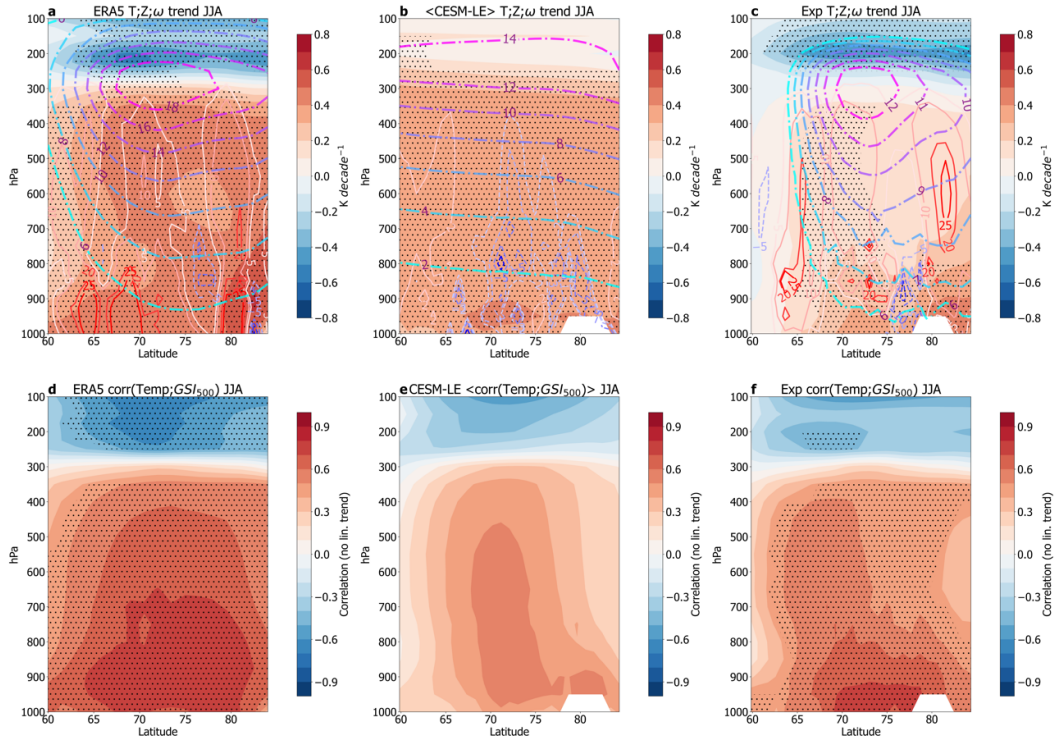

FIG. 3.2-11. Possible physical mechanism behind the observed model deficiencies. Linear trend in zonal-mean temperature (shading: statistically significant values are hatched; $p<0.05$), zonal-mean geopotential height (dash-dot contours; unit: m/decade) and vertical motion (omega; solid contours; unit: 10^5 Pa/s) over the GrIS (59ºN-85ºN;80ºW-20ºW) in (a) ERA5, (b) the mean of 40-members (forced component) of the CESM-LE and (c) nudging experiment between 1980-2018 JJA. Correlation (statistically significant values are hatched; $p<0.05$) between detrended zonal-mean temperature over the GrIS and 500hPa Greenland Streamfunction Index (GSI) in (d) ERA5, (e) the mean of the 40 individual correlation maps of the CESM-LE and (f) in the nudging experiment between 1980-2018 June-August (JJA).

3.3 Reassessing regional Arctic climate sensitivity and its possible biases

This Section is based on Topál and Ding (in prep).

In the previous two Sections we have seen how atmospheric processes, partially originating from low-frequency tropical SST decadal variability that is inherent to the climate dynamics, influence Arctic sea-ice and GrIS melting in summer. At the same time, significant model uncertainties were highlighted along with possible explanations behind the observed discrepancies between the observed and simulated melting processes.

Continuing on the latter thread, I now describe progress made towards reassessing Regional Climate Sensitivity in the Arctic (RCS_A) in numerous climate models by using large-scale atmospheric circulation as an emergent constraint (Notz 2013; Hall et al. 2019) on Arctic warming in three SMILEs (Deser et al. 2020), 31 CMIP5 and in 29 CMIP6 models. In doing so, I generate a circulation index in the Arctic to measure atmospheric forcing and then statistically remove its impact from Arctic *SAT*, sea-ice and GrIS *SMB* in both observations and model simulations separately (**Section 2.11**). Considering that the SMILE means show only weak circulation changes in the Arctic since 1979 (as I have shown in **Sections 3.1 and 3.2**), a direct comparison of the residual parts more clearly reflects the response to the same anthropogenic forcing over the past decades in the real world and model environments than doing the same with the raw outputs. This also allows for a recalibration of models' RCS_A over the historical period, that is further used to constrain Arctic model projections assuming that RCS_A is relatively stable in future global warming scenarios. In what follows, I will show that it is essential to account for the influence of atmospheric forcing on Arctic sea-ice and the GrIS when interpreting their transient sensitivities to anthropogenic emissions with major implications for the timing of the first seasonally sea-ice-free Arctic Ocean and widespread GrIS melting in the coming decades.

3.3.1 Divergent modelled and observed sensitivities

To address the aim $\mathbf{A_4}$, I utilize the method described in **Section 2.10** and **2.11**. In doing so I first create indices of the global 300-hPa horizontal wind-based streamfunction (*Ψ300*) and SAT by spatially averaging over the Arctic (*ASI*) and over the GrIS (*GSI*), respectively (see **Section 2.9**). Recall, that the *ASI*/*GSI* measures the rotational component of atmospheric circulation variability and warming intensity over the Arctic/Greenland primarily through adiabatic processes. Next, I calculate *R* (as defined in **Section 2.10**) using a linear regression-based approach to quantify the sensitivity of Arctic (GrIS) *SAT*s (R_{SAT}) to upper-level large-scale circulation changes (as shown in the top x-axis in Figure 3.3-1). These calculations are intended to showcase differences between the observed and modelled *SAT* sensitivities to large-scale circulation: as opposed to the significant reduction in *SAT* trends in ERA5 over the Arctic (GrIS) after having regressed out the *ASI* (*GSI*), each and every member of the model ensembles indicate less of an influence from the *ASI/GSI* on *SAT* variability (Figure 3.3-1). The ensemble mean R_{SAT} values in models are ~34% (~50%) biased high compared to the reanalysis for the Arctic (GrIS) (Figure 3.3-1). Note that those 50 members of the CESM2-LE with observationally constrained biomass burning (BB) emissions (see more details on the CESM2-LE experimental design here) align better with the observed *raw* surface temperature trends (measured on the y-axis in Figure 3.3-1a-b) than of those without constraining BB emissions (DeRepentigny et al. 2022; Fassulo et al. 2022). However as for the *residual* trends (measured on the x-axis in Figure 3.3-1a-b) it is no longer the case. This indicates that BB emissions cause enhanced surface warming without much interaction with atmospheric circulation. Moreover, those CMIP6 models simulating the largest (e.g., CanESM5, E3SM-1-1, CESM2-WACCM) and smallest (e.g., MIROC6, NorESM2, GFDL-ESM4) amounts of Arctic warming (Tokarska et al. 2020) are indistinguishable in terms of their simulated R_{SAT} values (Figure 3.3-1c-d).

Hence their higher sensitivity to CO_2 forcing is unlikely to be a consequence of better simulating atmospheric circulation changes. I also extended the calculations to the vertical cross-section of zonal mean temperatures over the Arctic and the GrIS, respectively, which yield similar results (Supplementary Figure 5).

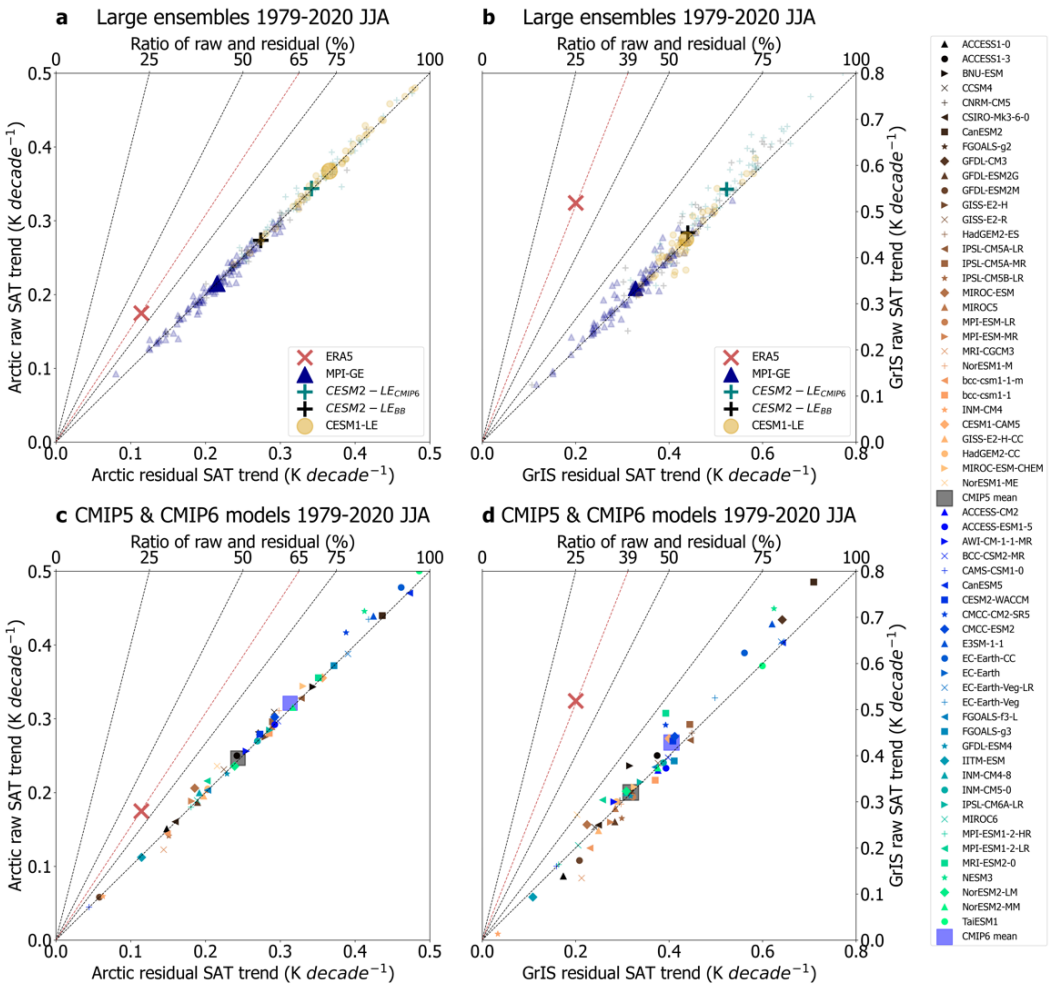

FIG. 3.3-1. Mismatch between observed and modelled sensitivity of Arctic and GrIS surface temperature changes to large-scale circulation. Scatterplot of the raw and residual (obtained as regressing out the *GSI*/*ASI* from Arctic/GrIS *SAT* over 1979-2020 period in summer, June-July-August) *SAT* trends over the Arctic (panels a) and c)) and over the GrIS (panels b) and d)) in ERA5 (a)-(b), in three SMILEs and (c)-(d) in 31 CMIP5 and 29 CMIP6 models (see legend). The small, transparent markers refer to the individual ensemble members, while the larger markers are the ensemble means. The CESM2-LE in panels (a)-(b) is separated into 50-members forced by CMIP6 standards and 50-members with prescribed biomass burning emissions (BB). Note the upper x-axes in each of the panels, which refer to the *R* values (**Section 2.10**).

To further assess the robustness of the above findings I examine 40-year rolling-window (linearly detrended) correlations between the *ASI* (*GSI*) and *SAT* over the Arctic (GrIS) using the ERA and NOAA 20th century reanalysis products in addition to the full length of the historical simulations in the SMILEs (1850-onwards) (Figure 3.3-2). Each 40-yr long period can be considered as parallel realizations of the past four decades and thus helps to increase confidence in the results. Both reanalyses exhibit notable low frequency oscillations in the correlation between large-scale atmospheric circulation and *SAT* similarly over the Arctic and the GrIS, with a significant upward trend over the past century such that the circulation-surface connection over 1979-2020 is the strongest over the past 150 years (Figure 3.3-2a-b). The reliability of the observational data steeply reduces with going back in time and uncertainties between the two reanalyses are as well acknowledged, however the similarities between the ERA and NOAA products after 1940s (onward the 1936-1975 40-yr period) is reassuring.

In contrast to reanalyses, the ensemble means of 40-yr rolling-window correlations (computed in each member separately, then averaged) across the three SMILES are rather constant or indicate slight weakening. In addition, computing the correlations across the ensemble members – instead of in each member separately – in each year offers new perspectives (Tél et al. 2020) in studying the forced response of the modelled connections between *SAT* and large-scale circulation. Hence, I calculate the ensemble-wise correlation coefficient (Herein et al. 2017; *Haszpra et al. 2020a*; Haszpra et al. 2020b) between the *ASI*/*GSI* and the respective surface temperature indices (Figure 3.3-2c-d). All three models indicate slight, but statistically significant weakening of the circulation-surface connection in response to anthropogenic emissions over the Arctic and the GrIS (Figure 3.3-2c-d) in contrary to observations.

This mismatch suggests that the observed increasing influence of large-scale circulation on Arctic climate over the past four decades (Figure 3.3-2a-b) is unlikely to be a forced response and raises concerns about the realistic representation of Arctic climate sensitivity to anthropogenic emissions in contemporary climate models.

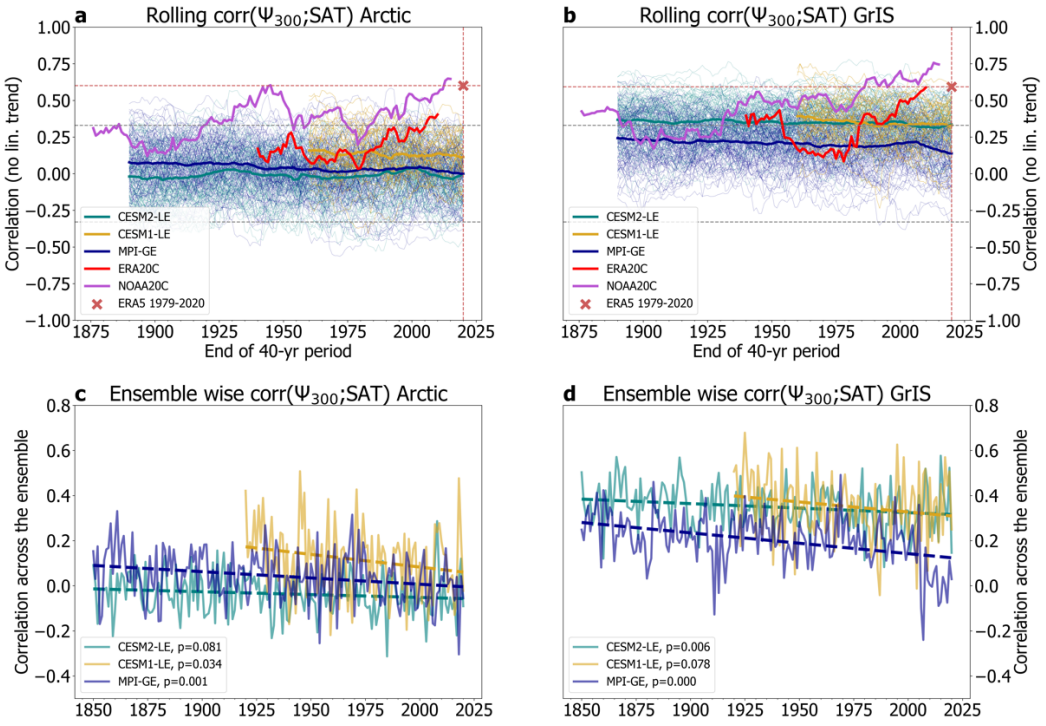

FIG. 3.3-2. Divergent changes in the influence of large-scale circulation on Arctic surface temperatures in reanalyses and in the models' forced response. 40-yr rolling window correlations between SAT and the large-scale circulation index (GSI/ASI) over the (a) Arctic and (b) GrIS in reanalyses and SMILEs (see legend). The linear trend in removed from each variable before computing the correlations. As for the SMILEs, the correlations are computed in each individual members (thin lines) and then the average of the individual correlations are shown with the thick solid lines. Also shown: ensemble-wise correlations between *SAT* and large-scale circulation index (*ASI*/*GSI*) over the (c) Arctic and (d) GrIS in the three SMILEs and the linear trend fitted into the time series (dashed-line) and their p-values in the legend. The ensemble-wise correlation coefficient is used to estimate the forced response in the connection between atmospheric circulation and *SAT* to anthropogenic emissions. Note that the convergence time in the CESM-LE may affect the ensemble-wise correlations (Drótos et al. 2015).

3.3.2 Constraining projected Arctic climate change

Here, I illustrate how the abovementioned mismatch between the modelled and observed Arctic *SAT* sensitivities to atmospheric forcing impacts future Arctic temperature projections. To do so, I constrain the modelled forced response projections so that the *R* values corresponding to the ensemble means and the observation, respectively, become identical over 1979-2020 while assuming that the ensemble spread remains the same (see details in **Section 2.11**). Since the models' ensemble mean *R* values are greater than the observed (circulation is less prominent to cause warming in models than in observations), each ensemble shows slower warming in their future projections (2021 onwards) than their unconstrained time series. *This also means, that the global mean temperature response to global warming, which is very well simulated by current climate models, may not offer a comprehensive-enough picture when studying* RCS_A.

To showcase this point, I study the timing of three certain temperature thresholds (1ºC, 1.5ºC and 2ºC above pre-industrial levels, i.e., 1850-1900) to be crossed in the Arctic summer by plotting the corresponding cumulative density functions (Figure 3.3-3, **Section 2.12**) in the CESM2-LE, MPI-GE and in 29 CMIP6 models (these models provide long-enough data for 1850-2100). The results (Figure 3.3-3) indicate a consistent ~20-year delay (±5 years) in reaching each temperature threshold as a consequence of having constrained the modelled forced response. Hence, it is advisable to take caution when interpreting the RCS_A based on the capability of climate models to reproduce the global mean surface temperature.

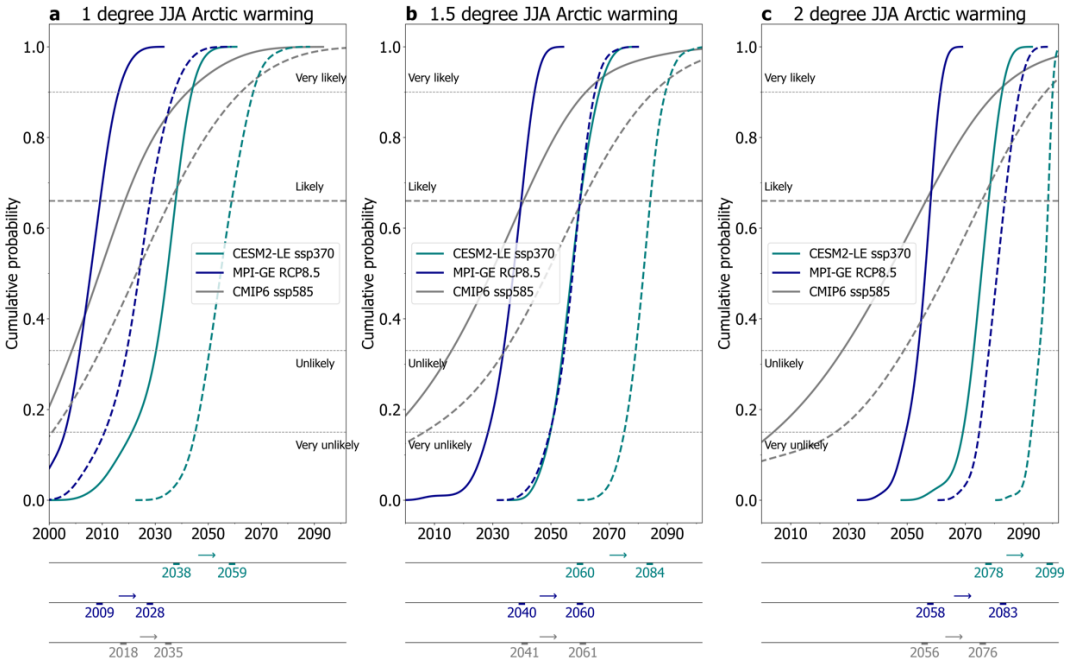

FIG. 3.3-3. Constraining projected Arctic warming. Cumulative probability density functions (CDF) corresponding to the date of (a) 1ºC, (b) 1.5ºC and (c) 2ºC warming above pre-industrial levels in the CESM2-LE and MPI-GE SMILEs and in CMIP6. The solid (dashed) lines indicate the raw (constrained) CDF (**Section 2.13**). The dates below the x-axes refer to the prospective delays introduced by matching the modelled sensitivities to large-scale circulation with observations over 1979-2020.

I further elaborate on these model limitations' impacts on the simulated RCS_A by translating the above results to September sea-ice extent (*SIE*) and JJA GrIS *SMB* in observations, the SMILE members and in the CMIP-class models (only the CESM2-LE for *SMB*). In doing so, I quantify the extent to which the *SIE* and *SMB* sensitivities to CO_2 forcing (the reduction in *SIE*/*SMB* per a tonne of observed CO_2 emission over 1979-2020; **Section 2.10**) change after linearly regressing out the corresponding streamfunction indices (*ASI*/*GSI*) compared to the raw CO_2 sensitivities by deriving R_{SIE} and R_{SMB} (**Section 2.10**). The discrepancies between the observed and modelled R_{SIE} (R_{SMB}) values (Figure 3.3-4a-b) suggest that the models have unrealistically low sensitivity to atmospheric forcing accompanied by an overall high sensitivity to CO_2 forcing in the Arctic, as indicated by the

ensemble mean R_{SIE} (R_{SMB}). I repeat the constraining method (performed on *SAT*) on future projections of sea-ice (and GrIS *SMB* in the CESM2-LE) by matching the ensemble mean R_{SIE} (R_{SMB}) to its observed counterpart over the 1979-2020 period (**Section 2.12**). The cumulative probability density functions corresponding to the time of emergence of the first seasonally sea-ice-free Arctic (below 1 million km^2 *SIE* in September) in the raw and the constrained *SIE* time-series in the model ensembles show prospects of a 9–11-year delay of the 'likely' (in IPCC Climate Change (2013) terms) probability ($P > 0.66$) of a September ice-free Arctic, such *that it is not likely to see an ice-free summer before 2050* (Figure 3.3-4c, **Section 2.12**). As for the GrIS, adjusting the CESM2-LE's *SMB* projections to match the observed sensitivity to atmospheric forcing yields a 15-year delay of the 'likely' probability of widespread GrIS melting (when SMB<0 see **Section 2.11**; Figure 3.3-4d).

Hence, accounting for the RCS_A bias in the models moderates the projected Arctic warming and sea-ice loss, which is starkly at odds with previous results so far (Bonan et al. 2021; Laliberté et al. 2016; Wang et al. 2009; IPCC Climate Change 2013). The reason for this controversy may be that by using surface temperature to constrain the modelled RCS_A previous studies had the impression that models underestimate the warming signal (e.g., Bonan et al. 2022) and conclude that the underestimation is due to their low sensitivity to anthropogenic emissions. *In turn, I suggest that the models' low sensitivity to atmospheric forcing can result in too strong Arctic warming- and a high sea- and land-ice sensitivity to anthropogenic forcing if the priority criteria to evaluate model performance is based on matching the simulations with observations.*

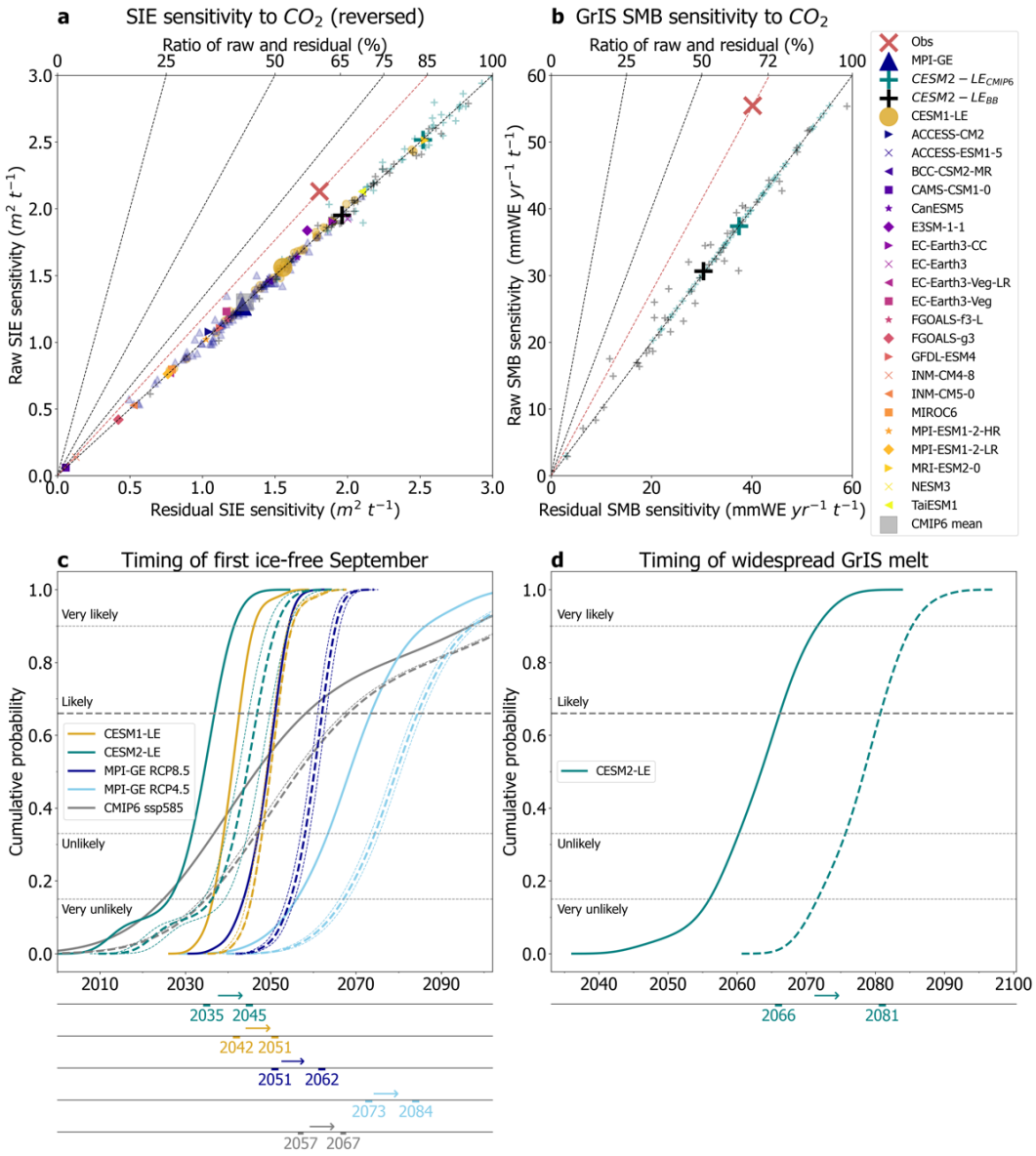

FIG. 3.3-4. Constraining the date of the first sea-ice free September and widespread GrIS melting. (a)-(b) is the same as in Figure 3.3-2a-b, but for September *SIE* (a) and GrIS *SMB* (b) sensitivities to observed cumulative CO_2 emissions. The small, transparent markers refer to the individual ensemble members, while the larger markers refer to the ensemble means. Note the upper x-axes in each of the panels, which refer to the *R* values (**Section 2.10**). Also shown: cumulative probability density functions of (c) the ice-free date in three SMILEs and in CMIP6 and (d) widespread GrIS melting in the CESM2-LE shown for the raw (solid lines) and the constrained model projections (dashed-lines) (**Section 2.12**). The thin dashed lines indicate the uncertainty due to the selection of the window-size used to estimate the constrained ice-free dates (**Section 2.12**). The dates below the x-axes refer to the prospective delays introduced by matching the modelled sensitivities to large-scale circulation with observations over 1979-2020.

3.3.3 Possible underlying causes of the sensitivity issues

Previous studies have recognized the crucial role of observed atmospheric circulation changes in causing sea- and land-ice melting as well as upper-ocean warming in the Arctic using numerical model simulations with the CESM1 (Baxter et al. 2022; Ding et al. 2022; Li et al. 2022; *Topál et al. 2022*; Roach and Blanchard-Wrigglesworth 2022). These reinforce the simple statistical approach taken in this Section and support the physical interpretation behind the hereby suggested constraining method. In addition, the arguments raised here are irrespective of whether the underlying cause of the sensitivity issue lies in an insufficient simulation of atmospheric forcing response to CO_2 (Roach and Blanchard-Wrigglesworth 2022) or that internal variability is what dominantly cause the observed circulation changes. Previous studies also assess the probability of an ice-free summer corresponding to a certain (annual mean) global warming level (Screen and Williamson 2017; Jahn 2018; Niederdrenk and Notz 2018; Sigmond et al. 2018), which approach seems to circumvent the sensitivity problem (the focus is elsewhere). Nevertheless, it does matter when and how we get to those certain global warming levels that can no longer host a frozen Arctic. *I speculate that since the global mean temperature response to CO_2 forcing seems insufficient to scale the Arctic climate response, my concerns translate into uncertainties of the probabilities of an ice-free Arctic at 1.5ºC or 2ºC global warming above pre-industrial levels.*

The observed changes in Arctic circulation are likely in part driven by tropical Pacific decadal SST variability (Ding et al. 2014), which can generate strong upper-level divergence and convergence in the tropics (see Eq. 4 in **Section 2.9**) that further serves as the main source to create strong rotational winds in the high latitudes through Rossby-wave dispersion. However, the models' forced responses do not favour a low frequency change in the rotational component of Arctic winds likely associated with that under global

warming scenarios models exhibit rather horizontally uniform SST response in the tropics, which obstructs the excitement of upper-level divergence and convergence changes. Hence, this mismatch between observations and models is likely to play a role in explaining the main underlying cause why models simulate much weaker low frequency changes of the rotational component of large-scale circulation in the Arctic.

The new constraint on models' RCS_A presented here has important implications for the interpretation of current climate change projections for the Arctic and the future development of climate models. Studies have attempted to address possible biases in sea-ice simulation, however, recalibration efforts that adjust modelled surface temperature trends to observations (Stroeve et al 2007; Screen and Simmonds 2010; Winton 2011;) are an interim fix to make predictions about the future of Arctic sea-ice, especially if the discrepancy between modelled and observed sea-ice loss is due to internal variability, which remains an open question (Moritz et al. 2002; Swart et al. 2015; Ding et al. 2019). The discrepancies between observed and simulated *R* values identified in this study suggest that the contribution of large-scale circulation forcing in recent Arctic warming, regardless of its origin being internal or forced, allows us to evaluate models' sensitivity to anthropogenic forcing from new lens when there is a growing concern about the oversensitivity of models to anthropogenic forcing (Fyfe and Gillett 2014; Tokarska et al. 2020; Zhu et al. 2020; Hausfater et al. 2022).

3.4 Central European summer hydroclimate projection uncertainties

This Section is based on Topál et al. 2020b.

Apart from changes in the Arctic, another region-specific focus of this dissertation arises from the fact that hydroclimate projections of CMIP-class global climate models diverge to a great extent in Central and East-Central Europe (Figure 3.4-1). In **Section 1.4** I introduced the key challenges that we need to face when assessing the robustness of future precipitation projections in our region. To resolve these uncertainties previous studies developed diverse model ranking methodologies, ranging from studies using correlation, root-mean-square error and variance ratio (Boer and Lambert 2001; Gleckler et al. 2008) to the application of prediction indices (Murphy et al. 2004) or to those taking a Bayesian approach (Min and Hense 2006). In addition, Olson et al. (2019) re-evaluated the interdependency of CMIP models (Sanderson et al. 2015) as another potential uncertainty. Regarding the target area of model evaluation Garfinkel et al. (2020) studied the sources of CMIP5 intermodel spread in precipitation changes globally, however, ample analyses is targeted at more regional areas, e.g., the North Atlantic (Perez et al. 2014), parts of Europe (Coppola et al. 2010; Pieczka et al. 2017), Africa (Brands et al. 2013; Dyer et al. 2019; Yapo et al. 2020), South America (Lovino et al. 2018) or Asia (Ahmed et al. 2019).

In this Section I describe an approach I took to evaluate East-Central European hydroclimate model projection uncertainties using multiple CMIP5 and SMILE simulations.

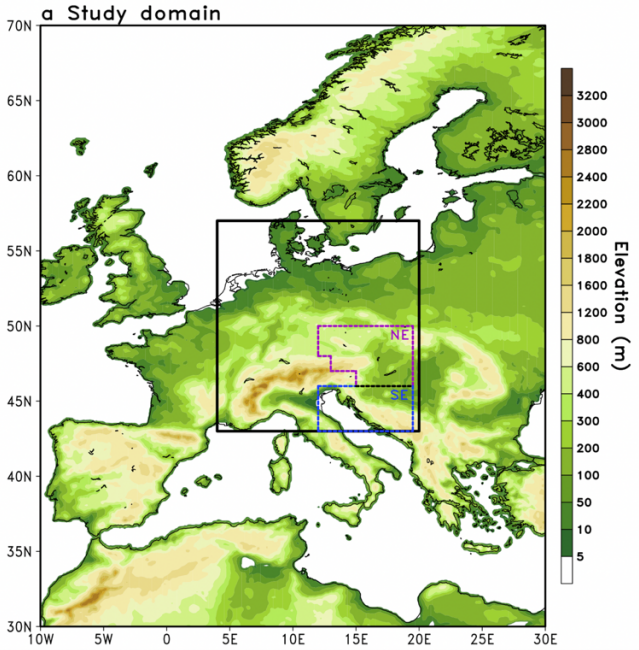

FIG. 3.4-1. Location of the study area on an orography map. The purple and blue dashed lines represent the HISTALP Northeast (NE) and Southeast (SE) regions. The primary target area is selected as the rectangle overlapping the NE and SE regions, i.e. 43°N-50°N;13°E-19.5°E. The black rectangle represents the Central Europe (CEU) domain (extended target area) used to evaluate CMIP5 models against the NOAA 20th century reanalysis. *This Figure is adopted from Topál et al. (2020b).*

3.4.1 Assessing historical performance of CMIP5 models

To begin with, I assess the historical performance of 32 CMIP5 models (**Table 1**), based on the HISTALP observations (**Section 2.15**; 1861-2005) and use the ranking method introduced in **Section 2.16**. In doing so, at first *RMSE*, *rank* and *NSE* were calculated for the NE and SE subregions for both summer (JJA) and winter (DJF) seasons separately, then averaged over the primary target area. Then I average the seasonal statistics and obtain the mean *RMSE*, *rank* and *NSE* (Figure 3.4-2a) per variable. As the next steps, I re-scale them to range from 0 to 1 based on Eq. 8 and via averaging the re-scaled mean *RMSE*, *rank* and *NSE* values I obtain the *grand-RMSE*, *-rank* and *-NSE* (Figure 3.4-2b). The 32 CMIP5 models show diverging performance in capturing past seasonal TS and PR variability (Figure 3.4-2). Some models (e.g., FGOALS-s2; MRI-CGCM3) stand out from others, suggesting that abandoning the 'one model one vote' approach (Knutti 2010) is a

right decision for the target area. Those models that performed above the 90th percentile of the CMIP5 ensemble based on any of the three metrics – a total of six models (FGOALS-s2; IPSL-CM5B-LR; MPI-ESM-LR; MRI-CGCM3; MRI-ESM1; GISS-E2-R-CC) – are selected that skillfully reproduce multidecadal TS and PR variability over the past ~150 years in East-Central Europe (Figure 3.4-2b).

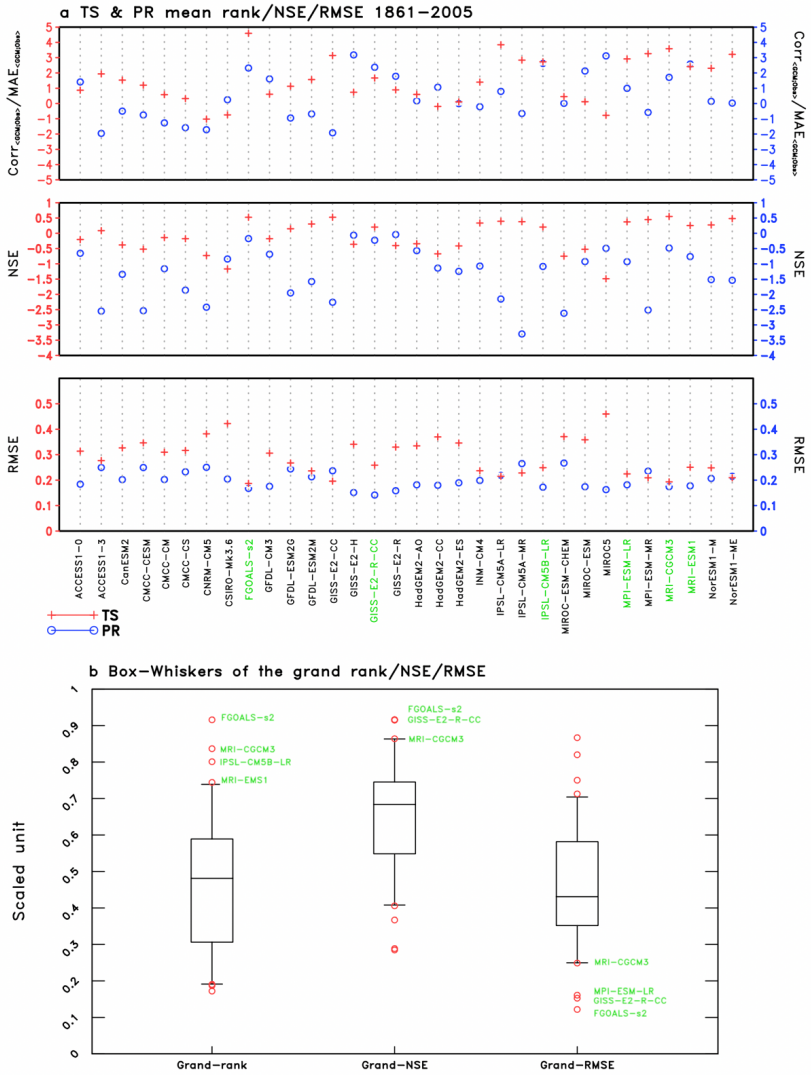

FIG. 3.4-2. Constraining past hydroclimate projections of CMIP5 models. (a) Surface temperature (*TS*) and precipitation (*PR*) mean ((JJA+DJF)/2) ranks (upper panel), mean *NSE* (middle panel) and mean *RMSE* (lower panel) for East-Central Europe for the historical era (1861-2005) across 32 CMIP5 climate models (indicated below the x-axis). (b) box-and-whiskers plot of the scaled [0;1] *grand-rank*, *grand-NSE* and *grand-RMSE* (indicated below the x-axis) showing the 10th and 90th percentiles of 32 CMIP5 model's performances. Red circles show models above 90th and below 10th percentiles, respectively. Those six models above the 90th percentile in the *grand-rank* or *-NSE* or *-RMSE* are highlighted with green on (a). *This Figure is adopted from Topál et al. (2020b).*

3.4.2 Validation of the ranking based on the NOAA 20th century reanalysis

To account for possible obscuring effects of the moderate size of the primary target area on the selection of the best performing models, I repeat the ranking using only *RMSE* for the extended domain (Figure 3.4-1) based on the NOAA 20th century version 3 gridded reanalysis (**Section 2.15**; Slivinski et al. 2019). The calculation method is equivalent to the one applied to the HISTALP records except the 32 CMIP5 models are evaluated against the gridded reanalysis product. The spatial distribution of the reanalysis-based *TS/PR mean RMSE* relative to the CMIP5 multi-model ensemble mean for the six previously selected models are shown in Figure 3.4-3. In addition, the *TS/PR mean RMSE* and the *grand-RMSE* for each model averaged over the extended target area is shown as a box-and-whiskers plot (Figure 3.4-3m). Based on the *grand-RMSE* for the extended target area only three out of the previously selected six models exhibit similar good overall performance; thus, I further reduce the range of selected models to the MRI-CGCM3, MRI-ESM1 and FGOALS-s2 and refer to them as the constrained ensemble.

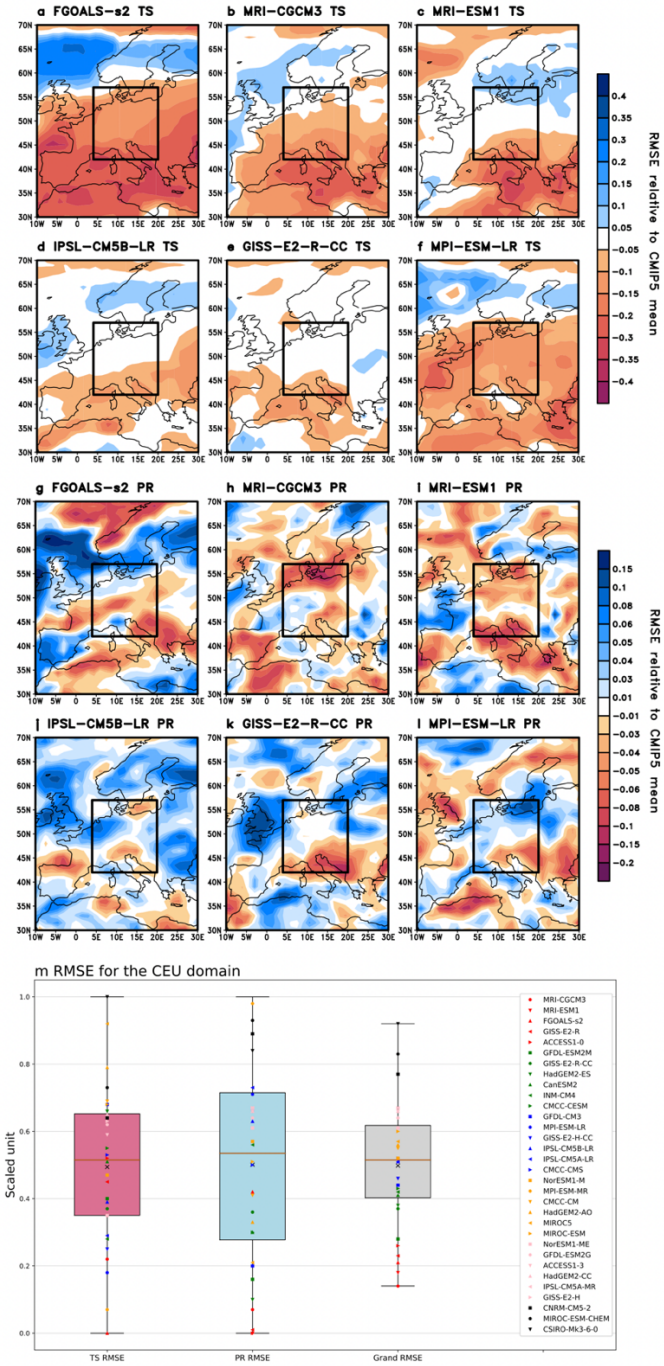

FIG. 3.4-3. Evaluation of model performance based on the NOAA 20th century reanalysis. Spatial map of (a)-(f) surface temperature (*TS*) and (g)-(l) precipitation (*PR*) *RMSE* based on the NOAA 20th century reanalysis (1861-2005) relative to the CMIP5 ensemble mean shown for the top 6 ranked models and (m) box-and-whiskers plot of the *TS* (violet) and *PR* (light blue) *RMSE* averaged for the Central European (CEU) domain (43°-57°N;4°E-20°E) and the average of the *TS* and *PR RMSE* values (*grand-RMSE* with grey) for 32 CMIP5 models each of which is marked as in the legend. The whiskers extend to the minimums and maximums. The median of each group is indicated with orange horizontal lines. The means are marked with ×. *This Figure is adopted from Topál et al. (2020b).*

3.4.3 Rank histograms to assess SMILE performance

Furthermore, since internal variability cannot be correctly assessed in a multi-model ensemble because of the initial condition problem and differences in model structures (Branstator and Teng 2010; Knutti 2010; Bódai and Tél 2012), it must be considered, that it may leave its fingerprint on the applied ranking. Hence, I study rank histograms of historical precipitation projections of the MPI-GE and EC_EARTH-LE in the primary target area (Figure 3.4.4). Both SMILEs underestimate the observed summer and winter precipitation variability (histograms are u-shaped), which is reinforced by the chi-squared tests indicating significant differences from uniformity (on the 99% confidence level). Additionally, the CMIP5 multi-model ensemble shows similar rank histograms to the SMILEs' Figure 3.4.4e-f), except that the winter rank histogram does not differ significantly from a flat one. These indicate that (i) conclusions based on simulated internal variability by these two state-of-the-art SMILEs should be treated with caution and that (ii) observational constraints may indeed be helpful in revealing models with structural advances relative to other models.

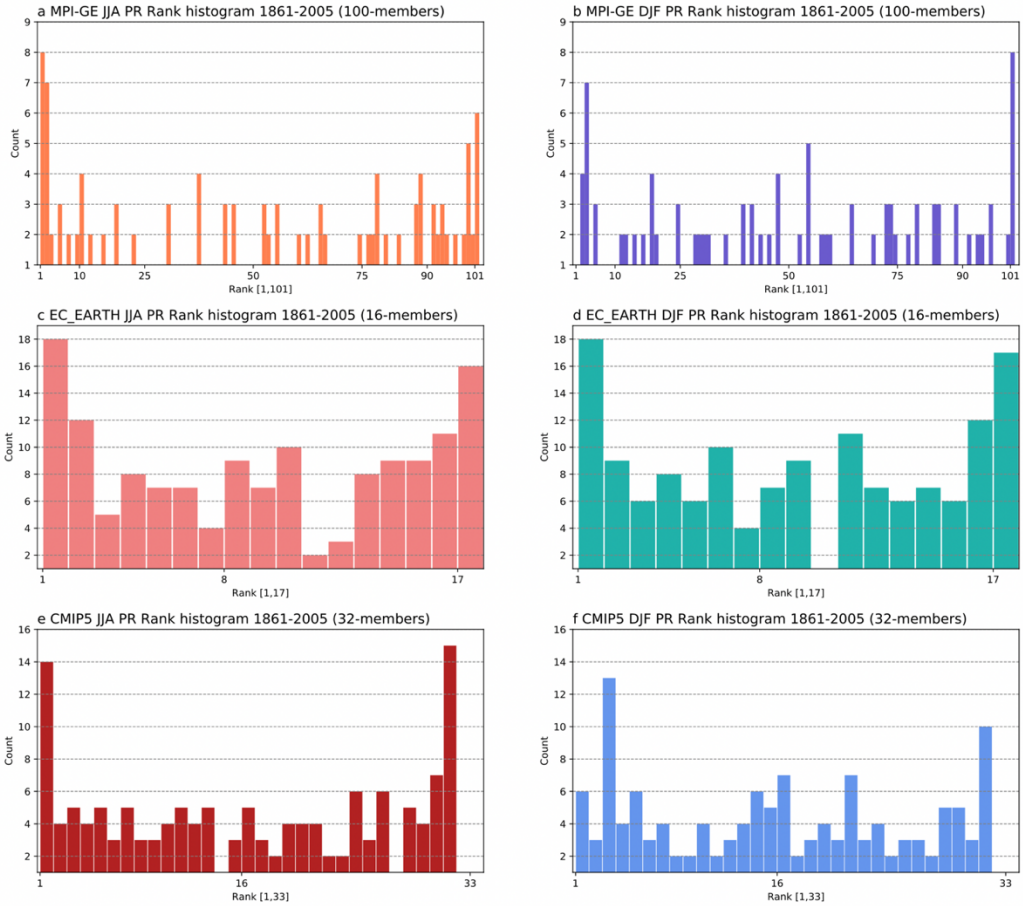

FIG. 3.4-4. Rank histograms. Evaluation of rank histograms (**Section 2.17**) based on the year-to-year seasonal mean HISTALP observed precipitation in the primary target area (43°N-50°N;13°E-19.5°E) for two large ensembles (a)-(b) MPI-GE and (c)-(d) EC_EARTH-LE, in addition to the CMIP5 multi-model ensemble (e)-(f). (a)-(e) are found to significantly differ from a flat rank histogram based on a chi-squared test ($p<0.01$). *This Figure is adopted from Topál et al. (2020b).*

3.4.4 A possible source for a reduced projection spread: land-atmosphere couplings

I am particularly concerned with how future projections of the constrained model ensemble look like in East-Central Europe. Not only did the ranking result in a reduced spread in historical simulations, but the members of the constrained ensemble also show reduced spread in their future projections relative to the CMIP5 ensemble mean for both summer (Figure 3.4.5a) and winter (Figure 3.4.5b). Moreover, the difference between the CMIP5 ensemble mean (28 models' mean: -3.9%/decade) and the constrained ensemble mean (3 models' mean: -0.1%/decade) future precipitation trend is significant based on a two-sample t-test (99% confidence level). The three top-ranked models indicate less dry

summer and wetter winter conditions in the upcoming decades not only in the primary target area, but on the extended domain as well in parallel with considerable surface temperature rise (Figure 3.4.6). Members of the constrained CMIP5 ensemble indicate -0.7 to +1 %/decade summer and +1 to +5 %/decade winter precipitation change for East-Central Europe relative to 1971-2000. Examining the constrained ensemble members' future seasonal surface temperature projections, I find no noticeable differences relative to the CMIP5 ensemble mean, therefore I rule out the possibility that the discrepancy in future precipitation projections may be due to a negative surface temperature bias in those models.

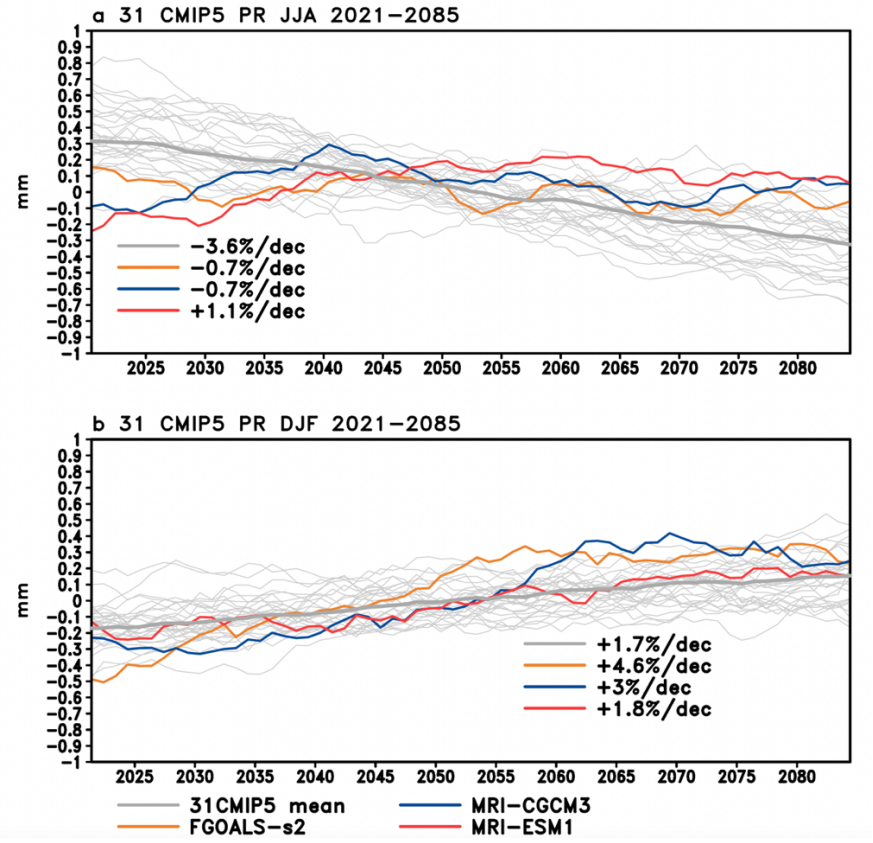

FIG. 3.4-5. Future precipitation projections of the constrained CMIP-ensemble. Time series of standardized (relative to 1971-2000 mean) seasonal mean precipitation (*PR*) for 2021-2085 (31-yr moving averaged) for the members of the constrained CMIP5 ensemble (colored solid lines) and the mean of 31 CMIP5 models (thick solid grey line) in addition to the 31 individual models in CMIP5 (thin solid grey lines) for the primary target area (43°N-50°N;13°E-19.5°E) (a) for JJA and (b) for DJF. *This Figure is adopted from Topál et al. (2020b).*

These results are partly at odds with previous expectations that project extensive summer drying in the Central European region (Feng and Fu 2013; Polade et al. 2015; Pfleiderer et al. 2019). One mechanism for the advanced summer aridification in the region has been associated with the moist lapse-rate feedback due to global warming (Brogli et al. 2019). A warmer atmosphere, deduced from Clausius-Clapeyron relation, can held more moisture, which, during moist adiabatic vertical motions, allows enhanced latent heat release and thus upper-tropospheric warming. These altogether result in an increased dry atmospheric static stability as the thermal stratification remains close to the moist adiabat during summer (Schneider 2007; Brogli et al. 2019). Another mechanism regarding changes in atmospheric circulation regimes, such as the poleward shifted subsidence zone with the projected expansion of the Hadley-cell, has also been suggested to influence future hydroclimate in the region due to enhanced radiative forcing (Perez et al. 2014; Mann et al. 2018). Nevertheless, the inconclusive literature (e.g., Kröner et al. 2017) hinders us from a complete understanding of possible future precipitation changes in transitional climatic zones, such as Central Europe.

Recent studies highlight a competing role for land-atmosphere interactions and the extent of its realistic representation in climate models in determining future hydroclimate uncertainty in the Mediterranean and Central Europe, where soil moisture largely affects temperature and precipitation via the partitioning of net radiation into sensible and latent heat fluxes (Boberg and Christensen 2012; Lorenz et al. 2016; Vogel et al. 2018; Al-Yaari et al. 2019; Selten et al. 2020). It has also been proposed that it is not enough for a model to faithfully represent observed soil-atmosphere feedbacks because convection, land-surface and cloud parametrization schemes not only influence how soil moisture-precipitation feedbacks are handled in a model, but they also affect soil moisture-temperature feedbacks in turn (Christensen and Boberg 2012). This further complicates and

highlights the importance of land-atmosphere interactions in determining future hydroclimate uncertainty in our target region.

Members of the constrained CMIP5 ensemble belong to the group of CMIP5 models that was identified by Vogel et al. (2018) with (i) more fidelity in representing land-atmosphere couplings and (ii) less pronounced summer hot and dry extremes for central Europe. A physical mechanism strongly connected to land-atmosphere feedbacks that might balance the decrease in precipitation during future transition into drought-prone regions in Central Europe was also suggested (Taylor et al. 2012a). In an early study Dai (2006) showed that a previous version of MRI-CGCM3 (the MRI-CGCM version 2.3.2a) better captured observed global rainfall patterns than other models indicating that some basic features rooted in the model physics (most likely the convective and stratiform precipitation parametrization schemes) can indeed be sources of intermodel spread.

These lines of evidence reinforce the idea of ranking to constrain future hydroclimate projections of different CMIP5 models based on evaluating their historical performance and suggest an important physical mechanism that can explain why the above-selected models perform better regionally. Furthermore, presented results provide valuable implications for future RCM simulations and advocate future research to revisit the problem of the fidelity of land-atmosphere feedbacks in RCM simulations, where the enhanced resolution allows for a more detailed picture of regional feedback mechanisms.

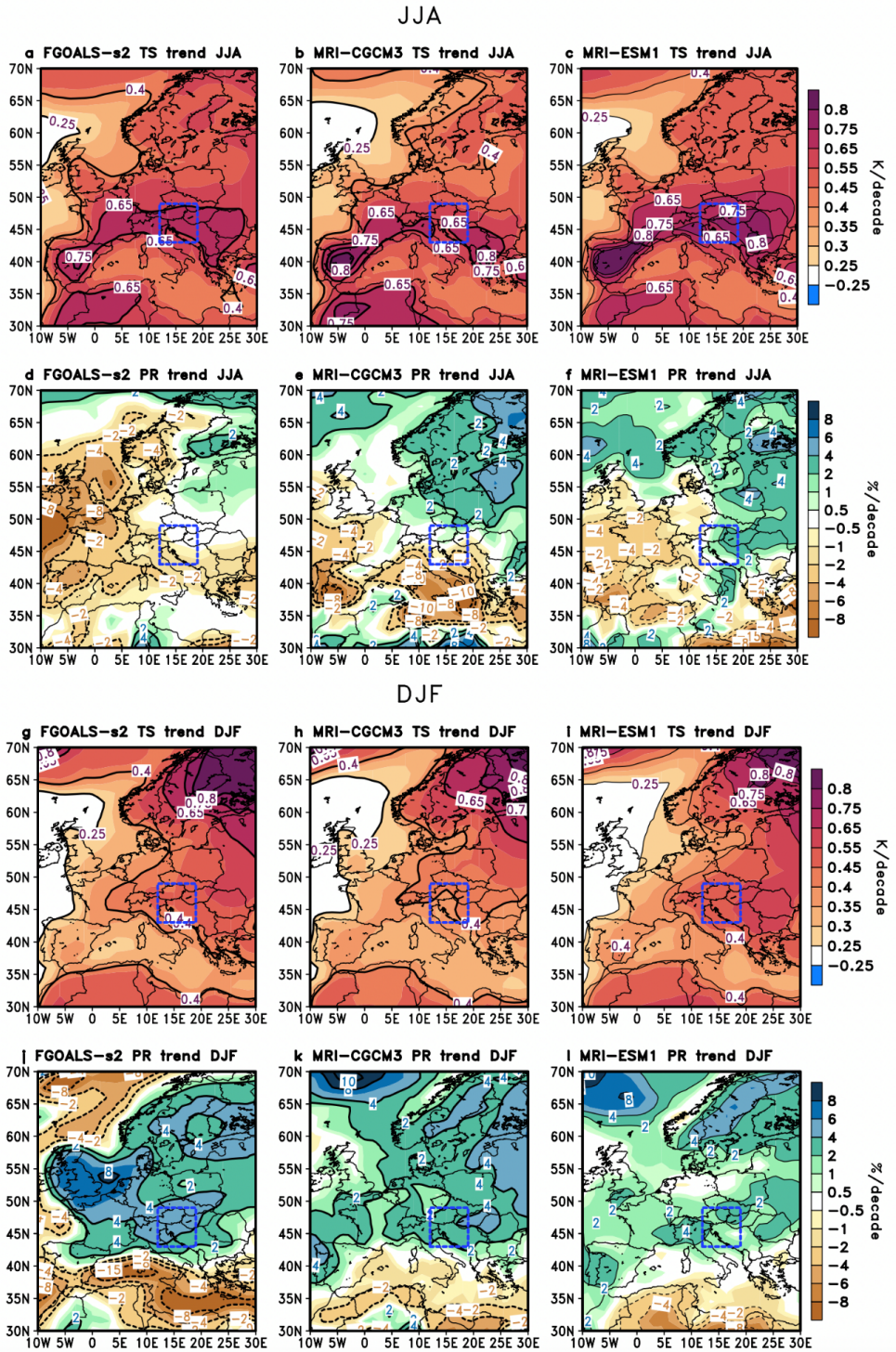

FIG. 3.4-6. Long-term (2021-2085) surface temperature and precipitation changes in the constrained CMIP5 ensemble. Spatial map of the linear trend (relative to 1971-2000 mean) of (a)-(c) & (g)-(i) surface temperature (*TS*: K/decade) and (d)-(f) & (j)-(l) precipitation (*PR*: %/decade) for 2021-2085 (31-yr moving averaged) under RCP8.5 scenario in the members of the constrained CMIP5 ensemble for JJA and DJF. *This Figure is adopted from Topál et al. (2020b).*

3.4.5 Placing future precipitation projections of the constrained ensemble in the context of SMILE projections

Based on the ranking I identified a constrained CMIP5 multi-model ensemble that shows reduced spread in their historical and future precipitation projections indicating less dry summer and wetter winter conditions in the upcoming decades. I have also discussed that land-atmosphere feedbacks may be of key importance in explaining why some models perform better than others. The advantage of including SMILE simulations here is to provide an estimate (i) for the forced response (ensemble mean) in precipitation to greenhouse gas emissions as well as (ii) for all possible states allowed by internal variability in a certain model (ensemble spread), which allows for placing the observationally constrained CMIP5 ensemble (three top-ranked models) in the context of internal variability. What is more, with the inclusion of six SMILEs, I can compare the internal variability of projected precipitation of various models, thus, get a more robust estimate of future states of hydroclimate allowed by internal variability in the region. Caveats added by the coarse spatial and topography resolution of SMILEs are also noted, however, currently it is our best estimate for projected hydroclimate uncertainty due to internal variability because of lacking SMILEs with regional climate models.

The spatial map of the ensemble mean future precipitation projections' linear trends for Europe as well as the spread across all members of the ensembles as a box-and-whiskers plot are shown in our primary target area for summer (Figure 3.4.7). In summer all SMILE mean simulations show drier future conditions in East-Central Europe indicating -2% to -7%/decade precipitation decrease during the upcoming decades relative to 1971-2000 (Figure 3.4.7), while the constrained CMIP5 ensemble mean trend indicates less pronounced summer drying (-0.1%/decade). However, the magnitudes of the ensemble mean projections as well as the ensemble spread of different SMILE simulations varies considerably across the six SMILEs, that implies a role for model uncertainty in regulating

future hydroclimate changes on top of internal variability. Furthermore, the constrained ensemble's mean future (2021-2085) precipitation trend (-0.1%/decade) emerges from the interquartile range of simulated internal variability by six SMILEs ((-8%, -1%)/decade). The difference between the group of future precipitation trends spanned by all the members of the six SMILEs (a total of 256 members) and the constrained ensemble (3 members) is significant based on a two-sample t-test on the 99% confidence level (the means of the two groups' trends: -4.8%/decade for the six SMILEs and -0.1%/decade for the constrained ensemble).

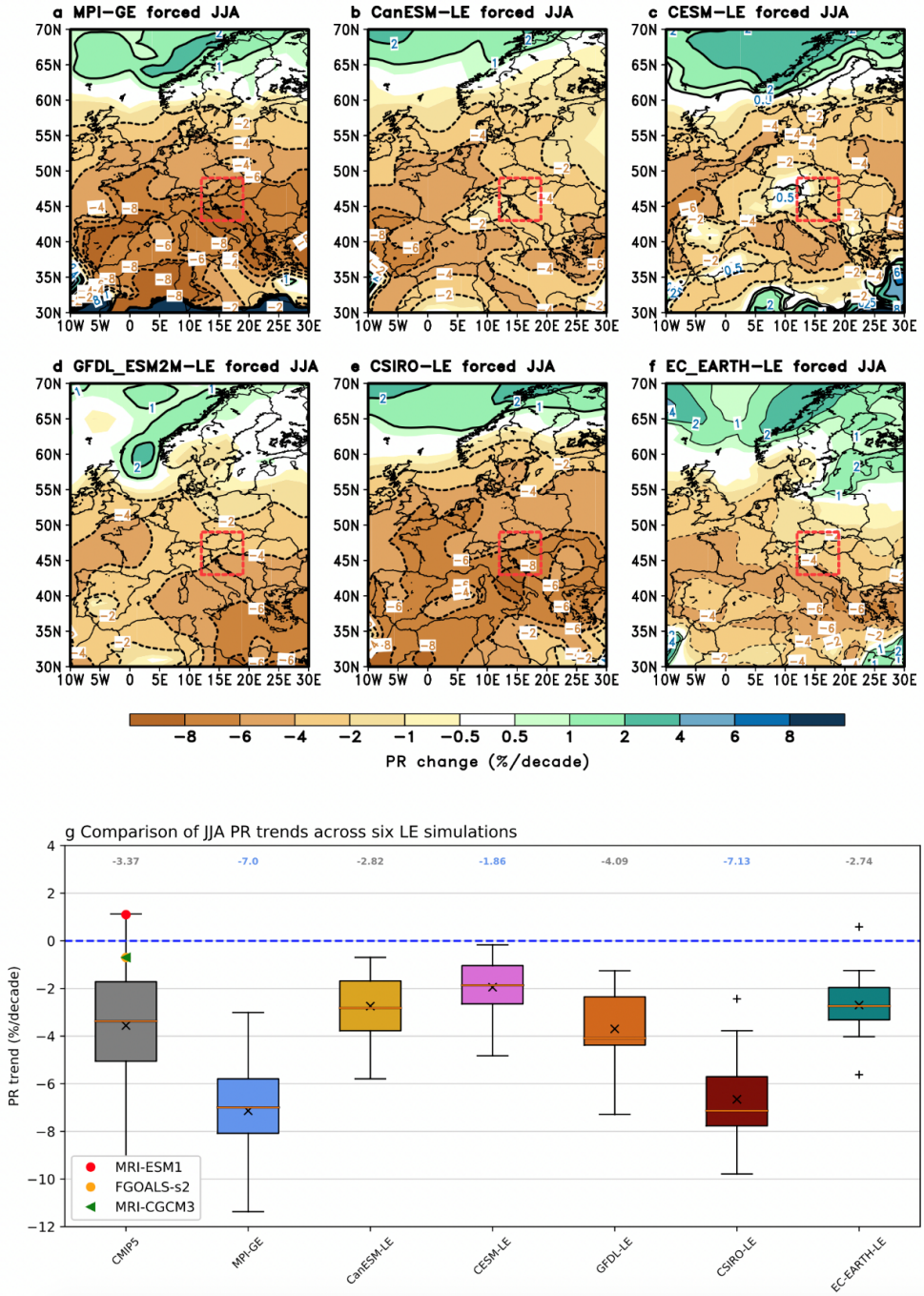

FIG. 3.4-7. Future regional precipitation changes in SMILEs. Above: (a)-(f) spatial map of the ensemble mean (forced component) linear trend (relative to 1971-2000) of summer (June-July-August: JJA) precipitation for 2021-2085 (31-yr moving averaged) for the six SMILEs. Below: (g) box-and-whiskers plot (with the whiskers extending to 1.5×interquartile range) of JJA precipitation linear trends (relative to 1971-2000) for 2021-2085 (31-yr moving averaged) for the CMIP5 multi-model and the six SMILEs (indicated below the x-axis) for the primary target area (indicated by the red rectangles on (a)-(f): 43°N-50°N;13°E-19.5°E). The median of each ensemble is indicated with numbers above the boxes in addition to the orange lines. The means are marked with ×, while the outliers (extending 1.5×interquartile range) are marked with +. Trend values of the members of the constrained CMIP5 ensemble are indicated with markers on the first box-and-whiskers. *This Figure is adopted from Topál et al. (2020b).*

Since observations were used to constrain the CMIP5 ensemble, which resulted in the selection of models with more realistic representations of land-atmosphere feedbacks, *I suggest that the difference between the constrained ensemble's and the six SMILEs' future summer precipitation trends may be attributable to land-atmosphere coupling discrepancies between the models.* Importantly, except for the CESM1, the base models of the large ensemble simulations were either involved in the ranking, or I evaluated their historical simulations. Thus, it is unlikely that the SMILE simulations would regionally outperform the members of the constrained CMIP5 ensemble in capturing observed precipitation variability. Although, this needs further efforts to clarify, these lines of evidence suggest less extreme summer drying in East-Central Europe and that land-atmosphere coupling may play a key role in regulating future summer hydroclimate uncertainty in line with several recent studies (Boberg and Christensen 2012; Vogel et al. 2018; Selten et al. 2020).

These results suggest an important role for land-atmosphere coupling differences among climate models in regulating future summer hydroclimate uncertainty on top of the irreducible internal variability and calls for caution when interpreting future summer precipitation projections of the state-of-the-art SMILE simulations. I urge coordinated efforts to further quantify the relative contribution of internal variability and model structural differences in regulating future seasonal hydroclimate uncertainty in Central Europe by e.g., running SMILEs with regional climate models or downscaling existing SMILEs for our region.

4 SUMMARY and THESES

In this dissertation I have addressed four main topics, involving five aims ($\mathbf{A_1}$ to $\mathbf{A_5}$). As for $\mathbf{A_1}$ I have shown that **$\mathbf{T_1}$: an atmospheric process, partially originating from internal variability, is a significant contributor to sea-ice changes not only in the past decades, but also under future emissions scenarios. Nonetheless, important model limitations were also highlighted, which yet obstructs the attribution of Arctic sea-ice changes to internal versus forced origins.**

Making use of the wind-nudging framework ($\mathbf{A_2}$ and $\mathbf{A_3}$), however, I have shown example how to circumvent the model biases and quantified the wind-driven response of GrIS melting with implications to global sea-level rise. **$\mathbf{T_2}$: A substantial portion, –71.7 Gt yr^{-1} decade^{-1} (out of the –132.8 Gt yr^{-1} decade^{-1}) total ice mass change equaling ~0.2 mm yr^{-1} decade^{-1} sea-level rise acceleration relates to wind-induced adiabatic warming between 1990 and 2012, which holds potential for atmospheric circulation to affect the rate of sea-level rise to a similar extent in the coming decades.**

$\mathbf{T_3}$: Paleoclimatic evidence reinforces that the significant enhancement of GrIS melting between 1990 and 2012 and associated acceleration in the rate of sea-level rise have been a manifestation of low-frequency variability in the climate system, arising from decadal tropical SST variability.

Lessons learnt from the nudging experiments lead to the next steps to actually interpret the model issues in terms of the transient climate sensitivity ($\mathbf{A_4}$). The misrepresented sensitivity of Arctic sea-ice and the GrIS to large-scale winds in climate models prioritizes a need to refocus model evaluation efforts from expecting the models to match observed surface warming rates in their forced responses and instead assess model skill in simulating the observed sensitivity to overlying circulation changes.

T_4: The global mean temperature response to CO_2 forcing seems insufficient to scale the Arctic climate response. The models' low sensitivity to atmospheric forcing (compared with observations) can result in too strong Arctic warming- and a high sea- and land-ice sensitivity to anthropogenic forcing if the priority criteria to evaluate model performance is based on matching the simulations with observations.

We have also seen that the main difference between the modelled and observed RCS_A is that **T_5: the models' forced responses do not favour a low frequency change in the rotational component of Arctic winds since under global warming scenarios they exhibit rather horizontally uniform SST response in the tropics. Hence the main source to create strong rotational winds in the high latitudes through Rossby-wave dispersion is obstructed.**

Accounting for this discrepancy I find that **T_6: the likely probability of a seasonally ice-free Arctic and widespread GrIS melting is delayed by 9–15 years, and it is not likely to see an ice-free summer before 2050.**

Hence, improved simulation of the Arctic's observed sensitivity to large-scale atmospheric circulation-driven changes in climate models may provide a means of significantly improving predictions of the GrIS's future contribution to global environmental crises, including freshwater discharge into the Atlantic Ocean that may influence the recently observed AMOC slow-down (Rahmstorf et al. 2015; Caesar et al. 2021), global sea level rise (Briner et al. 2020; Slater et al. 2020; Frederikse et al. 2020) and toxic mercury transport to the global oceans (Hawkings et al. 2020). The local atmospheric circulation bias may also be linked to model limitations in simulating tropical-Arctic teleconnections and their sensitivity to low frequency tropical SST variability and/or high-latitude sea-ice-ocean-atmosphere interactions (*Topál et al. 2020a*; Luo et al. 2021), which, according to previous studies (Ding and Wang 2005; Ding et al. 2011), could arise

from biases in simulating low-frequency SST and rainfall variability over the tropical eastern Pacific and the climatological mean flow over the North Pacific.

If the Arctic climate system in current climate models is indeed insufficiently and exaggeratedly sensitive to CO_2, then future research will need to identify the processes and physics in models that contribute to the biased sensitivity. The above results in **Section 3.3.** suggest a delay in the time of emergence of an ice-free Arctic, which may be a silver linen. Nevertheless, regarding preserving the Arctic's local cryosphere, a better understanding is called for the 'too hot' issue (Hausfater et al. 2022) through quantifying the role of observed large-scale circulation in explaining warming particular regions of the planet over the past decades. This new perspective may move us closer to understand why some CMIP6 models have become more sensitive to greenhouse effects (Zelinka et al. 2020). In summary, the evaluation of models' ability to represent the *ASI/GSI* may need to precede the assessment or recalibration of models' Arctic sea- or land-ice projections based on their simulation of the global mean temperature response to CO_2 forcing.

Regarding $\mathbf{A_5}$, unfortunately, those models identified in **Section 3.4** are currently not being used to force regional climate model (RCM) simulations in East Central Europe, which may lead to spurious projections of future drying in our region and false attribution of internal variability driven changes to a forced hydroclimate response. **T_7: My results suggest that the difference between the constrained ensemble's and the six SMILEs' future summer precipitation trends may be attributable to land-atmosphere coupling discrepancies between the models. Physical differences between models thus plays an important role in regulating future summer hydroclimate uncertainty and calls for caution when interpreting future summer precipitation projections of the state-of-the-art SMILE simulations.**

Hence, I advocate for the need to systematically consider internal variability as a separate form of model projection uncertainty on top of model structural uncertainties that arise from the differences in the models' physical settings. This separation is only possible with downscaling SMILEs made with global climate models (see e.g., Wood and Ludwig 2020), however this approach so far has been overlooked by national climate policymakers. This approach should be a high-priority next step in coordinated national policymaking with implications to agricultural adaptation planning.

5 REFERENCES

Ablain, M et al. (2019) Uncertainty in satellite estimate of global mean sea level changes, trend and acceleration. *Earth Syst. Sci. Data*. **2**, 1-26. https://doi.org/10.5194/essd-11-1189-2019

Ahmed K, Sachindra DA et al. (2019) Selection of multi-model ensemble of general circulation models for the simulation of precipitation and maximum and minimum temperature based on spatial assessment metrics. *Hydrol. Earth. Syst. Sci.* **23**(11), 4803-4824. https://doi.org/10.5194/hess-23-4803-2019

Al-Yaari, A, Ducharne, A, Cheruy, F et al. (2019) Satellite-based soil moisture provides missing link between summertime precipitation and surface temperature biases in CMIP5 simulations over conterminous United States. *Sci. Rep.* **9**(1657). https://doi.org/10.1038/s41598-018-38309-5

Amory, C et al. (2015) Comparison between observed and simulated aeolian snow mass fluxes in Adélie Land, East Antarctica. *Cryosphere* **9**, 1373-1383. https://doi.org/10.5194/tc-9-1373-2015

Annan, JD, Hargreaves, JC (2010) Reliability of the CMIP3 ensemble. *Geophys. Res. Lett.* **37**, L02703. https://doi.org/10.1029/2009GL041994

Auer, I, Böhm, R, Jurkovic, A et al (2007) HISTALP—historical instrumental climatological surface time series of the Greater Alpine Region. *Int. J. Climatol.* **27,** 17-46. https://doi.org/10.1002/joc.1377

Ballinger, TJ et al. (2018a) Anomalous blocking over Greenland preceded the 2013 extreme early melt of local sea ice. *Ann. Glaciol*. **59**, 81-190. https://doi.org/10.1017/aog.2017.30

Ballinger, TJ et al. (2018b) Greenland coastal air temperatures linked to Baffin Bay and Greenland Sea ice conditions during autumn through regional blocking patterns. *Clim. Dyn.* **50**, 83-100. https://doi.org/10.1007/s00382-017-3583-3

Ballinger, TJ et al. (2021) The role of blocking circulation and emerging open water feedbacks on Greenland cold-season air temperature variability over the last century. *Int. J. Climatol.* **41,** E2778-E2800. https://doi.org/10.1002/joc.6879

Barnes, EA, Polvani, LM (2015) CMIP5 Projections of Arctic Amplification, of the North American/North Atlantic Circulation, and of Their Relationship. *J. Clim.* **28**(13), 5254-5271. https://doi.org/10.1175/JCLI-D-14-00589.1

Bartholy, J, Pongrácz, R (2007) Regional analysis of extreme temperature and precipitation indices for the Carpathian Basin from 1946 to 2001. *Glob. Planet. Change.* **57**(1-2), 83-95. https://doi.org/10.1016/j.gloplacha.2006.11.002

Baxter, I, Ding, Q, Schweiger, A et al. (2019) How tropical Pacific surface cooling contributed to accelerated sea ice melt from 2007 to 2012 as ice is thinned by anthropogenic forcing. *J. Clim.* **32**(24), 8583-8602. https://doi.org/10.1175/JCLI-D-18-0783.1

Baxter, I, Ding, Q (2022) An optimal atmospheric circulation mode in the Arctic favoring strong summertime sea ice melting and ice-albedo feedback. *J. Clim.* **35**(20), 3027-3045. https://doi.org/10.1175/JCLI-D-21-0679.1

Beniston, M, Stephenson, DB, Christensen, OB et al (2007) Future extreme events in European climate: an exploration of regional climate model projections. *Clim. Change.* **37**, 71-95. https://doi.org/10.1007/s10584-006-9226-z

Bennartz, R et al. (2013) 2012 July Greenland melt extent enhanced by low-level liquid clouds. *Nature* **496**, 83-86. https://doi.org/10.1038/nature12002

Berg, A, Findell, K, Lintner, B et al (2016) Land–atmosphere feedbacks amplify aridity increase over land under global warming. *Nat. Clim. Change.* **6**, 869-874. https://doi.org/10.1038/nclimate3029

Bevis, M et al. (2019) Accelerating changes in ice mass within Greenland, and the ice sheet's sensitivity to atmospheric forcing. *Proc. Natl. Acad. Sci. USA* **116**, 1934-1939. https://doi.org/10.1073/pnas.1806562116

Boberg, F, Christensen, JH (2012) Overestimation of Mediterranean summer temperature projections due to model deficiencies. *Nat. Clim. Change.* **2**, 433-436. https://doi.org/10.1038/nclimate1454

Bódai, T, Drótos, G, Herein, M et al. (2020) The forced response of the El Niño–Southern Oscillation–Indian monsoon teleconnection in ensembles of earth system models. *J. Clim.* **33**(6), 2163-2182. https://doi.org/10.1175/JCLI-D-19-0341.1

Bódai, T, Tél, T (2012) Annual variability in a conceptual climate model: Snapshot attractors, hysteresis in extreme events, and climate sensitivity. *Chaos* **22**, 023110. https://doi.org/10.1063/1.3697984

Boening, C, Willis, JK, Landerer, FW, Nerem, RS Fasullo, J (2012) The 2011 La Niña: so strong, the oceans fell. *Geophys. Res. Lett.* **39**, L19602. https://doi.org/10.1029/2012GL053055

Boer, GJ, Lambert, SJ (2001) Second-order space-time climate difference statistics. *Clim. Dyn.* **17**, 213-218. https://doi.org/10.1007/PL00013735

Boers, N, Rypdal, M (2021) Critical slowing down suggests that the western Greenland Ice Sheet is close to a tipping point. *Proc. Natl Acad. Sci. USA* **118**, e2024192118. https://doi.org/10.1073/pnas.2024192118

Bonan, DB, Blanchard-Wrigglesworth, E (2020). Nonstationary teleconnection between the Pacific Ocean and Arctic sea ice. *Geophys. Res. Lett.,* **47**, e2019GL085666. https://doi.org/10.1029/2019GL085666

Bonan, DB, Lehner, F, Holland, MM (2021) Partitioning uncertainty in projections of Arctic sea ice. *Environ. Res. Lett.* **16**, 044002. https://doi.org/10.1088/1748-9326/abe0ec

Bonan, DB, Schneider, T, Eisenman, I, Wills, RCJ (2021) Constraining the Date of a Seasonally Ice-Free Arctic Using a Simple Model, *Geophys. Res. Lett.* **48**(18), e2021GL094309. https://doi.org/10.1029/2021GL094309

Brands, S, Herrera, S, Fernández, J et al (2013) How well do CMIP5 Earth System Models simulate present climate conditions in Europe and Africa? *Clim. Dyn.* **41**, 803-817. https://doi.org/10.1007/s00382-013-1742-8

Branstator, G, Teng, H (2010) Two limits of initial-value decadal predictability in a CGCM. *J. Clim.* **23**(23), 6292-6311. https://doi.org/10.1175/2010JCLI3678.1

Bretherton, CS, Smith, C, Wallace, JM (1992) An intercomparison of methods for finding coupled patterns in climate data. *J Clim*, **5**, 541-560. https://doi.org/10.1175/1520-0442(1992)005<0541:AIOMFF>2.0.CO;2

Briner, JP et al. (2020) Rate of mass loss from the Greenland Ice Sheet will exceed Holocene values this century. *Nature* **586**, 70-74. https://doi.org/10.1038/s41586-020-2742-6

Brogli, R, Kröner, N, Sørland, SL et al (2019) The role of Hadley circulation and lapse-rate changes for the future European summer climate. *J. Clim.* **32**(2), 385-404. https://doi.org/10.1175/JCLI-D-18-0431.1

Caesar, L et al. Current Atlantic Meridional Overturning Circulation weakest in last millennium. *Nat. Geosci.* **14**, 118–120 (2021). https://doi.org/10.1038/s41561-021-00699-z

Castruccio, FS, Ruprich-Robert, Y, Yeager, SG, Danabasoglu, G, Msadek, R, Delworth, T (2019) Modulation of Arctic Sea Ice Loss by Atmospheric Teleconnections from Atlantic Multidecadal Variability. *J Clim*, **32**, 1419-1441. https://doi.org/10.1175/JCLI-D-20-0330.1

Cavalieri, DJ, Parkinson, CL, Gloersen, P, Zwally, HJ (1996) Sea ice concentrations from Nimbus-7 SMMR and DMSP SSM/I-SSMIS passive microwave data, version 1. Subset used: V3-NH, NASA, National Snow and Ice Data Center Distributed Active Archive Center, accessed 29 April 2018, https://doi.org/10.5067/8GQ8LZQVL0VL

Chen, X et al. (2017) The increasing rate of global mean sea-level rise during 1993–2014. *Nat. Clim Chang.* **7**, 492-495. https://doi.org/10.1038/nclimate3325

Cheruy, F, Dufresne, JL, Hourdin, F, Ducharne, A (2014) Role of clouds and land-atmosphere coupling in midlatitude continental summer warm biases and climate change amplification in CMIP5 simulations. *Geophys. Res. Lett.* **41,** 6493-6500. https://doi.org/10.1002/2014GL061145

Christensen, JH, Boberg F (2012) Temperature dependent climate projection deficiencies in CMIP5 models. *Geophys. Res. Lett.* **39**, L24705. https://doi.org/10.1029/2012GL053650

Chylek, P, Folland, C, Klett, JD, Wang, M, Hengartner, N, Lesins, G, Dubey, MK (2022) Annual Mean Arctic Amplification 1970–2020: Observed and Simulated by CMIP6 Climate Models, *Geophys. Res. Lett.* **49**(13) e2022GL099371. https://doi.org/10.1029/2022GL099371

Chylek, P, Folland, CK, Lesins, G., Dubey, MK, Wang, M, (2009) Arctic air temperature change amplification and the Atlantic Multidecadal Oscillation, *Geophys. Res. Lett.* **36**, L14801 https://doi.org/10.1029/2009GL038777

Cohen, J, et al. (2014) Recent Arctic amplification and extreme mid-latitude weather. *Nat. Geosci*. **7**, 627-637. https://doi.org/10.1038/ngeo2234

Compo, GP, Whitaker, JS, Sardeshmukh, PD et al (2011) The twentieth century reanalysis project. *Q. J. R. Meteorol. Soc.* **137**, 1-28. https://doi.org/10.1002/qj.776

Coppola, E, Giorgi, F, Rauscher, SA, et al (2010) Model weighting based on mesoscale structures in precipitation and temperature in an ensemble of regional climate models. *Clim. Res.* **44**, 121-134. https://doi.org/10.3354/cr00940

Dai, A (2006) Precipitation Characteristics in Eighteen Coupled Climate Models. *J. Clim.* **19**(18), 4605-4630. https://doi.org/10.1175/JCLI3884.1

Dai, A, Fyfe, J, Xie, S et al (2015) Decadal modulation of global surface temperature by internal climate variability. *Nat. Clim. Change.* **5**, 555-559. https://doi.org/10.1038/nclimate2605

Dai, A, Luo, D, Song, M, Liu, J (2019) Arctic amplification is caused by sea-ice loss under increasing CO_2. *Nat. Commun.* **10**, 121. https://doi.org/10.1038/s41467-018-07954-9

Day, JJ, Hargreaves, JC, Annan, JD, Abe-Ouchi, A (2012): Sources of multi-decadal variability in Arctic sea ice extent. *Environ. Res. Lett.,* **7**, 034011. https://doi.org/10.1088/1748-9326/7/3/034011

Delhasse, A, Hanna, E, Kittel, C, Fettweis, X (2021) Brief communication: CMIP6 does not suggest any atmospheric blocking increase in summer over Greenland by 2100. *Int. J. Climatol*. **41,** 2589-2596. https://doi.org/10.1002/joc.6977

Delhasse, A et al (2020) Brief communication: Evaluation of the near-surface climate in ERA5 over the Greenland Ice Sheet. *Cryosphere* **14**, 957-965. https://doi.org/10.5194/tc-14-957-2020

Delhasse, A, Fettweis, X, Kittel, C, Amory, C, Agosta, C (2018) Brief communication: Impact of the recent atmospheric circulation change in summer on the future surface mass balance of the Greenland Ice Sheet. *Cryosphere* **12**, 3409–3418. https://doi.org/10.5194/tc-12-3409-2018

DeRepentigny, P, Jahn, A, Holland, MM, Kay, JE. Fasullo, J et al (2022) Enhanced simulated early 21st century Arctic sea ice loss due to CMIP6 biomass burning emissions. *Sci. Adv.* **8**(30), eabo2405 https://doi.org/10.1126/sciadv.abo2405

Deser, C, Lehner, F, Rodgers, KB et al (2020) Insights from Earth system model initial-condition large ensembles and future prospects. *Nat. Clim. Change.* **10**, 277–286. https://doi.org/10.1038/s41558-020-0731-2

Deser, C, Phillips, A, Bourdette, V et al. (2012) Uncertainty in climate change projections: The role of internal variability. *Clim. Dyn.* **38**, 527-546. https://doi.org/10.1007/s00382-010-0977-x

Deser, C, Tomas, RA, Sun, L, (2015) The Role of Ocean–Atmosphere Coupling in the Zonal-Mean Atmospheric Response to Arctic Sea ice Loss. *J Clim*. **28**, 2168-2186. https://doi.org/10.1175/JCLI-D-14-00325.1

Deser, C, Tomas, R, Alexander, M, Lawrence, D, (2010) The Seasonal Atmospheric Response to Projected Arctic Sea ice Loss in the Late Twenty-First Century. *J. Clim*. **23**, 333-351. https://doi.org/10.1175/2009JCLI3053.1

Ding, Q, Schweiger, A, L'Heureux, M et al (2019) Fingerprints of internal drivers of Arctic sea ice loss in observations and model simulations. *Nat. Geosci.* **12**, 28-33. https://doi.org/10.1038/s41561-018-0256-8

Ding, Q, Wallace, JM, Battisti, DS et al (2014) Tropical forcing of the recent rapid Arctic warming in northeastern Canada and Greenland. *Nature* **509**, 209-212. https://doi.org/10.1038/nature13260

Ding, Q et al. (2017) Influence of high-latitude atmospheric circulation changes on summertime Arctic sea ice. *Nat. Clim. Chang.* **7**, 289-295. https://doi.org/10.1038/nclimate3241

Ding, Q, Wang, B (2005) Circumglobal Teleconnection in the Northern Hemisphere Summer. *J. Clim.* **18**(17), 3483-3505. https://doi.org/10.1175/JCLI3473.1

Ding, Q, Wang, B, Wallace, JM, Branstator, G (2011) Tropical–Extratropical Teleconnections in Boreal Summer: Observed Interannual Variability. *J. Clim*. **24(7)**, 1878-1896. https://doi.org/10.1175/2011JCLI3621.1

Dong, Y, Proistosescu, C, Armour, KC, Battisti, DS (2019) Attributing Historical and Future Evolution of Radiative Feedbacks to Regional Warming Patterns using a Green's Function Approach: The Preeminence of the Western Pacific. *J. Clim*. **32**, 5471-549. https://doi.org/10.1175/JCLI-D-18-0843.1

Drótos, G, Bódai, T, Tél, T (2015) Probabilistic Concepts in a Changing Climate: A Snapshot Attractor Picture. *J. Clim*. **28**(8), 3275-3288. https://doi.org/10.1175/JCLI-D-14-00459.1

Drótos, G, Bódai, T, Tél, T (2016) Quantifying nonergodicity in nonautonomous dissipative dynamical systems: An application to climate change. *Phys. Rev. E.* **94,** 022214. https://doi.org/10.1103/PhysRevE.94.022214

Drótos, G, Bódai, T, Tél, T (2017) On the importance of the convergence to climate attractors. *Eur. Phys. J. Spec. Top.* **226**, 2031-2038. https://doi.org/10.1140/epjst/e2017-70045-7

Dyer, E, Washington, R, Teferi, TM, (2019) Evaluating the CMIP5 ensemble in Ethiopia: Creating a reduced ensemble for rainfall and temperature in Northwest Ethiopia and the Awash basin. *Int. J. Climatol.* **40**, 2964-2985. https://doi.org/10.1002/joc.6377

England, M, Jahn, A, Polvani L (2019) Nonuniform Contribution of Internal Variability to Recent Arctic Sea Ice Loss. *J. Clim.* **32**, 4039-4053. https://doi.org/10.1175/JCLI-D-18-0864.1

Fasullo, JT et al. (2022) Spurious Late Historical-Era Warming in CESM2 Driven by Prescribed Biomass Burning Emissions *Geophys. Res. Lett.* **49**(2) e2021GL097420. https://doi.org/10.1029/2021GL097420

Feng, S, Fu, Q (2013) Expansion of global drylands under a warming climate. *Atmos. Chem. Phys.* **13**, 10081-10094. https://doi.org/10.5194/acp-13-10081-2013

Fettweis, X et al (2013) Brief communication: Important role of the mid-tropospheric atmospheric circulation in the recent surface melt increase over the Greenland ice sheet. *Cryosphere* **7**, 241-248. https://doi.org/10.5194/tc-7-241-2013

Fettweis, X et al. (2020) GrSMBMIP: Intercomparison of the modelled 1980–2012 surface mass balance over the Greenland Ice Sheet. *Cryosphere* **14**(11**)**, 3935-3958. https://doi.org/10.5194/tc-14-3935-2020

Fettweis, X et al. (2017) Reconstructions of the 1900–2015 Greenland ice sheet surface mass balance using the regional climate MAR model. *Cryosphere* **11**, 1015-1033. https://doi.org/10.5194/tc-11-1015-2017

Fettweis, X, Tedesco, M, van den Broeke, M, Ettema, J (2011) Melting trends over the Greenland ice sheet (1958–2009) from spaceborne microwave data and regional climate models. *Cryosphere* **5**, 359-375. https://doi.org/10.5194/tc-5-359-2011

Fischer, EM, Schär, C (2009) Future changes in daily summer temperature variability: driving processes and role for temperature extremes. *Clim. Dyn.* **33**, 917. https://doi.org/10.1007/s00382-008-0473-8

Francis, JA, Wu, B (2020) Why has no new record-minimum Arctic sea-ice extent occurred since September 2012? *Environ. Res. Lett.* **15** 114034. https://doi.org/10.1088/1748-9326/abc047

Frederikse, T et al (2020) The causes of sea-level rise since 1900. Nature 584, 393-397. https://doi.org/10.1038/s41586-020-2591-3

Fyfe, J, Gillett, N, Zwiers, F (2013) Overestimated global warming over the past 20 years. *Nat. Clim. Chang.* **3,** 767-769. https://doi.org/10.1038/nclimate1972

Fyfe, J, Gillett, N (2014) Recent observed and simulated warming. *Nat. Clim. Chang.* **4**, 150-151. https://doi.org/10.1038/nclimate2111

Gallée, HJ, (1997) Air-sea interactions over Terra Nova Bay during winter: Simulation with a coupled atmosphere-polynya model. *J Geophys. Res*. **102**, 13835-13849. https://doi.org/10.1029/96JD03098

Gallée, H, Schayes, G (1994) Development of a three-dimensional meso-γ primitive equation model: Katabatic winds simulation in the area of Terra Nova Bay, Antarctica. *Mon. Weather Rev*., **122**, 671-685. https://doi.org/10.1175/1520-0493(1994)122<0671:DOATDM>2.0.CO;2

Garfinkel, CI, Adam, O, Morin, E et al (2020) The role of zonally averaged climate change in contributing to intermodel spread in CMIP5 predicted local precipitation changes. *J. Clim.* **33**(3), 1141-1154. https://doi.org/10.1175/JCLI-D-19-0232.1

Gautam, J, Mascaro, G (2018) Evaluation of Coupled Model Intercomparison Project Phase 5 historical simulations in the Colorado River basin. *Int. J. Climatol*. **38**, 3861-3877. https://doi.org/10.1002/joc.5540

Gleckler, PJ, Taylor, KE, Doutriaux, C, (2008) Performance metrics for climate models. *J. Geophys. Res.* **113**, D06104. https://doi.org/10.1029/2007JD008972

Goosse, H, Kay, JE, Armour, KC et al (2018) Quantifying climate feedbacks in polar regions. Nat. Commun. 9, 1919. https://doi.org/10.1038/s41467-018-04173-0

Grunseich, G, Wang, B (2016) Arctic Sea Ice Patterns Driven by the Asian Summer Monsoon. *J. Clim.* **29**, 9097-9112. https://doi.org/10.1175/JCLI-D-16-0207.1

Hahn, LC, Armour, KC, Zelinka, MD, Bitz, CM, Donohoe, A (2021) Contributions to polar amplification in CMIP5 and CMIP6 models. *Front. Earth Sci.* **9**, 1-17. https://doi.org/10.3389/feart.2021.710036

Hahn, L, Ummenhofer, CC, Kwon, YO (2018) North Atlantic natural variability modulates emergence of widespread Greenland melt in a warming climate. *Geophys. Res. Lett.* **45**, 9171-9178. https://doi.org/10.1029/2018GL079682

Hall, A, Cox, P, Huntingford, C et al. (2019) Progressing emergent constraints on future climate change. *Nat. Clim. Chang.* **9,** 269-278. https://doi.org/10.1038/s41558-019-0436-6.

Hamlington, BD et al. (2019) The dominant global modes of recent internal sea level variability. *J Geophys Res. Oceans.* **124**, 2750-2768. https://doi.org/10.1029/2018JC014635

Han, W, et al. (2014) Intensification of decadal and multi-decadal sea level variability in the western tropical Pacific during recent decades. *Clim. Dyn* **43**, 1357-1379. https://doi.org/10.1007/s00382-013-1951-1

Hanna E et al. (2018) Greenland blocking index daily series 1851–2015: Analysis of changes in extremes and links with North Atlantic and UK climate variability and change, *Int. J. Climatol.* **38(9),** 3546-3564. https://doi.org/10.1002/joc.5516

Hanna, E et al. (2021) Greenland surface air temperature changes from 1981 to 2019 and implications for ice-sheet melt and mass-balance change. *Int. J. Climatol*. **41,** E1336-E1352. https://doi.org/10.1002/joc.6771

Hanna, E et al. (2020) Mass balace of the ice sheets and glaciers – progress since AR5 and challenges, *Earth Sci Reviews* **201**, 102976. https://doi.org/10.1016/j.earscirev.2019.102976

Hanna, E, Cropper, TE, Hall, RJ, Cappelen, J (2016) Greenland blocking index 1851–2015: a regional climate change signal. *Int. J. Climatol*. **36**, 4847-4861. https://doi.org/10.1002/joc.4673

Hanna, E et al. (2013) The influence of North Atlantic atmospheric and oceanic forcing effects on 1900–2010 Greenland summer climate and ice melt/runoff. *Int. J. Climatol*. **33(4)**, 862-880. https://doi.org/10.1002/joc.3475

Hanna, E, Fettweis, X, Hall, RJ (2018) Brief communication: Recent changes in summer Greenland blocking captured by none of the CMIP5 models. *Cryosphere* **12**, 3287-3292. https://doi.org/10.5194/tc-12-3287-2018

Harrison SP, Bartlein PJ, Izumi K, et al. (2015) Evaluation of CMIP5 palaeo-simulations to improve climate projections. Nat. Clim. Chang. 5, 735-743. https://doi.org/10.1038/nclimate2649

Haszpra, T, Herein, M, (2019) Ensemble-based analysis of the pollutant spreading intensity induced by climate change. *Sci. Rep.* **9**, 3896. https://doi.org/10.1038/s41598-019-40451-7

Haszpra, T, Herein, M, Bódai, T (2020a) Investigating ENSO and its teleconnections under climate change in an ensemble view – a new perspective. *Earth. Syst. Dynam.* **11**, 267–280. https://doi.org/10.5194/esd-11-267-2020

Haszpra, T, Topál, D, Herein, M (2020b) On the time evolution of the Arctic Oscillation and related wintertime phenomena under different forcing scenarios in an ensemble approach. *J. Clim.* **33**(8), 3107-3124. https://doi.org/10.1175/JCLI-D-19-0004.1

Hatvani, IG, Topál, D, Ruggieri, E, Kern, Z (2022) Concurrent Changepoints in Greenland Ice Core δ18O Records and the North Atlantic Oscillation over the Past Millennium. *Atmosphere* **13,** 93. https://doi.org/10.3390/atmos13010093

Hausfather, Z, Marvel, K, Schmidt, GA, Nielsen-Gammon, JW, Zelinka, M (2022) Climate simulations: Recognize the 'hot model' problem. *Nature*, **605**, 26-29. https://doi.org/10.1038/d41586-022-01192-2

Hawkings, JR, et al (2021) Large subglacial source of mercury from the southwestern margin of the Greenland Ice Sheet. Nat. Geosci. 14, 496-502. https://doi.org/10.1038/s41561-021-00753-w

Hawkins, E, Sutton, R (2009) The potential to narrow uncertainty in regional climate predictions. *B. Am. Meteor. Soc.* **90**(8), 1095-1108. https://doi.org/10.1175/2009BAMS2607.1

Hawkins, E, Frame, D, Harrington, L, et al (2021) Observed emergence of the climate change signal: from the familiar to the unknown, *Geopys. Res. Lett.* **47**(6) e2019GL086259 https://doi.org/10.1029/2019GL086259

Hazeleger, W, et al (2010) EC-Earth. *B. Am. Meteor. Soc.* **91**(10), 1357–1364. https://doi.org/10.1175/2010BAMS2877.1

Herein, M, Drótos, G, Haszpra, T, Márfy, J, Tél, T (2017) The theory of parallel climate realizations as a new framework for teleconnection analysis. *Sci. Rep.* **7**, 44529. https://doi.org/10.1038/srep44529

Herein, M, Márfy, J, Drótos, G, Tél, T (2016) Probabilistic concepts in intermediate-complexity climate models: a snapshot attractor picture. *J. Clim.* **29**(1), 259-272. https://doi.org/10.1175/JCLI-D-15-0353.1

Hermann, M, Papritz, L, Wernli, H (2020) A Lagrangian analysis of the dynamical and thermodynamic drivers of large-scale Greenland melt events during 1979–2017. *Weather. Clim. Dynam*. **1**, 497-518. https://doi.org/10.5194/wcd-1-497-2020

Hersbach, H et al. (2020) The ERA5 global reanalysis. *Q. J. R. Meteorol. Soc*. **146**, 1999-2049. https://doi.org/10.1002/qj.3803

Hirschi, M, Seneviratne, SI, Alexandrov, V et al (2010) Observational evidence for soil-moisture impact on hot extremes in southeastern Europe. *Nat. Geosci.* **4**, 17-21. https://doi.org/10.1038/ngeo1032

Hofer, S et al (2019) Cloud microphysics and circulation anomalies control differences in future Greenland melt. *Nat. Clim. Chang*. **9**, 523-528. https://doi.org/10.1038/s41558-019-0507-8

Hofer, S et al (2020) Greater Greenland Ice Sheet contribution to global sea level rise in CMIP6. *Nat. Commun.* **11**, 6289. https://doi.org/10.1038/s41467-020-20011-8

Hofer, S, Tedstone, AJ, Fettweis, X, Bamber, JL (2017) Decreasing cloud cover drives the recent mass loss on the Greenland Ice Sheet. *Sci. Adv*. **3**, e1700584. https://doi.org/10.1126/sciadv.1700584

Holland, DM, Thomas, RH, de Young, B, Ribergaard, MH, Lyberth, B (2008) Acceleration of Jakobshavn Isbræ triggered by warm subsurface ocean waters. *Nat. Geosci*. **1**, 659-664. https://doi.org/10.1038/ngeo316

Holland, MM, Landrum, L (2021) The emergence and transient nature of Arctic amplification in coupled climate models. *Front. Earth Sci.* **9**, 764. https://doi.org/10.3389/feart.2021.719024

Huang, J, Yu, H, Guan, X et al (2016) Accelerated dryland expansion under climate change. *Nat. Clim. Chang.* **6**, 166-171. https://doi.org/10.1038/nclimate2837

Huang, B et al. (2018) NOAA Extended Reconstructed Sea Surface Temperature (ERSST), version 5 [global]. NOAA National Centers for Environmental Information accessed 12 December (2018) https://doi.org/10.7289/V5T72FNM.

Huang, Y et al. (2021) Summertime low clouds mediate the impact of the large-scale circulation on Arctic sea ice. *Commun. Earth Environ.* **2**, 38. https://doi.org/10.1038/s43247-021-00114-w

Huang, Y et al. (2019) Thicker clouds and accelerated Arctic Sea ice decline: The atmosphere-sea ice interactions in spring. *Geophys. Res. Lett*., **46**, 6980-6989. https://doi.org/10.1029/2019GL082791

IPCC Climate Change 2013: The Physical Science Basis (eds Stocker, T.F. et al.) (Cambridge Univ. Press, 2013). ISBN 978-1-107-66182-0

IPCC, 2021: Climate Change 2021: The Physical Science Basis. Contribution of Working Group I to the Sixth Assessment Report of the Intergovernmental Panel on Climate Change [Masson-Delmotte, V., P.

Zhai, A. Pirani, S.L. Connors, C. Péan, S. Berger, N. Caud, Y. Chen, L. Goldfarb, M.I. Gomis, M. Huang, K. Leitzell, E. Lonnoy, J.B.R. Matthews, T.K. Maycock, T. Waterfield, O. Yelekçi, R. Yu, and B. Zhou (eds.)]. Cambridge University Press, Cambridge, United Kingdom and New York, NY, USA, 2391 pp. doi:10.1017/9781009157896.

Jahn, A (2018) Reduced probability of ice-free summers for 1.5 °C compared to 2 °C warming. *Nat. Clim. Chang.* **8**, 409413. https://doi.org/10.1038/s41558-018-0127-8

Jahn, A, Kay, JE, Holland, MM, Hall, DM (2016) How predictable is the timing of a summer ice-free Arctic? *Geophys. Res. Lett.* **43**(17), 9113-9120. https://doi.org/10.1002/2016GL070067

Jeffrey, S et al (2013) Australia's CMIP5 submission using the CSIRO-Mk3.6 model. *Aust. Meteorol. Oceanogr. J*. **63**, 1-13. https://doi.org/10.22499/2.6301.001

Kato, S et al (2018) Surface Irradiances of Edition 4.0 Clouds and the Earth's Radiant Energy System (CERES) Energy Balanced and Filled (EBAF) Data Product. *J. Clim.* **31**(11), 4501-4527. https://doi.org/10.1175/JCLI-D-17-0523.1

Kay, JE et al (2015) The Community Earth System Model (CESM) large ensemble project: A community resource for studying climate change in the presence of internal climate variability. *B. Am. Meteor. Soc.* **96**(8), 1333-1349. https://doi.org/10.1175/BAMS-D-13-00255.1

Kay, JE et al (2022) Less Surface Sea Ice Melt in the CESM2 Improves Arctic Sea Ice Simulation With Minimal Non-Polar Climate Impacts. *JAMES.* **14**, e2021MS002679. https://doi.org/10.1029/2021MS002679

Kirchmeier-Young, MC, Zwiers, FW, Gillett, NP (2017) Attribution of Extreme Events in Arctic Sea ice Extent. *J. Clim.* **30**(2), 553-571. https://doi.org/10.1175/JCLI-D-16-0412.1

Knutti, R, (2008) Should we believe model predictions of future climate c hange? *Philos Trans R Soc A* **366**, 4647-4664. https://doi.org/10.1098/rsta.2008.0169

Knutti, R (2010) The end of model democracy? *Clim. Change.* **102**, 395-404. https://doi.org/10.1007/s10584-010-9800-2

Knutti, R, Sedláček, J (2013) Robustness and uncertainties in the new CMIP5 climate model projections. *Nat. Clim. Chang.* **3**, 369–373. https://doi.org/10.1038/nclimate1716

Knutti, R, Sedláček J, Sanderson, B, Lorenz, R, Fischer, E, Eyring, V (2017) A climate model projection weighting scheme accounting for performance and interdependence: model projection weighting scheme *Geophys. Res. Lett*. **44**, 1909-1918. https://doi.org/10.1002/2016GL072012

Konecky, BL et al (2020) The Iso2k database: a global compilation of paleo-δ18O and δ2H records to aid understanding of Common Era climate. *Earth. Syst. Sci. Data.* **12**, 2261-2288. https://doi.org/10.5194/essd-12-2261-2020

Kröner, N, Kotlarski, S, Fischer, E et al (2017) Separating climate change signals into thermodynamic, lapse-rate and circulation effects: theory and application to the European summer climate. *Clim. Dyn.* **48**, 3425-3440. https://doi.org/10.1007/s00382-016-3276-3

L'Heureux, M, Tippett, MK, Kumar, A et al (2017) Strong Relations Between ENSO and the Arctic Oscillation in the North American Multimodel Ensemble. *Geophys. Res. Lett.* **44**(11), 654-662. https://doi.org/10.1002/2017GL074854

Labe, Z, Peings, Y, Magnusdottir, G, (2019) The effect of QBO phase on the atmospheric response to projected Arctic sea ice loss in early winter. *Geophys. Res. Lett*., **46**, 7663-7671. https://doi.org/10.1029/2019GL083095

Laliberté, F, Howell, SEL, Kushner, PJ (2016) Regional variability of a projected sea ice-free Arctic during the summer months. *Geophys. Res. Lett*. **43**, 256-263. https://doi.org/10.1002/2015GL066855

Lamarque, JF, et al (2010) Historical (1850–2000) gridded anthropogenic and biomass burning emissions of reactive gases and aerosols: methodology and application. *Atmos. Chem. Phys.* **10**, 7017-7039. https://doi.org/10.5194/acp-10-7017-2010

Landrum, L, Holland, MM, (2020) Extremes become routine in an emerging new Arctic. *Nat. Clim. Chang.* **10,** 1108-1115. https://doi.org/10.1038/s41558-020-0892-z

Lee, S (2012) Testing of the Tropically Excited Arctic Warming Mechanism (TEAM) with Traditional El Niño and La Niña. *J. Clim.* **25**, 4015-4022. https://doi.org/10.1175/JCLI-D-12-00055.1

Lefebre, F et al (2003) Modeling of snow and ice melt at ETH Camp (West Greenland): A study of surface albedo. *J. Geophys. Res*. **108**, 4231. https://doi.org/10.1029/2001JD001160

Lenaerts, JTM, Medley, B, Broeke, MR, Wouters, B (2019) Observing and modeling ice sheet surface mass balance. *Rev. Geophys.* **57**(2), 376-420. https://doi.org/10.1029/2018RG000622

Li, C, Notz, D, Tietsche, S, Marotzke, J (2013) The Transient versus the Equilibrium Response of Sea Ice to Global Warming, *J. Clim*. **26**(15), 5624-5636. https://doi.org/10.1175/JCLI-D-12-00492.1

Li, G, Xie, S, He, C et al (2017) Western Pacific emergent constraint lowers projected increase in Indian summer monsoon rainfall. *Nat. Clim. Change* **7**, 708-712. https://doi.org/10.1038/nclimate3387

Li, Z, Ding, Q, Steele, M et al (2022) Recent upper Arctic Ocean warming expedited by summertime atmospheric processes. Nat. Commun. 13, 362. https://doi.org/10.1038/s41467-022-28047-8

Liang, Y, Gillett, NP, Monahan, AH (2022) Emergent Constraints on CMIP6 Climate Warming Projections: Contrasting Cloud- and Surface Temperature–Based Constraints, *J. Clim*. **35**(6), 1809-1824. https://doi.org/10.1175/JCLI-D-21-0468.1

Loeb, NG (2018) Clouds and the Earth's Radiant Energy System (CERES) Energy Balanced and Filled (EBAF) Top-of-Atmosphere (TOA) Edition-4.0 Data Product, *J. Clim*. **31**(**2**), 895-918. https://doi.org/10.1175/JCLI-D-17-0208.1

Lorenz, EN (1963) Deterministic Nonperiodic Flow. *J. Atmos. Sci.* **20**(2), 130-141. https://doi.org/10.1175/1520-0469(1963)020<0130:DNF>2.0.CO;2

Lorenz, R, Argüeso, D, Donat, MG et al (2016) Influence of land-atmosphere feedbacks on temperature and precipitation extremes in the GLACE-CMIP5 ensemble. *J. Geophys. Res. Atmos*. **121**, 607-623. https://doi.org/10.1002/2015JD024053

Lovino, MA, Müller, OV, Berbery, EH et al. (2018) Evaluation of CMIP5 retrospective simulations of temperature and precipitation in northeastern Argentina. *Int. J. Climatol.* **38**. 1158-1175. https://doi.org/10.1002/joc.5441

Lu, J, Vecchi, GA, Reichler, T, (2007) Expansion of the Hadley cell under global warming. *Geophys. Res. Lett.* **34,** L06805. https://doi.org/10.1029/2006GL028443

Lucarini, V, Ragone, F, Lunkeit, F, (2017) Predicting climate change using response theory: global averages and spatial patterns*. J. Stat. Phys.* **166**, 1036–1064. https://doi.org/10.1007/s10955-016-1506-z

Luo, R et al (2021) Summertime atmosphere–sea ice coupling in the Arctic simulated by CMIP5/6 models: Importance of large-scale circulation. Clim. Dyn. 56, 1467-1485. https://doi.org/10.1007/s00382-020-05543-5

Maher, N et al. (2019) The Max Planck Institute Grand Ensemble – enabling the exploration of climate system variability. *J. Adv. Model.* **11**, 2050-2069. https://doi.org/10.1029/2019MS001639

Mann, ME et al (2018) Projected changes in persistent extreme summer weather events: the role of quasi-resonant amplification*. Sci. Adv.* **4**(10), eaat3272. https://doi.org/10.1126/sciadv.aat3272

McCabe, GJ, Palecki, MA (2006) Multidecadal climate variability of global lands and oceans. *Int. J. Climatol.* **26**, 849-865. https://doi.org/10.1002/joc.1289

McCrystall, MR, Hosking, JS, White, IP, Maycock, AC (2020) The Impact of Changes in Tropical Sea Surface Temperatures over 1979–2012 on Northern Hemisphere High-Latitude Climate. *J. Clim*. **33**, 5103-5121. https://doi.org/10.1175/JCLI-D-19-0456.1

Meehl, GA, Chung, CTY, Arblaster, JM, Holland, MM, Bitz, CM (2018) Tropical decadal variability and the rate of Arctic sea ice decrease. *Geophys. Res. Lett*. **45**, 11,326-11,333. http://dx.doi.org/10.1029/2018GL079989

Merrifield, AL, Brunner, L, Lorenz, R et al (2020) An investigation of weighting schemes suitable for incorporating large ensembles into multi-model ensembles. *Earth. Syst. Dynam.* **11***,* 807-834. https://doi.org/10.5194/esd-11-807-2020

Min, SK, Hense, A (2006) A Bayesian approach to climate model evaluation and multi-model averaging with an application to global mean surface temperatures from IPCC AR4 coupled climate models. *Geophys. Res. Lett.* **33**, L08708. https://doi.org/10.1029/2006GL025779

Mioduszewski, JR, Rennermalm, AK, Hammann, A, Tedesco, M, Noble, EU, Stroeve, JC, Mote, TL (2016) Atmospheric drivers of Greenland surface melt revealed by self-organizing maps. *J. Geophys. Res. Atmos.* **121**, 5095-5114. https://doi.org/10.1002/2015JD024550

Moritz, RE, Bitz, CM, Steig, E (2002) Dynamics of recent climate change in the Arctic. *Science*, **297** (5586), 1497-1502. https://doi.org/10.1126/science.1076522

Mouginot, J et al (2019) Forty-six years of Greenland Ice Sheet mass balance from 1972 to 2018. *Proc. Natl. Acad. Sci. USA* **116**(19), 9239-9244. https://doi.org/10.1073/pnas.1904242116

Muntjewerf, L, Petrini, M, Vizcaino, M, Ernani da Silva, C, Sellevold, R, Scherrenberg, MDW et al (2020) Greenland Ice Sheet contribution to 21st century sea level rise as simulated by the coupled CESM2.1-CISM2.1. *Geophys. Res. Lett.* **47**, e2019GL086836. https://doi.org/10.1029/2019GL086836

Murphy, JM, Sexton, DMH, Barnett, DN et al (2004) Quantification of modelling uncertainties in a large ensemble of climate change simulations. *Nature* **430**, 768-772. https://doi.org/10.1038/nature02771

Nash, JE, Sutcliffe, JV (1970) River flow forecasting through conceptual models part I - A discussion of principles. *J. Hydrol.* **10**(3), 280-290. https://doi.org/10.1016/0022-1694(70)90255-6

Niederdrenk, AL, Notz, D (2018) Arctic Sea Ice in a 1.5°C Warmer World. *Geophys. Res. Lett*. **45**, 1963-1971. https://doi.org/10.1002/2017GL076159

Noël, B, van de Berg, WJ, Lhermitte, S, van den Broeke, MR (2019) Rapid ablation zone expansion amplifies north Greenland mass loss. *Sci. Adv.* **5**, eaaw0123. https://doi.org/10.1126/sciadv.aaw0123

Noël, B, van Kampenhout, L, Lenaerts, JTM, van de Berg, WJ, van den Broeke, MR (2021) A 21st century warming threshold for sustained Greenland ice sheet mass loss. *Geophys. Res. Lett.* **48**, e2020GL090471. https://doi.org/10.1029/2020GL090471

Noël, B, van Kampenhout, L, van de Berg, WJ, Lenaerts, JTM, Wouters, B, and van den Broeke, MR (2020) Brief communication: CESM2 climate forcing (1950–2014) yields realistic Greenland ice sheet surface mass balance, *Cryosphere*, **14**, 1425-1435. https://doi.org/10.5194/tc-14-1425-2020

Notz, D, SIMIP Community (2020). Arctic Sea Ice in CMIP6. *Geophys. Res. Lett*. **47**(10), e2019GL086749 https://doi.org/10.1029/2019GL086749

Notz, D, (2015) How well must climate models agree with observations? *Phil. Trans. R. Soc. A* **373**, 20140164. https://doi.org/10.1098/rsta.2014.0164

Notz, D, (2014) Sea-ice extent and its trend provide limited metrics of model performance, *Cryosphere*, **8**, 229-243. https://doi.org/10.5194/tc-8-229-2014

Notz, D, Marotzke, J (2012) Observations reveal external driver for Arctic sea-ice retreat. *Geophys. Res. Lett.*, **39**, L08502. https://doi.org/10.1029/2012GL051094

Notz, D, Stroeve, JC (2016) Observed Arctic sea-ice loss directly follows anthropogenic CO2 emission. *Science*, **354**(6313), 747-750. https://doi.org/10.1126/science.aag234

Notz, D, Haumann, A, Haak, H, Jungclaus, J, Marotzke, J (2013) Arctic sea ice evolution as modeled by Max Planck Institute for Meteorology's Earth system model. *JAMES*, **5,** 173-194. https://doi.org/10.1002/jame.20016

Olonscheck, D, Mauritsen, T, Notz, D (2019): Arctic sea-ice variability is primarily driven by atmospheric temperature fluctuations. *Nat. Geosci.* **12,** 430-434. https://doi.org/10.1038/s41561-019-0363-1

Olson, R, An, S, Fan, Y et al (2019) A novel method to test non-exclusive hypotheses applied to Arctic ice projections from dependent models. *Nat. Commun.* **10**, 3016. https://doi.org/10.1038/s41467-019-10561-x

PAGES2k Consortium (2017) A global multiproxy database for temperature reconstructions of the Common Era. *Sci. Data.* **4**, 170088. https://doi.org/10.1038/sdata.2017.88

Perez, J, Menendez, M, Mendez, FJ et al (2014) Evaluating the performance of CMIP3 and CMIP5 global climate models over the north-east Atlantic region. *Clim. Dyn.* **43**, 2663-2680. https://doi.org 10.1007/s00382-014-2078-8

Pfleiderer, P, Schleussner, C, Kornhuber, K et al (2019) Summer weather becomes more persistent in a 2 °C world. *Nat. Clim. Chang.* **9**, 666-671 https://doi.org/10.1038/s41558-019-0555-0

Pieczka, I, Pongrácz, R, Szabóné, AK et al (2017) Sensitivity analysis of different parameterization schemes using RegCM4.3 for the Carpathian region. *Theor. Appl. Climatol.* **130**, 1175-1188. https://doi.org/10.1007/s00704-016-1941-4

Polade, S, Pierce, D, Cayan, D et al (2015) The key role of dry days in changing regional climate and precipitation regimes. *Sci. Rep.* **4**, 4364. https://doi.org/10.1038/srep04364

Poli, P et al (2016) ERA-20C: An Atmospheric Reanalysis of the Twentieth Century. *J. Clim.* **29**(11). https://doi.org/10.1175/JCLI-D-15-0556.1

Previdi, M, Smith, KL, Polvani, LM (2021) Arctic amplification of climate change: a review of underlying mechanisms. *Environ. Res. Lett.* **16,** 093003. https://doi.org 10.1088/1748-9326/ac1c29

Rahmstorf, S et al (2015) Exceptional twentieth-century slowdown in Atlantic Ocean overturning circulation. *Nat. Clim. Chang.* **5**, 475-480. https://doi.org/10.1038/nclimate2554

Reichler, T, Kim, J (2008) How well do coupled models simulate today's climate? *B. Am. Meteor. Soc.* **89**(3), 303-312. https://doi.org/10.1175/BAMS-89-3-303

Rignot, E, Fenty, I, Menemenlis, D, Xu, Y (2012) Spreading of warm ocean waters around Greenland as a possible cause for glacier acceleration. *Ann. Glaciol*. **53**, 257-266. https://doi.org /10.3189/2012AoG60A136

Roach, LA, Blanchard-Wrigglesworth, E, (2022) Observed Winds Crucial for September Arctic Sea Ice Loss, *Geophys. Res. Lett*. **49**, e2022GL097884. https://doi.org/10.1029/2022GL097884

Rodgers, KB, Lin, J, Frölicher, TL (2015) Emergence of multiple ocean ecosystem drivers in a large ensemble suite with an Earth system model. *Biogeosciences* **12**, 3301–3320. https://doi.org/10.5194/bg-12-3301-2015

Rodgers, K et al (2021) Ubiquity of human-induced changes in climate variability. *Earth. Syst. Dynam*. **12**, 1393-1411. https://doi.org/10.5194/esd-12-1393-2021

Rosenblum, E., Eisenman, I (2017) Sea Ice Trends in Climate Models Only Accurate in Runs with Biased Global Warming, *J. Clim*, **30**(16), 6265-6278. https://doi.org/10.1175/JCLI-D-16-0455.1

Rosenzweig C, Karoly, D, Vicarelli, M et al (2008) Attributing physical and biological impacts to anthropogenic climate change. *Nature* **453**, 353-357. https://doi.org/10.1038/nature06937

Ruti, PM, Somot, S, Giorgi, F et al (2016) Med-CORDEX Initiative for Mediterranean Climate Studies. *B. Am. Meteor. Soc*. **97**(7), 1187-1208. . https://doi.org/10.1175/BAMS-D-14-00176.1

Rutt, I, Hagdorn, M, Hulton, N, Payne, A (2009) The Glimmer community ice sheet model. *J. Geophys. Res*. **114**, F02004. https://doi.org/10.1029/2008JF001015

Sanderson, BM, Knutti, R, Caldwell, P (2015) Addressing Interdependency in a Multimodel Ensemble by Interpolation of Model Properties. *J. Clim.* **28**(13), 5150-5170. https://doi.org/10.1175/JCLI-D-14-00361.1

Santer, BD et al (2018) Human influence on the seasonal cycle of tropospheric temperature. Science 361(6399), eaas8806. https://doi.org/10.1126/science.aas8806

Schneider, T (2007) The thermal stratification of the extratropical troposphere. The Global Circulation of the Atmosphere, T. Schneider and A. H. Sobel, Eds., Princeton University Press, 47–77. https://doi.org/10.1515/9780691236919-005

Schwingshackl, C, Hirschi, M, Seneviratne, SI (2018) A theoretical approach to assess soil moisture–climate coupling across CMIP5 and GLACE-CMIP5 experiments. *Earth . Syst. Dynam.* **9**, 1217–1234. https://doi.org/10.5194/esd-9-1217-2018

Screen, JA, Deser, C (2019) Pacific Ocean variability influences the time of emergence of a seasonally ice-free Arctic Ocean. *Geophys. Res. Lett*., **46**(4), 2222-2231 https://doi.org/10.1029/2018GL081393

Screen, JA, Francis, JA (2016) Contribution of sea ice loss to Arctic amplification is regulated by Pacific Ocean decadal variability. *Nat. Climate Change*, **6**, 856-860. https://doi.org/10.1038/nclimate3011

Screen, JA, Williamson, D (2017) Ice-free Arctic at 1.5°C? *Nat. Clim. Chang.* **7**, 230-231. https://doi.org/10.1038/nclimate3248

Screen, JA, Simmonds, I (2010) The central role of diminishing sea ice in recent Arctic temperature amplification. *Nature* **464,** 1334–1337. https://doi.org/10.1038/nature09051

Screen, JA, Deser, C, Smith, DM et al (2018) Consistency and discrepancy in the atmospheric response to Arctic sea-ice loss across climate models. Nature. Geosci. 11, 155–163. https://doi.org/10.1038/s41561-018-0059-y

Selten, FM, Bintanja, R, Vautard, R et al (2020) Future continental summer warming constrained by the present-day seasonal cycle of surface hydrology. Sci. Rep. 10, 4721. https://doi.org/10.1038/s41598-020-61721-9

Sobel, A, Nilsson, J, Polvani, LM (2001) The weak temperature gradient approximation and balanced tropical moisture waves. *J. Atmos. Sci.* **58**, 3650-3665. https://doi.org/10.1175/1520-0469(2001)058<3650:TWTGAA>2.0.CO;2

Lutsko, NJ (2018) The Response of an Idealized Atmosphere to Localized Tropical Heating: Superrotation and the Breakdown of Linear Theory, *J. Atmos. Sci*. **75**(1), 3-20. https://doi.org/10.1175/JAS-D-17-0192.1

Seneviratne, S, Lüthi, D, Litschi, M et al. (2006) Land–atmosphere coupling and climate change in Europe. *Nature* **443**, 205-209. https://doi.org/10.1038/nature05095

Seneviratne, SI, Wilhelm, M, Stanelle, T (2013) Impact of soil moisture-climate feedbacks on CMIP5 projections: First results from the GLACE-CMIP5 experiment. *Geophys. Res. Lett.* **40**, 5212-5217. https://doi.org/10.1002/grl.50956

Senftleben, D, Lauer, A, Karpechko, A (2020) Constraining Uncertainties in CMIP5 Projections of September Arctic Sea Ice Extent with Observations. *J. Clim.* **33**(4), 1487-1503. https://doi.org/10.1175/JCLI-D-19-0075.1

Serreze, MC, Francis, JA (2006) The Arctic Amplification Debate. *Clim. Chang.* **76,** 241-264. https://doi.org/10.1007/s10584-005-9017-y

Serreze, MC (2011) Climate change: Rethinking the sea-ice tipping point. *Nature*, **471**, 47-48. https://doi.org/10.1038/471047a

Shahi, S, Abermann, J, Heinrich, G, Prinz, R, Schöner, W (2020) Regional Variability and Trends of Temperature Inversions in Greenland. *J. Clim.* **33**(21), 9391-940 https://doi.org/10.1175/JCLI-D-19-0962.1

Sheerwood, F, Fu, Q, (2014) A drier future? *Science* **343**(6172), 737-739. https://doi.org/10.1126/science.1247620

Sheffield, J, Barrett, AP, Colle, B et al (2013) North American Climate in CMIP5 Experiments. Part I: Evaluation of Historical Simulations of Continental and Regional Climatology. *J. Clim.* **26**(23), 9209-9245. https://doi.org/10.1175/JCLI-D-12-00592.1

Sherman, P, Tziperman, E, Deser, C, McElroy, M (2020) Historical and future roles of internal atmospheric variability in modulating summertime Greenland Ice Sheet melt. *Geophys. Res. Lett*. **47**, e2019GL086913. https://doi.org/10.1029/2019GL086913

Sigmond, M, Fyfe, JC, Swart, NC, (2018) Ice-free Arctic projections under the Paris Agreement. *Nat. Clim. Chang.* **8**, 404-408. https://doi.org/10.1038/s41558-018-0124-y

Sillmann, J, Kharin, VV, Zhang, X et al (2013) Climate extremes indices in the CMIP5 multimodel ensemble: Part 1. Model evaluation in the present climate. *J. Geophys. Res. Atmos.* **118**, 1716-1733. https://doi.org/10.1002/jgrd.50203

Simmonds, I (2015) Comparing and contrasting the behaviour of Arctic and Antarctic sea ice over the 35 year period 1979–2013. *Ann.Glaciol.* **56**(69), 18-28. https://doi.org/10.3189/2015AoG69A909

Sippel, S, Meinshausen, N, Fischer, EM et al (2020) Climate change now detectable from any single day of weather at global scale. *Nat. Clim. Chang.* **10**, 35-41. https://doi.org/10.1038/s41558-019-0666-7

Slater, T, Hogg, AE, Mottram, R (2020) Ice-sheet losses track high-end sea-level rise projections. *Nat. Clim. Chang.* **10**, 879-881. https://doi.org/10.1038/s41558-020-0893-y

Slivinski, LC et al (2019) Towards a more reliable historical reanalysis: Improvements for version 3 of the Twentieth Century Reanalysis system. *Q. J. R. Meteorol. Soc.* **145,** 2876-2908. https://doi.org/10.1002/qj.3598

Stainforth, DA, Allen, MR, Tredger, ER et al (2007) Confidence, uncertainty and decision-support relevance in climate predictions. *Phil. Trans. R. Soc. A* **365**, 2145-2161. https://doi.org/10.1098/rsta.2007.2074

Steele, M, Zhang, J, Ermold, W (2010) Mechanisms of summertime upper Arctic Ocean warming and the effect on sea ice melt. *J. Geophys. Res*. **115**, C11004. https://doi.org/10.1029/2009JC005849

Steele, M., Ermold, W, Zhang, J (2008) Arctic Ocean surface warming trends over the past 100 years. *Geophys. Res. Lett.* **35**, L02614. https://doi.org/10.1029/2007GL031651

Stroeve, JC, Notz, D (2015) Insights on past and future sea-ice evolution from combining observations and models. *Glob. Planet. Chang.* **135**, 119-132. https://doi.org/10.1016/j.gloplacha.2015.10.011

Stroeve, JC, Holland, MM, Meier, W, Scambos, T, Serreze, MC (2007) Arctic sea ice decline: Faster than forecast. *Geophys. Res. Lett.* **34**(9). https://doi.org/10.1029/2007GL029703

Student (1908) The probable error of a mean. *Biometrika*, 1–25. https://doi.org/10.2307/2331554

Suh, MS, Oh, SG, Lee, DK et al (2012) Development of new ensemble methods based on the performance skills of regional climate models over South Korea. *J. Clim.* **25**(20), 7067-7082. https://doi.org/10.1175/JCLI-D-11-00457.1

Sun, L, Alexander, M, Deser, C (2018) Evolution of the Global Coupled Climate Response to Arctic Sea Ice Loss during 1990–2090 and Its Contribution to Climate Change. *J. Clim*. **31**, 7823-7843. https://doi.org/10.1175/JCLI-D-18-0134.1

Svendsen, L, Keenlyside, N, Bethke, I, Gao, Y, Omrani, NE (2018) Pacific contribution to the early twentieth-century warming in the Arctic. *Nat. Clim. Chang.* **8**, 793-797. https://doi.org/10.1038/s41558-018-0247-1

Swart, NC, Fyfe, JC, Hawkins, E et al (2015) Influence of internal variability on Arctic sea ice trends. *Nat. Clim. Chang.* **5**, 86–89. https://doi.org/10.1038/nclimate2483

Syed, FS, Latif, M, Al-Maashi, A et al (2019) Regional climate model RCA4 simulations of temperature and precipitation over the Arabian Peninsula: sensitivity to CORDEX domain and lateral boundary conditions. *Clim. Dyn*. **53**, 7045-7064. https://doi.org/10.1007/s00382-019-04974-z

Talagrand, O, Vautard, R, Strauss, B (1997) Evaluation of probabilistic prediction systems. Proc. ECMWF Workshop on Predictability, Reading, United Kingdom, ECMWF, 1–25, https://www.ecmwf.int/en/elibrary/12555-evaluation-probabilistic- prediction-systems

Tardif, R et al. (2019) Last Millennium Reanalysis with an expanded proxy database and seasonal proxy modeling, *Clim. Past* **15,** 1251-1273. https://doi.org/10.5194/cp-15-1251-2019

Taylor, C, de Jeu R, Guichard, F et al (2012a) Afternoon rain more likely over drier soils. *Nature* **489**, 423-426. https://doi.org/10.1038/nature11377

Taylor, KE, Stouffer, RJ, Meehl, GA (2012b) An Overview of CMIP5 and the Experiment Design. *B. Am. Meteor. Soc.* **93**(4), 485-498. https://doi.org/10.1175/BAMS-D-11-00094.1

Tedesco, M et al. (2016) The darkening of the Greenland ice sheet: Trends, drivers, and projections (1981-2100). *Cryosphere* **10**, 477-496. https://doi.org/10.5194/tc-10-477-2016

Tedesco, M, Fettweis, X (2020) Unprecedented atmospheric conditions (1948–2019) drive the 2019 exceptional melting season over the Greenland ice sheet. *Cryosphere*, **14**, 1209-1223. https://doi.org/10.5194/tc-14-1209-2020

Tél, T, Bódai, T, Drótos, G et al (2019) The Theory of Parallel Climate Realizations. J. Stat. Phys. 179, 1496-1530. https://doi.org/10.1007/s10955-019-02445-7

Thackeray, CW, Hall, A, (2019) An emergent constraint on future Arctic sea-ice albedo feedback. *Nat. Clim. Chang.* **9,** 972-978. https://doi.org/10.1038/s41558-019-0619-1

The IMBIE Team, Shepherd, A et al (2020) Mass balance of the Greenland Ice Sheet from 1992 to 2018. *Nature* **579**, 233-239. https://doi.org/10.1038/s41586-019-1855-2

Tokarska, KB, Stolpe, MB, Sippel, S, Fischer, EM, Smith, CJ, Lehner, F, Knutti, R (2020). Past warming trend constrains future warming in CMIP6 models. *Sci Adv*, **6**(12), eaaz9549. https://doi.org/10.1126/sciadv.aaz9549

Tokinaga, H, Xie, SP, Mukougawa, H (2017) Early 20th-century Arctic warming intensified by Pacific and Atlantic multidecadal variability. *Proc. Nat. Acad. Sci. USA* **114**. https://doi.org/10.1073/pnas.1615880114

Topál, D, Ding, Q, (in prep) Constrained model sensitivity recalibrates projected Arctic climate change. in review in *Nat. Clim. Chang.*

Topál, D, Ding, Q., Ballinger, TJ et al (2022) Discrepancies between observations and climate models of large-scale wind-driven Greenland melt influence sea-level rise projections. *Nat. Commun*. **13**, 6833 https://doi.org/10.1038/s41467-022-34414-2

Topál, D, Ding, Q, Mitchell, J, Baxter, I, Herein, M, Haszpra, T, Luo, R, Li, Q (2020a). An Internal Atmospheric Process Determining Summertime Arctic Sea Ice Melting in the Next Three Decades: Lessons Learned from Five Large Ensembles and Multiple CMIP5 Climate Simulations, *J. Clim.* **33**(17), 7431-7454. https://doi.org/10.1175/JCLI-D-19-0803.1

Topál, D, Hatvani, IG, Kern, Z, (2020b) Refining projected multidecadal hydroclimate uncertainty in East-Central Europe using CMIP5 and single-model large ensemble simulations. *Theor. Appl. Climatol.* **142**, 1147-1167. https://doi.org/10.1007/s00704-020-03361-7

Uotila, P, O'Farrell, S, Marsland, SJ, Bi, D (2013) The sea-ice performance of the Australian climate models participating in the CMIP5. *Australian Meteorological and Oceanographic Journal*, **63**, 121-143. https://doi.org/10.22499/2.6301.008

Valler, V, Franke, J, Brugnara, Y, Brönnimann, S (2021) An updated global atmospheric paleo-reanalysis covering the last 400 years, *Geosci. Data J.* **9(1)**, 89-107. https://doi.org/10.1002/gdj3.121

Van Tricht, K et al (2016) Clouds enhance Greenland ice sheet meltwater runoff. *Nat. Commun*. **7**, 10266. https://doi.org/10.1038/ncomms10266

Vaughan, DG, Comiso, JC, Allison, I, Carrasco, J, Kaser, G, Kwok, R, Mote, P, Murray, T, Paul, F, Ren, J, Rignot, E (2013) Observations: cryosphere. *IPCC Climate Change*, **2103**, 317-382.

Verfaillie, D, Favier, V, Gallée, H, et al. (2019) Regional modeling of surface mass balance on the Cook Ice Cap, Kerguelen Islands (49°S, 69°E*). Clim. Dyn.* **53**, 5909-5925. https://doi.org/10.1007/s00382-019-04904-z

Vogel, MM, Zscheischler, J, Seneviratne, SI (2018) Varying soil moisture–atmosphere feedbacks explain divergent temperature extremes and precipitation projections in central Europe*. Earth. Syst. Dyn.* **9**, 1107-1125. https://doi.org/10.5194/esd-9-1107-2018

Wang, C, Zhang, L, Lee, SK et al (2014) A global perspective on CMIP5 climate model biases. Nat. Clim. Chang. 4, 201-205. https://doi.org/10.1038/nclimate2118

Wang, M, Overland, JE (2009) A sea ice free summer Arctic within 30 years? *Geophys. Res. Lett*. **36**, L07502. https://doi.org/10.1029/2009GL037820

Warner, JL, Screen, JA, Scaife, AA (2020) Links between Barents-Kara sea ice and the extratropical atmospheric circulation explained by internal variability and tropical forcing. *Geophys. Res. Lett.* **47**, e2019GL085679. https://doi.org/10.1029/2019GL085679

Wernli, H, Papritz, L (2018) Role of polar anticyclones and mid-latitude cyclones for Arctic summertime sea-ice melting. *Nat Geosci* **11,** 108-113. https://doi.org/10.1038/s41561-017-0041-0

Winton, M (2011) Do Climate Models Underestimate the Sensitivity of Northern Hemisphere Sea Ice Cover? *J. Clim*. **24**(15), 3924-3934. https://doi.org/10.1175/2011JCLI4146.1

Wood, M et al (2021) Ocean forcing drives glacier retreat in Greenland. *Sci. Adv*. **7**, eaba7282. https://doi.org/10.1126/sciadv.aba7282

Wood, RR, Ludwig, R (2020). Analyzing internal variability and forced response of subdaily and daily extreme precipitation over Europe. *Geophys. Res. Lett*. **47**, e2020GL089300. https://doi.org/10.1029/2020GL089300

Yapo, ALM, Diawara, A, Kouassi, BK, et al (2020) Projected changes in extreme precipitation intensity and dry spell length in Côte d'Ivoire under future climates. *Theor. Appl. Climatol.* **140**, 871-889. https://doi.org/10.1007/s00704-020-03124-4

Zelinka, MD, Myers, TA, McCoy, DT, Po-Chedley, S, Caldwell, PM, Ceppi, P, Taylor, KE (2020) Causes of higher climate sensitivity in CMIP6 models. *Geophys. Res. Lett.* **47**, e2019GL085782. https://doi.org/10.1029/2019GL085782

Zeng, X, Pielke, RA, Eykholt, R (1993) Chaos Theory and Its Applications to the Atmosphere. *B. Am. Meteor. Soc.* **74**(4), 631-644. https://doi.org/10.1175/1520-0477(1993)074<0631:CTAIAT>2.0.CO;2.

Zhang, J, Lindsay, R, Schweiger, A, Steele, M (2013) The impact of an intense summer cyclone on 2012 Arctic sea ice retreat. *Geophys. Res. Lett*. **40**, 720-726. https://doi.org/10.1002/grl.50190

Zhang, R (2007) Anticorrelated multidecadal variations between surface and subsurface tropical North Atlantic. *Geophys. Res. Lett.* **34**, L12713. https://doi.org/10.1029/2007GL030225

Zhang, R (2015) Mechanisms for low-frequency variability of summer Arctic sea ice extent. *Proc. Nat. Acad. Sci. USA*. **22296**, 4570-4575. https://doi.org/10.1073/pnas.1422296112

Zhu, J, Poulsen, CJ, Otto-Bliesner, BL (2020) High climate sensitivity in CMIP6 model not supported by paleoclimate. *Nat. Clim. Chang.* **10**, 378-379. http://dx.doi.org/10.1038/s41558-020-0764-6

Zuo, H, Balmaseda, MA, Tietsche, S, Mogensen, K, Mayer, M (2019) The ECMWF operational ensemble reanalysis-analysis system for ocean and sea ice: a description of the system and assessment. *Ocean Sci.* **15**, 779-808. https://doi.org/10.5194/os-15-779-2019

6 SUPPLEMENTARY MATERIAL

Supplementary Table 1. 30 ice core records across the GrIS used in the study and the correlation coefficients between the individual ice cores and the MCA(1) related expansion coefficient time-series of *Z500* (r<Z500>) and the 200hPa Greenland streamfunction index (r<Ψ200>) in the EKF400 simulation. The source codes of the oceanic coral records are also shown in the rightmost column referring to the codes of the original datasets in PAGES2k Consortium (2017). The bold coefficients mark significant correlations ($p<0.05$).

Ice Core Site	Lat	Lon	r(Z500)	r(Ψ200)	Coral proxy site
Prince-of-Wales	78.4	-80.4	-0.13	**-0.24**	Ocn_095
B26	77.25	-49.22	-0.05	-0.09	Ocn_111
B19	78	-36.4	-0.03	-0.01	Ocn_087
B27	76.66	-46.48	0.06	0.02	Ocn_140
B21	80	-41.14	-0.06	0.02	Ocn_073
B22	79.34	-45.91	-0.01	0.03	Ocn_099
Agassiz A79	80.7	-73.1	0.03	0.05	Ocn_078
Camp Century	77.17	-61.13	-0.08	0.1	Ocn_156
B16	73.94	-37.63	-0.07	0.1	Ocn_109
B20	78.83	-36.5	-0.08	0.1	Ocn_110
GRIP	72.58	-37.64	0.15	0.1	Ocn_060
Site G	71.76	-35.85	0.05	0.1	Ocn_122
Devon Ice Cap	75.33	-82.5	-0.08	0.12	Ocn_097
B18	76.62	-36.4	-0.02	0.16	Ocn_090
B30	75	-42	0.04	0.16	Ocn_081
Site E	71.15	-35.84	0.12	**0.18**	Ocn_080
B23	78	-44	0.19	**0.19**	Ocn_120
Agassiz A87	80.7	-73.1	-0.04	**0.19**	Ocn_062
B17	75.25	-37.62	0.11	**0.2**	Ocn_098
B28	76.66	-46.48	0.13	**0.2**	Ocn_075
Renland	71.27	-26.73	0.11	**0.21**	Ocn_125
NEEM	77.45	-51.06	0.17	**0.22**	Ocn_130
B29	76	-43.49	0.09	**0.22**	Ocn_103
Site A	70.63	-35.82	0.14	**0.23**	Ocn_179
GISP2	72.6	-38.5	0.16	**0.25**	Ocn_068
Site D	70.64	-39.62	**0.2**	**0.25**	Ocn_084
Crete	71.12	-37.32	0.14	**0.28**	Ocn_079
DYE2	66.38	-46.18	0.16	**0.29**	Ocn_083
NGRIP	75.1	-42.32	**0.26**	**0.3**	Ocn_077
Milcent	70.3	-44.58	**0.28**	**0.38**	Ocn_074
					Ocn_088
					Ocn_119
					Ocn_086

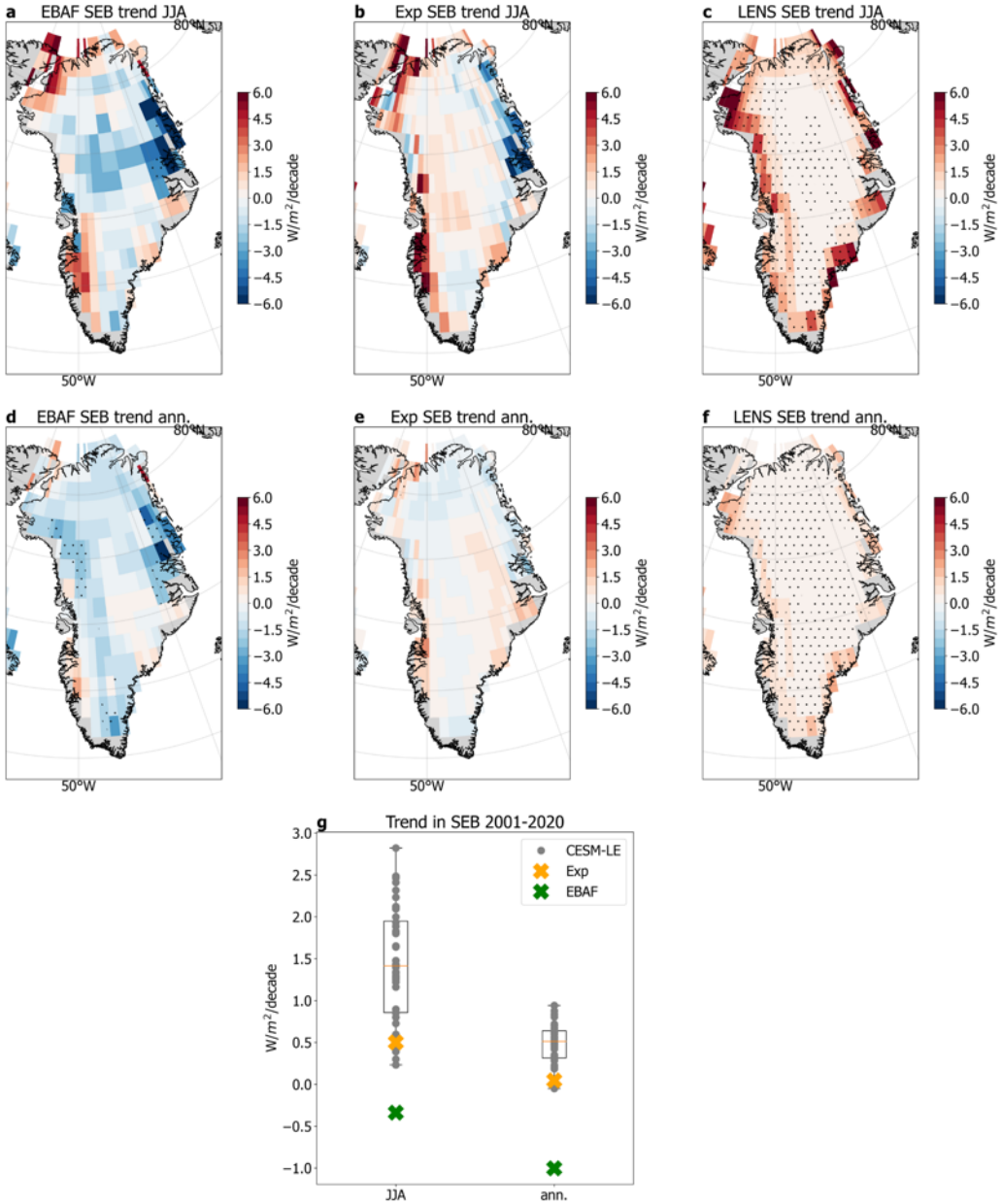

Supplementary Figure 1. Maps of the linear trends in the surface energy balance (SEB = SWnet+LWnet) in (a) the EBAF satellite product, (b) the nudging experiment (Exp) and (c) the CESM large ensemble mean (LENS) in summer (June-July-August, JJA) during 2001-2020. (d)-(f) is the same as (a)-(c) but for annual means. Panel (g) shows the GrIS spatially averaged linear trends in the SEB from the LENS (grey dots) and the nudging experiment (Exp, orange marker) along with the EBAF satellite product (green marker) in JJA (first column) and annual means (second column) for 2001-2020. Stippling indicates statistically significant trends on 95% confidence level.

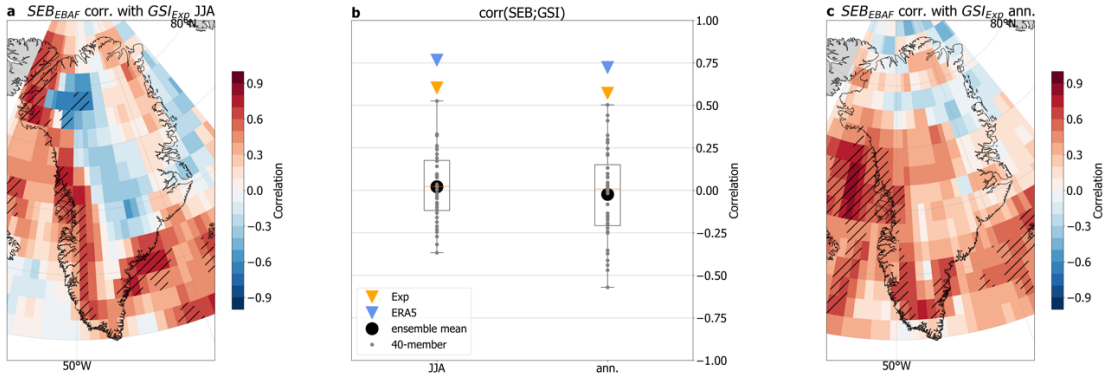

Supplementary Figure 2. Panels (a) and (c) show the correlation between EBAF surface energy balance (*SEB*) and the nudging experiment derived 500hPa Greenland streamfunction index (*GSI*) for JJA and annual means, respectively, and (b) shows the correlation between EBAF *SEB* and *GSI* in ERA5 (blue triangle) or the nudging experiment (orange triangle) along with the correlation between *SEB* and *GSI* in each member of the CESM-LE (grey dots) and the mean of each member's correlation (black dot) for JJA (left box plot) and annual means (right box plot) (see legend in panel (b)). Hatching in (a),(c) indicate areas with statistically-significant correlations ($p<0.05$).

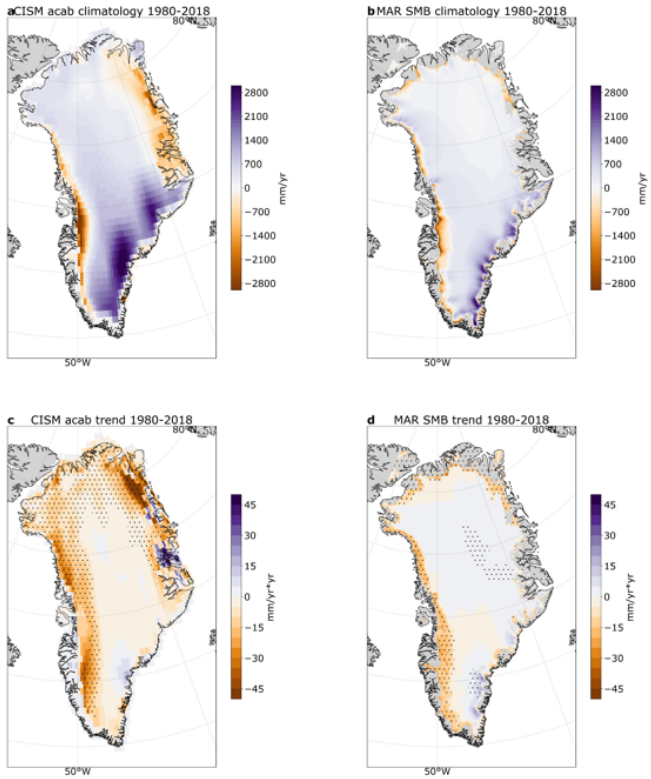

Supplementary Figure 3. Comparison between the (a) nudging experiment-driven CISM Glimmer simulation and the (b) MAR *SMB* (forced by ERA5) spatial climatologies for 1980-2018 annual means along with the *SMB* linear trend maps in the (c) Glimmer simulation and in (d) MAR.

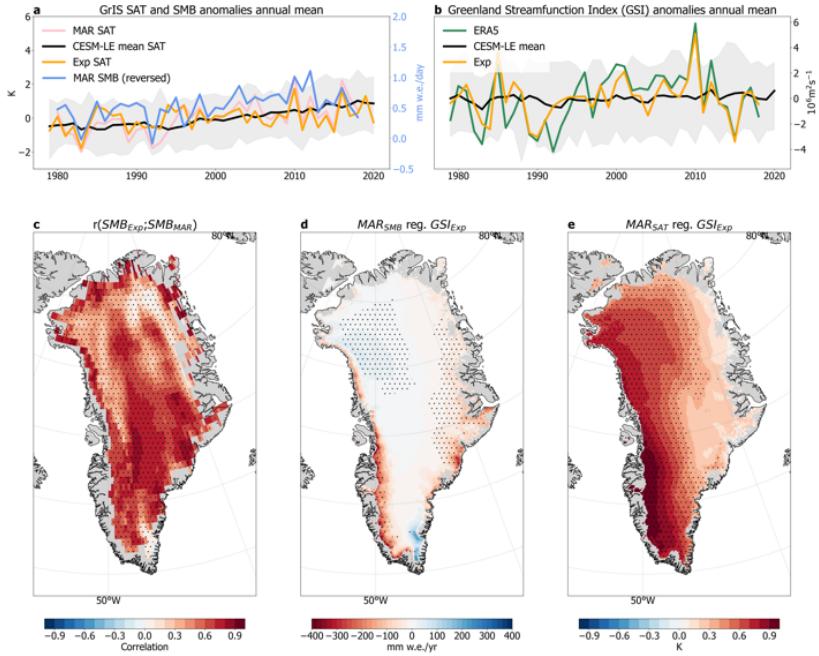

Supplementary Figure 4. (a) GrIS spatially-averaged time-series of anomalies in MAR surface air temperature (*SAT*, pink) and surface mass balance (*SMB*, blue), the ensemble mean *SAT* from CESM large ensemble (CESM-LE, black) and the *SAT* from the wind-nudging experiment (Exp) in CESM1 (orange) for the annual means. The grey shading in (a) represents all members' SAT anomalies from the CESM-LE. In (b) ERA5 500hPa Greenland streamfunction index (*GSI*) (green) is compared with the GSI calculated using the CESM-LE mean (black), the spread in CESM-LE (grey shading) and the wind-nudging experiment (Exp, orange) for annual means. Also shown: (c) the grid-point-wise correlation between the MAR and the CISM Glimmer experiment derived annual mean SMB along with the regression maps of (d) MAR *SMB* and (e) MAR *SAT* onto the 500hPa *GSI* derived from the nudging experiment. Hatching in (c)-(e) indicate areas with statistically-significant correlations or regressions ($p<0.05$).

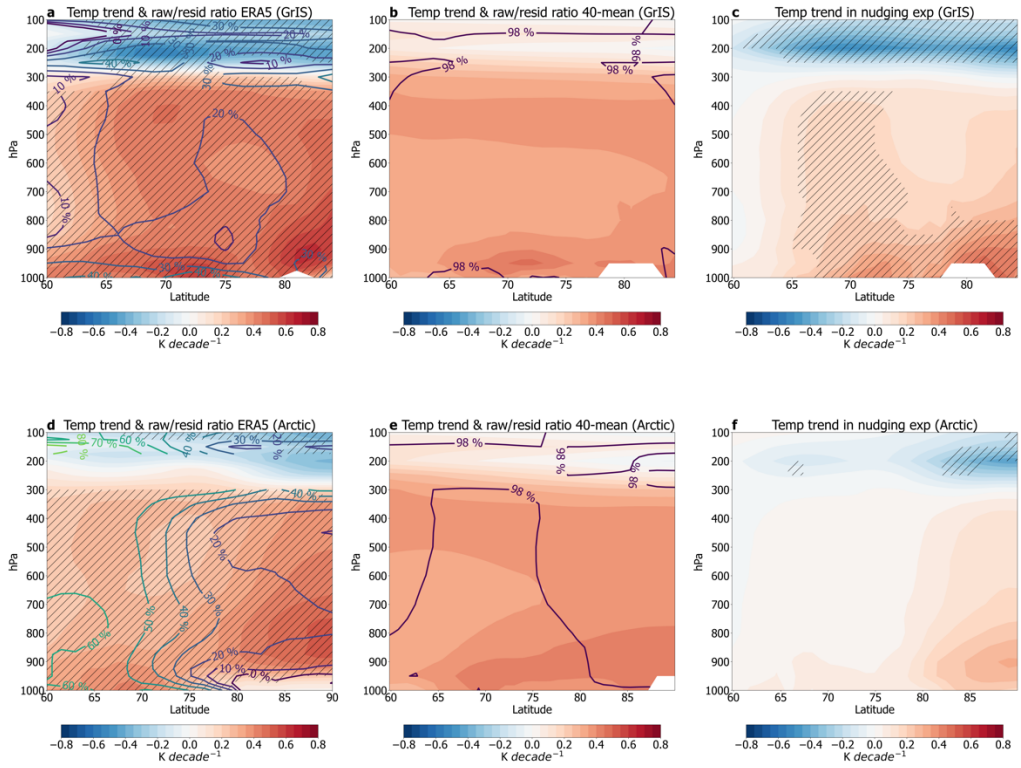

Supplementary Figure 5. Linear trend vertical cross-section of zonal mean temperature over (a)-(c) the GrIS (280-340ºE; 60-85ºN) and (d)-(f) over the Arctic (60-90ºN) in summer (June-July-August, JJA) between 1979-2020 in (a),(d) ERA5, (b),(e) CESM1-LE mean simulation and (c),(f) in our nudging experiment (see **Section 2.10**). In (a)-(b) and (d)-(e) the ratio of the raw and the residual trend values are also shown in percentages, where the residual trends refer to the temperature trends after having removed the corresponding streamfunction indices (*ASI/GSI*) at each vertical level and latitude point. Statistically significant linear trend values (two-sample t-test at 95% confidence level) are hatched.